LEVEL II A063487 (12)

DNA 4425F-2

AD A090218

THEORETICAL AND LABORATORY STUDY OF DEEP-BASED STRUCTURES

Volume II—Model Tests and Analyses of Mighty Epic Structures

SRI International
333 Ravenswood Avenue
Menlo Park, California 94025

15 January 1979

Final Report for Period 1 April 1975—15 January 1979

CONTRACT No. DNA 001-75-C-0245

APPROVED FOR PUBLIC RELEASE;
DISTRIBUTION UNLIMITED.

THIS WORK SPONSORED BY THE DEFENSE NUCLEAR AGENCY
UNDER RDT&E RMSS CODE B344075462 J34EAXSX31102 H2590D.

Prepared for
Director
DEFENSE NUCLEAR AGENCY
Washington, D. C. 20305

OCT 14 1980

A

80 10 9 014

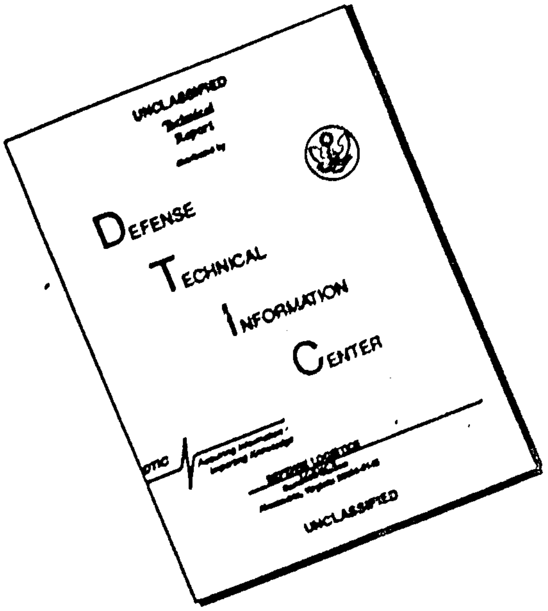

UNCLASSIFIED
Technical
Report

DEFENSE
TECHNICAL
INFORMATION
CENTER

DTIC

UNCLASSIFIED

UNCLASSIFIED

SECURITY CLASSIFICATION OF THIS PAGE (*When Data Entered*)

REPORT DOCUMENTATION PAGE

19

READ INSTRUCTIONS BEFORE COMPLETING FORM

1. REPORT NUMBER
8 DNA 4425F-2

2. GOVT ACCESSION NO.
AD-A090218

3. RECIPIENT'S CATALOG NUMBER
9

4. TITLE (and Subtitle)
6 THEORETICAL AND LABORATORY STUDY OF DEEP-BASED STRUCTURES. Volume II. Model Tests and Analyses of Mighty Epic Structures.

5. ~~TYPE OF REPORT & PERIOD COVERED~~
Final Report, ~~for Period~~ 1 Apr 75—15 Jan 79.

6. PERFORMING ORG. REPORT NUMBER
SRI Project PYU-4121

7. ~~AUTHOR(s)~~
10 P. E. Senseny
H. E. Lindberg

8. CONTRACT OR GRANT NUMBER(s)
15 DNA 001-75-C-0245

9. PERFORMING ORGANIZATION NAME AND ADDRESS
SRI International
333 Ravenswood Avenue
Menlo Park, California 94025

10. PROGRAM ELEMENT, PROJECT, TASK AREA & WORK UNIT NUMBERS
Subtask J34EAXSX311-02
16

11. CONTROLLING OFFICE NAME AND ADDRESS
Director
Defense Nuclear Agency
Washington, D.C. 20305

17 X311

12. ~~REPORT DATE~~
11 15 Jan[redacted]979

13. NUMBER OF PAGES
156
12 153

14. MONITORING AGENCY NAME & ADDRESS(*if different from Controlling Office*)

15. SECURITY CLASS (*of this report*)
UNCLASSIFIED

15a. DECLASSIFICATION DOWNGRADING SCHEDULE

16. DISTRIBUTION STATEMENT (*of this Report*)

Approved for public release; distribution unlimited.

17. DISTRIBUTION STATEMENT (*of the abstract entered in Block 20, if different from Report*)

18. SUPPLEMENTARY NOTES

This work sponsored by the Defense Nuclear Agency under RDT&E RMSS Code B344075462 J34EAXSX31102 H2590D.

19. KEY WORDS (*Continue on reverse side if necessary and identify by block number*)

Deep Basing	Lined Tunnels
Scale Models	Laboratory Tests
Structural Response	Dynamic Tests
Rock Response	Static Tests

20. ABSTRACT (*Continue on reverse side if necessary and identify by block number*)

Laboratory tests were performed on 5/8-inch- (16mm) diameter scale models of cylindrical structures fielded in Mighty Epic. The model structures were tested in 4-inch- (0.1-m) diameter specimens of SRI RMG2C2, a tuff simulant. Results from these tests show that (1) structures are damaged less during dynamic loading than during static loading, (2) if yielding occurs in the free field, tunnel closure is not greatly influenced by structure strength, and (3) structures can effectively resist deformation

DD FORM 1 JAN 73 1473 EDITION OF 1 NOV 65 IS OBSOLETE

UNCLASSIFIED

SECURITY CLASSIFICATION OF THIS PAGE (*When Data Entered*)

20. ABSTRACT (Continued)

under repeated loading. Theoretical analyses were performed for axisymmetric loading of a deep-based structure in SRI RMG 2C2. Results show that (1) the analyses can predict tunnel closures measured in the isotropic loading laboratory tests, (2) theoretical tunnel closures under plane strain loading (radical pressure at infinity and axial strains identically zero) and isotropic loading (hydrostatic pressure at infinity) differ only slightly, but (3) tunnel closure and rock stress field under end-on loading differ substantially from closure and stress under isotropic loading; thus substantial theoretical extrapolation of rock response is needed to predict tunnel closures in the field during end-on loading using isotropic loading laboratory data, even though both loading types produce symmetric tunnel response.

SUMMARY

This project had two goals: (1) develop a large-scale testing machine for laboratory experiments on scale model deep-based structures and (2) perform a theoretical and laboratory study of deep-based structures in support of the Mighty Epic structures test. Paralleling these goals, the final report is divided into two volumes: Volume I: Triaxial Machine for Static and Dynamic Testing of 12-inch-Diameter Rocks, and Volume II: Model Tests and Analysis of Mighty Epic Structures.

Volume I: Triaxial Machine for Static and Dynamic Testing of 12-inch Diameter Rocks

The first volume describes the design, fabrication, and development of a large-scale testing machine capable of testing specimens 12 inches (0.3 m) in diameter and 12 to 18 inches (0.3 to 0.45 m) in height, three times larger than the specimens for the smaller testing machine developed for DNA at SRI. The large-scale machine incorporates most of the design and operational features of the smaller prototype, but its larger size permits study of more detailed scale model structures and use of more comprehensive instrumentation. Like the small machine, the large-scale testing machine consists of a series of stacked rings and plates secured by 12 high-strength studs that span the distance between plates at the bottom and top of the machine. Using a number of rings and plates rather than a single chamber gives the machine maximum flexibility: static and dynamic testing configurations make use of the same parts in both isotropic and triaxial configurations, although the functions and location of the parts in the machine stack may be quite different. Another feature, also developed with the small prototype, is the provision of ports in the testing machine that permit visual and physical access to the tunnel in the rock specimen during the test, allowing instrumentation and photographic coverage of the tunnel deformation.

The testing machine may be used to apply a range of static and dynamic triaxial loadings, among which are those that simulate symmetric and side-on loadings of deep-based structures in the field. Static loading pressures are applied by two independently operated, air-driven hydraulic pumps; dynamic loading pressures are applied by two separate explosive gas sources. The maximum vertical pressure that can be applied is about 2 kbar (0.2 GPa) statically and about 1 kbar (0.1 GPa) dynamically. For both static and dynamic tests, the maximum lateral pressure is 1.5 kbar (0.15 GPa).

Volume II: Model Tests and Analysis of Mighty Epic Structures

The second volume describes laboratory experiments performed on 4-inch- (0.1-m) diameter specimens containing reinforced tunnels. Theoretical analyses are also included to aid interpretation of the experimental results.

The specimens were made of SRI RMG 2C2, a tuff simulant, and included scale models of five different direct-contact structures fielded in Mighty Epic. The pressures applied to the specimens simulated both side-on (uniaxial strain) loading and symmetric (isotropic) loading of deep-based structures in the field. Both loading types were applied statically and dynamically.

The results of the laboratory tests for each structure are summarized in Figures S.1 through S.4 The first three figures give plots of tunnel closure as a function of applied pressure for three 6061-TO aluminum monocoque liners of different strengths; the fourth gives a plot of tunnel closure as a function of applied pressure for two 1015 steel liners of equal radius-to-thickness ratio. One steel structure was a monocoque liner and the other was a liner stiffened to resist buckling. Specimens containing steel structures were subjected to uniaxial strain loading only. The data in these four figures show that the reproducibility of the tunnel closure measurements is good.

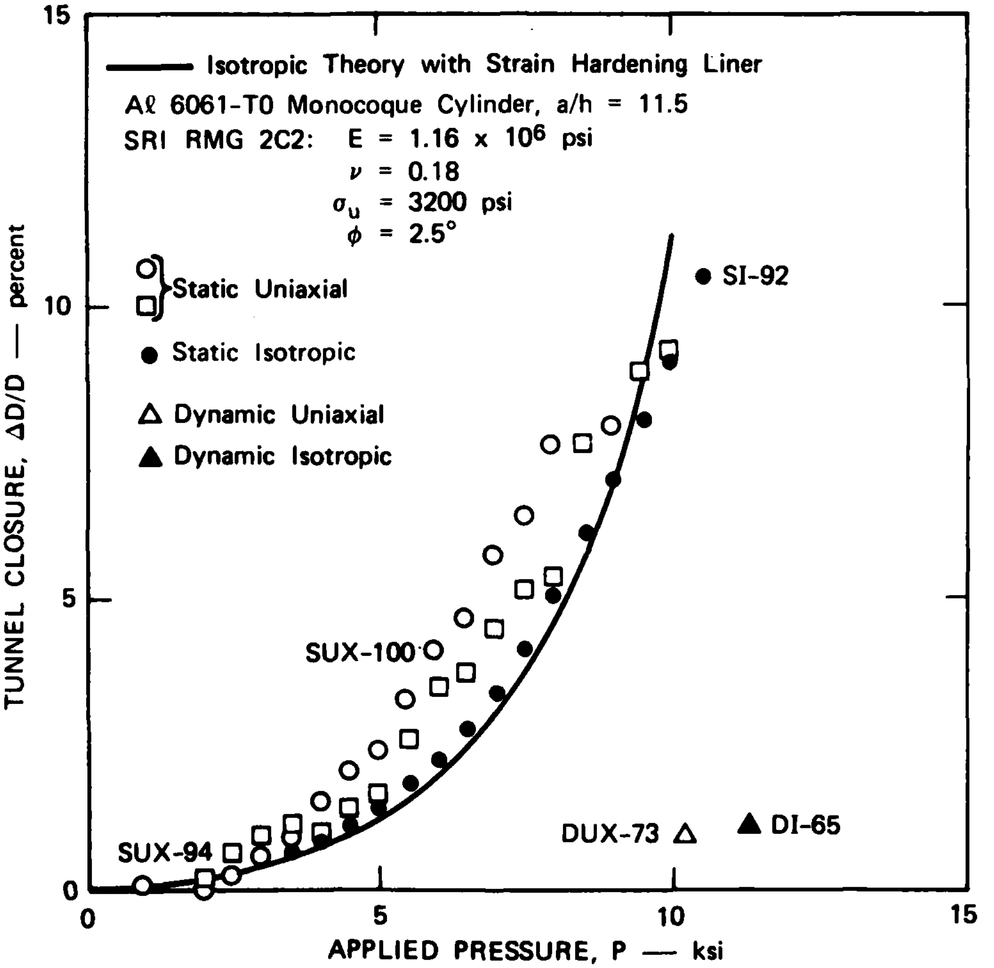

FIGURE S.1 COMPARISON OF TUNNEL CLOSURES IN SRI RMG 2C2 FOR UNIAXIAL STRAIN AND ISOTROPIC LOADING — Aℓ 6061-T0 LINER, a/h = 11.5

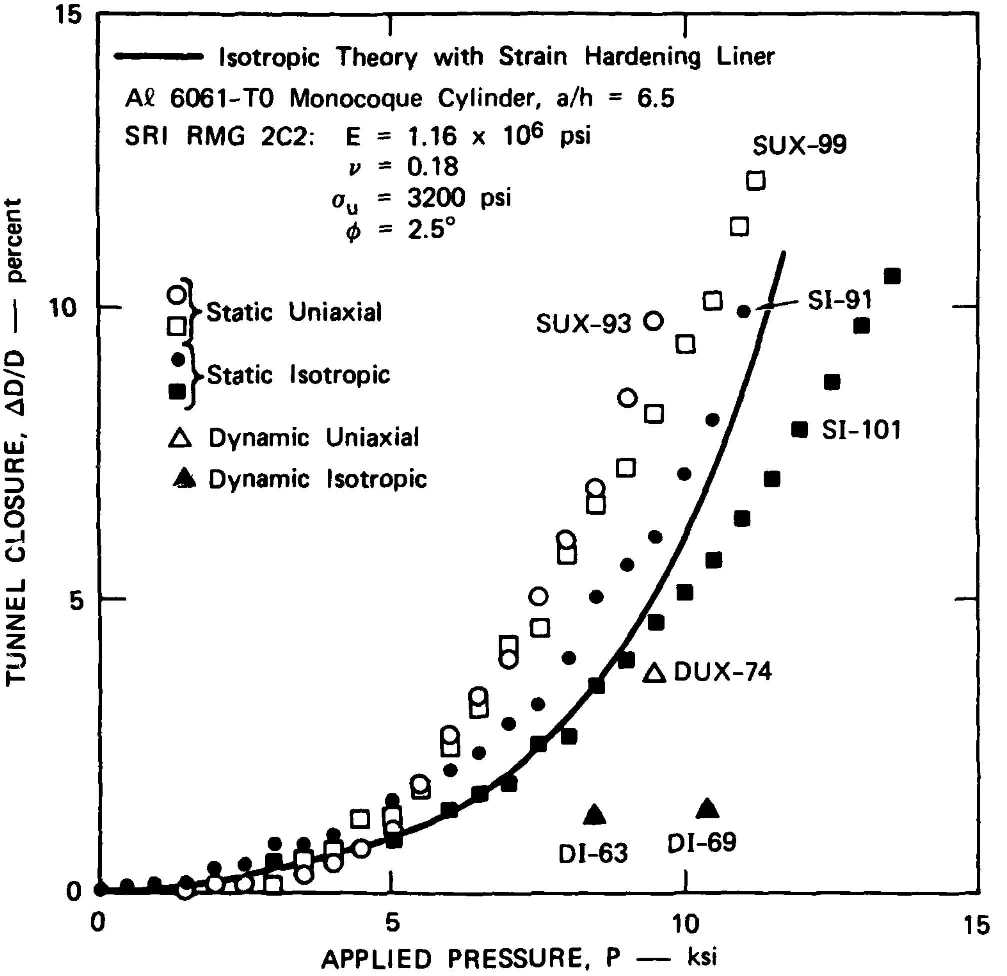

MA-4121-65 A

FIGURE S.2 COMPARISON OF TUNNEL CLOSURES IN SRI RMG 2C2 FOR UNIAXIAL STRAIN AND ISOTROPIC LOADING — Aℓ 6061-T0 LINER, a/h = 6.5

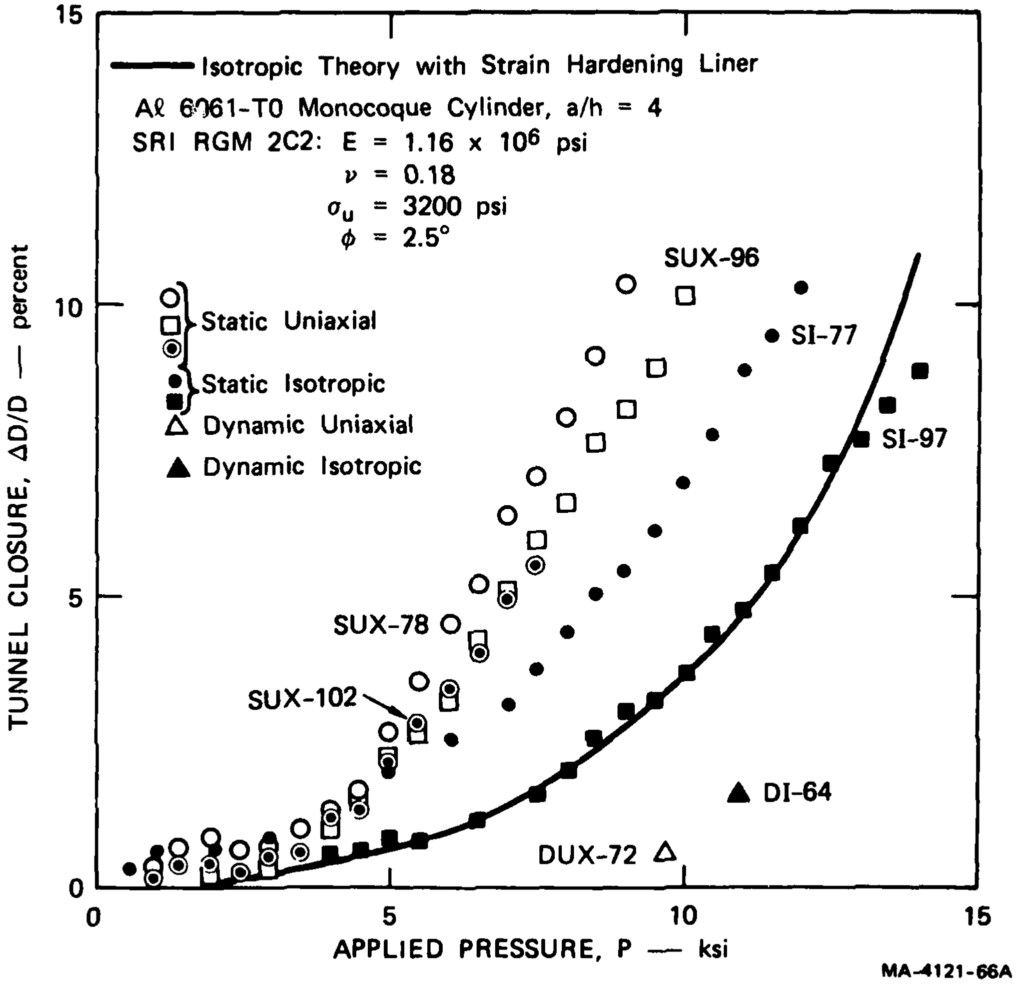

FIGURE S.3 COMPARISON OF TUNNEL CLOSURES IN SRI RMG 2C2 FOR UNIAXIAL STRAIN AND ISOTROPIC LOADING — Aℓ 6061-T0 LINER, a/h = 4.0

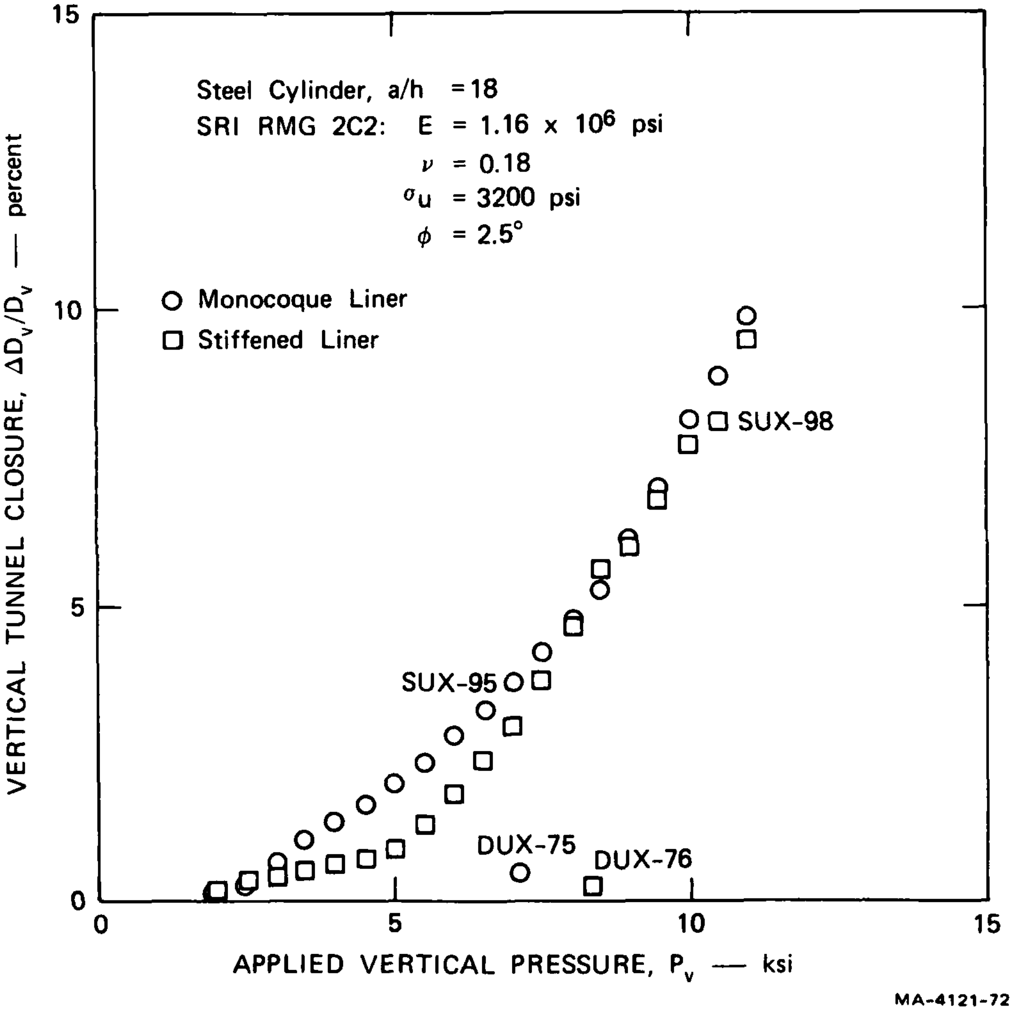

FIGURE S.4 VERTICAL TUNNEL CLOSURE IN SRI RMG 2C2 FOR STATIC AND DYNAMIC UNIAXIAL STRAIN LOADING — 1015 STEEL LINER, a/h = 18

Results of the tests on the Al 6061-TO liners indicate that:

(1) Tunnel closures measured under static isotropic loading are less than those measured under static uniaxial strain loading.

(2) This difference in tunnel closure increases as the strength of the tunnel liner increases.

(3) Tunnel closures obtained under dynamic loading are considerably smaller than those obtained under static loading.

Results from the uniaxial strain loading tests with 1015 steel liners also support this last observation.

The first result, that static isotropic tunnel closures are smaller than static uniaxial strain tunnel closures, is expected because under isotropic loading the liner resists deformation through hoop compression, the most efficient means of resistance for a thin-walled shell, and the liner carries a large portion of the load. Under uniaxial strain loading, however, the liner resists deformation through a combination of hoop compression and bending; therefore, the rock must carry more of the load than under isotropic loading.

This distinction also explains the second result, that the difference between static isotropic and static uniaxial strain tunnel closures increases with increasing liner strength. Under isotropic loading the liner carries much of the load, and the use of a stronger liner reduces the closure significantly. However, under uniaxial strain loading the rock carries most of the load, and use of a stronger liner does not affect the closure noticeably. In fact, the results of all the static uniaxial strain loading tests, including those on the 1015 steel structures, show that the strength of the tunnel liner has a relatively small influence on tunnel closure. This result is attributed to yielding of the rock in the free field because of the low strength of tuff and the tuff simulant.

The third result, that dynamic tunnel closures are significantly smaller than static tunnel closures, suggests that porewater pressure has a significant influence on the amount of tunnel closure obtained in tests on saturated rocks. The static tests were performed under drained conditions (zero porewater pressure), while in the dynamic tests loading times are so short that porewater drainage can be neglected.

A theoretical tunnel closure curve for isotropic loading is plotted in each of the first three figures. These curves were calculated with the closed form symmetric loading solution worked out by Hendron and used in designing the Mighty Epic structures. Yielding in the theory is treated with the Mohr-Coulomb yield function and associated flow rule, and strain hardening of the aluminum liner material is accounted for. The theory also assumes that the out-of-plane (along the tunnel axis) plastic and elastic strains are both zero. It is shown in the main text that, for the low friction angles of tuff-like materials, this last assumption is violated. Nevertheless, the reasonably good agreement between theorv and experiment in Figures S.1 through S.3 supports use of the simple theory for preliminary design analysis. Comparisons with more elaborate theoretical results that take account of out-of-plane plastic strain and also model the laboratory experiment more closely are given in the main text.

The results relating tunnel liner strength to the static load-carrying capability of the combined rock and tunnel structure, and also the agreement between theory and experiment for symmetric loading, are the same as results obtained from the previous program at SRI with a stronger rock having higher internal friction. These consistent results, over a range of material parameters, indicate that we are correctly relating the response and the most important strength properties of the liner and rock materials.

A series of special tests was also performed. The loading in these tests was static, but it differed from the static monotonic, isotropic, or uniaxial strain loading of the other tests. Results of these tests are shown in Section 6 (Figures 6.1, 6.2, 6.3, and 6.6). In two of the tests, one isotropic and the other uniaxial strain, the loading pressures were cycled. The results of these two tests show that the reinforced rock cavity shakes down, i.e., that during subsequent loading, tunnel closure does not increase until the applied pressure exceeds the maximum pressure applied during previous loadings. In the third special test, the specimen was subjected to uniaxial strain loading followed by isotropic loading to simulate the repeat loading of structures fielded in both Mighty Epic (side-on loading) and Diablo Hawk (end-on loading). The results of this test show that the structure's load-carrying capability under isotropic loading is not degraded by the initial uniaxial strain loading. Further, the vertical tunnel closure during the isotropic loading portion of the test does not exceed the maximum vertical tunnel closure achieved during the uniaxial strain loading until the loading pressure is greater than the maximum vertical pressure applied during the uniaxial strain loading. In the fourth special test, a uniaxial strain-like loading test, the lateral confining pressure was held at 0.5 ksi (3.45 MPa) and the specimen was allowed to expand radially until the lateral strain reached 0.1 percent. Results from this test show that the tunnel closure is greater than for uniaxial strain loading, and we conclude that the magnitude of the tunnel closure for a given vertical pressure is sensitive to small deviations from uniaxial strain loading.

We also report on the fabrication of four tunnel reinforcing structures that were tested at Waterways Experiment Station in the static, 30-inch-(0.76-m) diameter testing machine.

Blank

TABLE OF CONTENTS

APPENDICES

LIST OF ILLUSTRATIONS

Figure

Figure

Figure

Figure

Figure

Blank

1. INTRODUCTION

1.1 BACKGROUND

This report is the third in a series [1,2][*] of reports describing laboratory experiments performed on scale models of deep-based structures. The goal of the laboratory program, in conjunction with computational and field testing programs, is to develop efficient structures for deep basing. Deep-based structures are needed to protect command, control, and communication centers from nuclear attack. Because of the high cost of building these structures, efficiency is important, the most efficient structure being the one that provides the necessary volume and hardness at least cost.

Laboratory tests on scale models are used to relate structural response to the properties of the surrounding rock over a wider range of geological and loading conditions than can be obtained from field tests alone. Laboratory tests also permit various deep-basing concepts to be investigated more economically and quickly than field tests.

Most laboratory tests on scale models of deep-based structures use rock-matching grouts as the rock material. This eliminates some of the specimen-to-specimen variation typical of laboratory scale geological samples. Furthermore, use of rock-matching grouts permits parameters such as strength, grain size, and friction angle to be selected independently. Previous experiments on scale models of deep-based structures have been devoted almost exclusively to static testing. One exception is an earlier laboratory program at SRI [1] in which most of the experiments were dynamic, with the loading pulse scaled to simulate a long duration ground shock from a nuclear burst.

---

[*] Numbers in brackets designate references at the end of the report.

1.2 APPROACH AND SCOPE OF INVESTIGATION

We studied the response of scale model deep-based structures using water-saturated SRI RMG 2C2, a tuff simulant, as the rock material. We loaded the specimens with two distinct types of static and dynamic loads. The first type, isotropic loading, is axisymmetric with respect to the tunnel axis. Isotropic loading produces the symmetric stress field around a deep-based structure subjected to end-on loading (but the axial stress and flow conditions are quite different). Perhaps more important, it also provides a means of correlating experimental results with existing theoretical predictions. The second loading type, uniaxial strain loading, simulates the side-on loading of a deep-based structure. For this type of loading, the confining pressure is selected to enforce the constraints provided by the surrounding rock in the field, that is, no far field motion in the plane normal to the loading direction.

The structures tested were scale models of five structures fielded in the Mighty Epic event. Three were monocoque 6061-T0 aluminum liners of different mean-radius-to-wall-thickness ratios and having nominal Mighty Epic design strengths* of 0.4, 0.5, and 0.6 kbar (40, 50, and 60 MPa). The two remaining structures were 1015 steel liners having a design strength of 0.5 kbar (50 MPa); one was a monocoque cylinder and the other was a stiffened cylinder with circumferential ribs to resist buckling.

Table 1.1 shows the test matrix. Both static and dynamic tests were performed with both isotropic and uniaxial strain loading. We also performed several special tests including tests in which the applied loading was cyclic. The experiments were supported by a theoretical effort in which both closed-form and numerical solutions were used to interpret the experimental results.

---

*These strengths are defined as the symmetric pressures P_0 to produce 5 percent closure when the liners are placed in nominal tuff with properties as estimated during the planning stage for Mighty Epic (Young's modulus $E = 1.0 \times 10^6$ psi (6.9 GPa), Poisson's ratio $\nu = 0.25$, unconfined strength $\sigma_u = 1460$ psi (10 MPa), and friction angle $\phi = 7.4$ degrees [0.129 rad.]).

Table 1.1 TESTS IN SRI RMG 2C2 (Tuff Simulant)

Model Type	Strength		a/h	Static Loading		Dynamic Loading	
	P_i (psi)	Design P_o (kbar)		Isotropic Stress	Uniaxial Strain	Isotropic Stress	Uniaxial Strain
Al 6061-TO	3300	0.6	4	SI-77 SI-97 SI-80[a]	SUX-78 SUX-96 SUX-79[a] SUX-90[b] SUX/SI-102[c]	DI-64	DUX-72
Al 6061-TO	2100	0.5	6.5	SI-91 SI-101	SUX-93 SUX-99	DI-63 DI-69	DUX-74
Al 6061-TO	1200	0.4	11.5	SI-92	SUX-94 SUX-100	DI-65	DUX-73
Monocoque steel	2100	0.5	18	--	SUX-95	--	DUX-75
Stiffened steel	2100	0.5	18	--	SUX-98	--	DUX-76

[a] Cycling loading.

[b] Underconfined.

[c] Followed by isotropic loading.

1.3 ORGANIZATION OF THE REPORT

The remainder of this report describes results of experiments performed on 4-inch- (0.1-m) diameter specimens of SRI RMG 2C2 that contain reinforced tunnels and the theoretical analyses used to interpret the experimental data. Chapter 2 describes both closed-form and numerical analyses performed in support of the laboratory tests. Chapter 3 gives a brief description of the testing machines and specimens used in this program. Chapters 4 and 5 describe the results of isotropic and uniaxial strain loading experiments, respectively. Chapter 6 describes the results of four special tests in which the loading differed from the standard monotonically increasing isotropic or uniaxial strain loading. In Chapter 7 we describe the fabrication of several large scale model reinforcing structures that were tested at Waterways Experiment Station (WES).

2. THEORETICAL ANALYSIS

Theoretical analyses were performed to aid interpretation of experimental data. The analyses indicated how our laboratory data may be related to deformation of deep-based structures in the field. Both numerical and closed-form analyses were performed. Results are shown to agree with experimental results obtained from laboratory tests described in the following chapters.

The problem we considered is a boundary value problem for a rock medium that contains a long cylindrical cavity reinforced with a thin liner. The boundary of the rock is subjected to axisymmetric pressure as shown in Figure 2.1. The rock medium is assumed to be isotropic and homogenous and is taken to be a linear elastic, perfectly plastic material whose failure behavior is governed by the Mohr-Coulomb criterion and associated flow rule. The rock medium is, therefore, dilatant. For our calculations we take the rock medium to be SRI RMG 2C2, a tuff simulant characterized by the four parameters given below.

Young's modulus	$E = 1.16 \times 10^6$ psi (8 GPa)
Poisson's ratio	$\nu = 0.18$
Unconfined compressive strength	$\sigma_u = 3200$ psi (22 MPa)
Friction angle	$\phi = 2.5°$ (0.044 rad.)

These parameters are averages of data resulting from material properties tests performed by both Terra Tek and WES. SRI RMG 2C2 is the grout used in the laboratory tests discussed in the following chapters.

Axisymmetric loading of structures occurs in our laboratory experiments for isotropic loading, and in the field when the structure faces the working point end-on. There is, however, a significant difference between end-on loading in the field and isotropic loading in the laboratory. In the field, the pressure that loads the structure is the pressure induced by the uniaxial flow constraint, i.e., no radial motion in the far field. In the laboratory, the pressure that loads the specimen is the

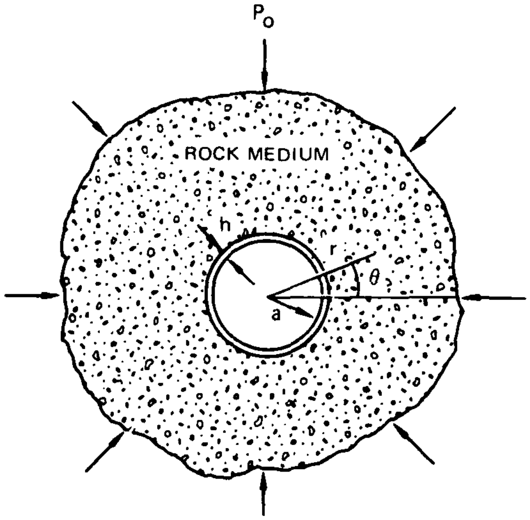

MA-4121-153A

FIGURE 2.1 SCHEMATIC OF BOUNDARY VALUE PROBLEM FOR A ROCK MEDIUM CONTAINING A LONG CYLINDRICAL CAVITY isotropic (hydrostatic) applied pressure. We analyzed both loading conditions numerically and will compare the results later in this chapter.

2.1 CLOSED-FORM SOLUTION

A closed-form solution was obtained previously [1,3] for a lined circular tunnel in an infinite rock medium subjected to axisymmetric radial pressure at infinity. In this solution the rock failure envelope was assumed to be linear (constant friction angle). The presence of the tunnel liner was modeled by a pressure inside the tunnel equal to the yield pressure of the tunnel liner. It was also assumed that the deformation was plane strain and that both the elastic and plastic components of the out-of-plane normal strain ε_z vanish individually. This solution is used widely to design structures for field testing.

In the present investigation we extended the analysis to treat an increase in liner pressure as the tunnel closes, so that we could interpret experiments performed here with liners of 6061-TO aluminum, which strain hardens appreciably, as shown in Figure 2.2. This extension to hardening liners is discussed in the next section. The solution was also generalized to include nonlinear failure envelopes, typical of many geological materials. This solution is presented in detail in Appendices A and B, with examples comparing solutions for measured nonlinear envelopes for tuff with solutions using simple straight line approximations.

During this investigation we discovered that the assumption that both the elastic and plastic components of ε_z are zero imposes constraints on the range of material parameters for which this solution is valid [4]. It is not valid for materials having small Poisson's ratio and small friction angle, such as SRI RMG 2C2 and tuff. The closed-form solution is valid, however, for materials such as 6B rock simulant and has been used successfully to predict tunnel closure measured in laboratory tests on samples of 6B rock simulant [2]. Tunnel closures computed for SRI RMG 2C2 using

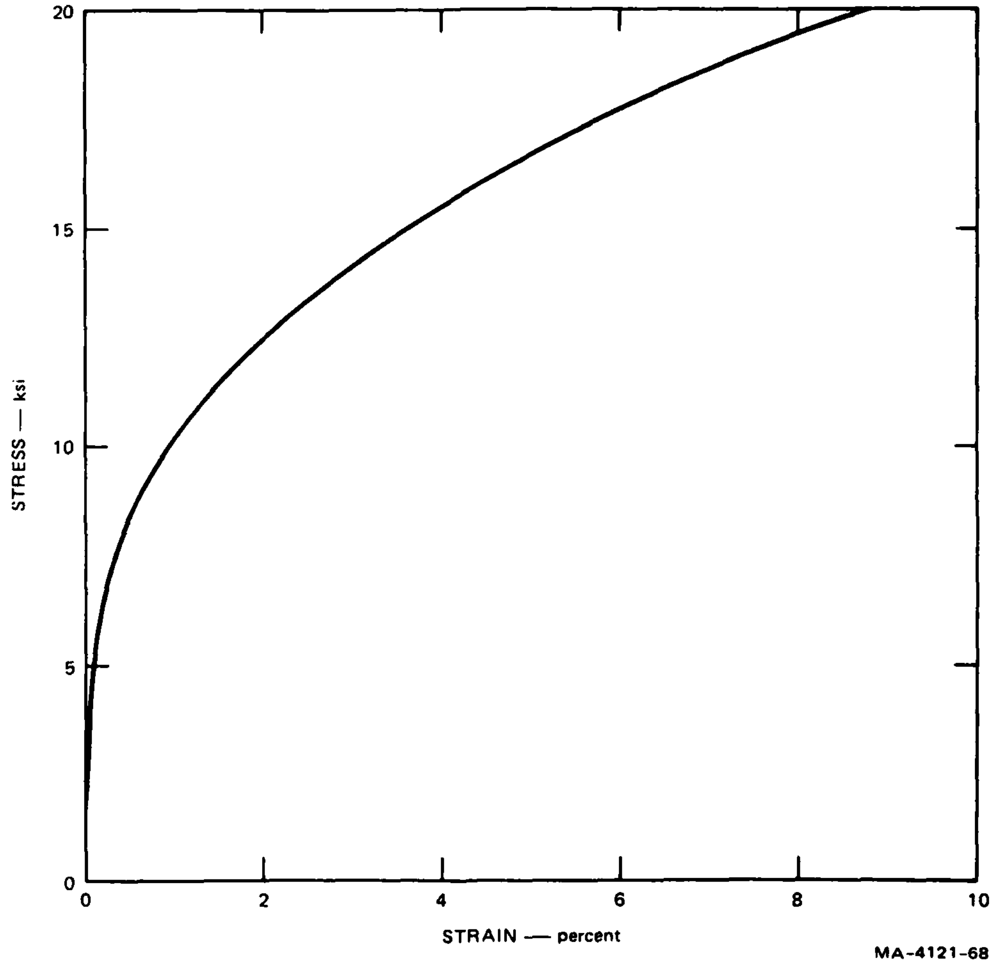

FIGURE 2.2 UNIAXIAL STRESS-STRAIN CURVE FOR Aℓ 6061-T0 IN COMPRESSION

the closed-form solution will be compared with numerical results to study the feasibility of using the closed-form analysis to determine design strengths of deep-based structures in soft materials like SRI RMG 2C2.

2.1.1 Solution for Strain Hardening Liner

For a liner to exert a constant pressure against the wall of the tunnel during deformation, as assumed in the original solution [1,3], the liner must be fabricated from a rigid, perfectly plastic material. The 1015 steel used as a liner material in some of the tests may be idealized as such a material, but a rapidly hardening material such as 6061-T0 aluminum cannot, as can be seen from the curve for engineering stress versus engineering strain shown in Figure 2.2. This curve was obtained from several tests performed in compression on standard solid cylindrical uniaxial stress specimens. The specimens were cut from tubing material used in the WES models (Chapter 7), with the specimen axis in the hoop direction.

To incorporate the increase in internal pressure with tunnel closure as the liner strain hardens, we use the simple hoop equations, neglecting variations through the thickness of the liner wall. Then the circumferential strain in the liner is $[\Delta D/D][1 + (h/2a)]$ where $\Delta D/D$ is the tunnel closure and a/h is the mean-radius-to-wall-thickness ratio of the tunnel liner. The hoop stress σ_θ is then found from the stress-strain curve given in Figure 2.2, and the pressure on the tunnel wall supplied by the liner is $P_i = 2\sigma_\theta h/D$.

To calculate the tunnel closure $\Delta D/D$ that starts this procedure, we must know the load and resulting liner pressure P_i. Thus, in general an iterative procedure must be used to determine both the tunnel closure and the pressure P_i compatible with this closure. However, the scheme actually used is simpler: the far-field pressure is increased from zero in increments of 100 psi (0.69 MPa), and the value of the internal pressure used in the calculation of $\Delta D/D$ is that which corresponds to the previously determined value of tunnel closure. Although the values of internal pressure and tunnel closure computed this way are slightly out of step, the errors are small.

2.1.2 Results

We made four calculations of tunnel closure versus applied pressure using the tunnel closure formula obtained from the closed-form solution. The calculated tunnel closure versus applied pressure curves are shown in Figure 2.3. In computing $\Delta D/D$, we took D to be the inside diameter of the tunnel liner.

In the first three calculations we used the solution for strain hardening liners to determine closure of tunnels reinforced with 6061-T0 aluminum liners having mean-radius-to-wall-thickness ratios, a/h = 11.5, 6.5, and 4.0. In the fourth calculation we used the constant internal pressure solution to determine the closure of a tunnel reinforced with a 1015 steel liner having a/h = 18. The value of the constant internal pressure used was 2100 psi (14.5 MPa), which corresponds to a yield stress of 38 ksi (0.26 GPa). This liner has the same design strength, 0.5 kbar (50 MPa), as the 6061-T0 aluminum liner of intermediate thickness.

The tunnel closure curves shown in Figure 2.3 show how the strength of the liner influences tunnel closure. The closure for each liner at its design strength is between 2 and 2.5 percent, only about half that computed using the closed-form solution at the same pressure levels in nominal tuff. This is not surprising since the unconfined compressive strength of SRI RMG 2C2 is more than twice the estimated compressive strength of tuff used to determine the design strengths of the liners. Further, comparing the steel and aluminum liners of equal strength, we see that we must account for strain hardening of the aluminum liners when analyzing our experimental data.

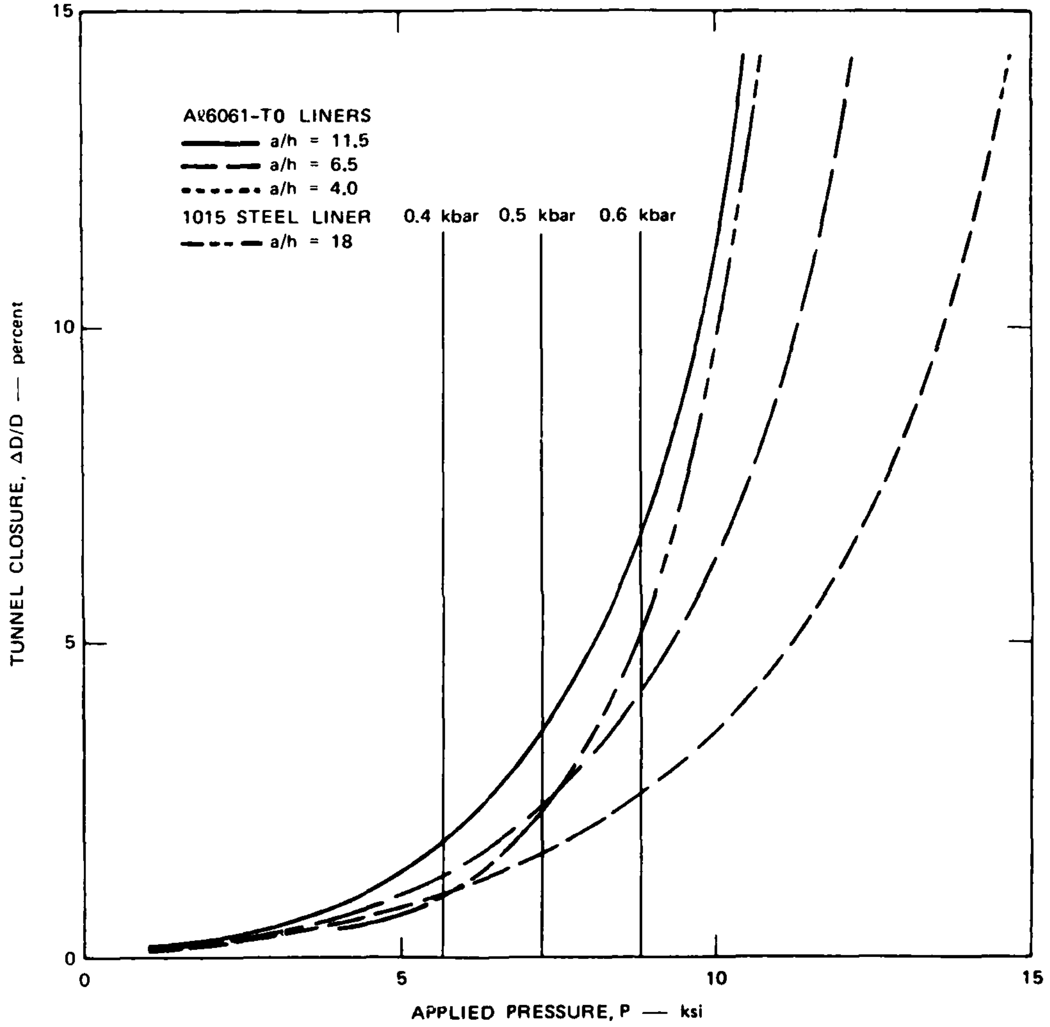

MA-4121-150A

FIGURE 2.3 CALCULATED TUNNEL CLOSURE VERSUS APPLIED PRESSURE CURVES USING CLOSED-FORM SOLUTION THAT NEGLECTS OUT OF PLANE PLASTIC STRAIN

2.2 NUMERICAL SOLUTION

In addition to our closed-form analysis we performed numerical calculations using the finite element code NONSAP. Our numerical analysis allowed us to model laboratory and field conditions more accurately than the closed-form analysis presented above. We used two mesh configurations, both comprising axisymmetric eight-node parametric elements. The first mesh, shown in Figure 2.4, models a disc cut from the center of our laboratory specimen. The loading, P_o, is applied at the outer boundary of the disc. To obtain a plane strain solution, we impose the constraint $\varepsilon_z = 0$. This solution is to be compared with the closed-form plane strain solution and will also serve as a baseline for our other numerical results. Imposing the constraint $\varepsilon_z = P_o/3K$, where K is the bulk modulus, allows us to approximate the laboratory conditions. This value of strain agrees with that in the far field, where the stresses are purely isotropic. We also used this mesh for our calculations of tunnel closure for end-on loading in the field. For this calculation we imposed the conditions $\varepsilon_z = P_o\ (1 + \nu)(1 - 2\nu)/(1 - \nu)E$ and zero radial displacement at the disc's outer boundary to model the kinematic field around the tunnel. These match the conditions in the far field and correspond to uniaxial compression in the direction of the tunnel axis.

The second mesh configuration, shown in Figure 2.5, models a sphere cut from our laboratory specimen. The loading, P_o, is applied on the spherical surface of the mesh. An advantage of this mesh is that no assumptions of kinematic behavior are necessary. The values of tunnel closure reported for the calculation using this mesh are those computed at the middle of the tunnel (at the bottom of the mesh), which is the location at which tunnel closure is determined in the laboratory tests.

The liner elements shown in Figures 2.4 and 2.5 model a 6061-T0 aluminum liner having a/h = 6.5. The constitutive behavior for these elements is determined by the bilinear fit to the measured stress-strain curve shown in Figure 2.6 and the Mises yield condition.

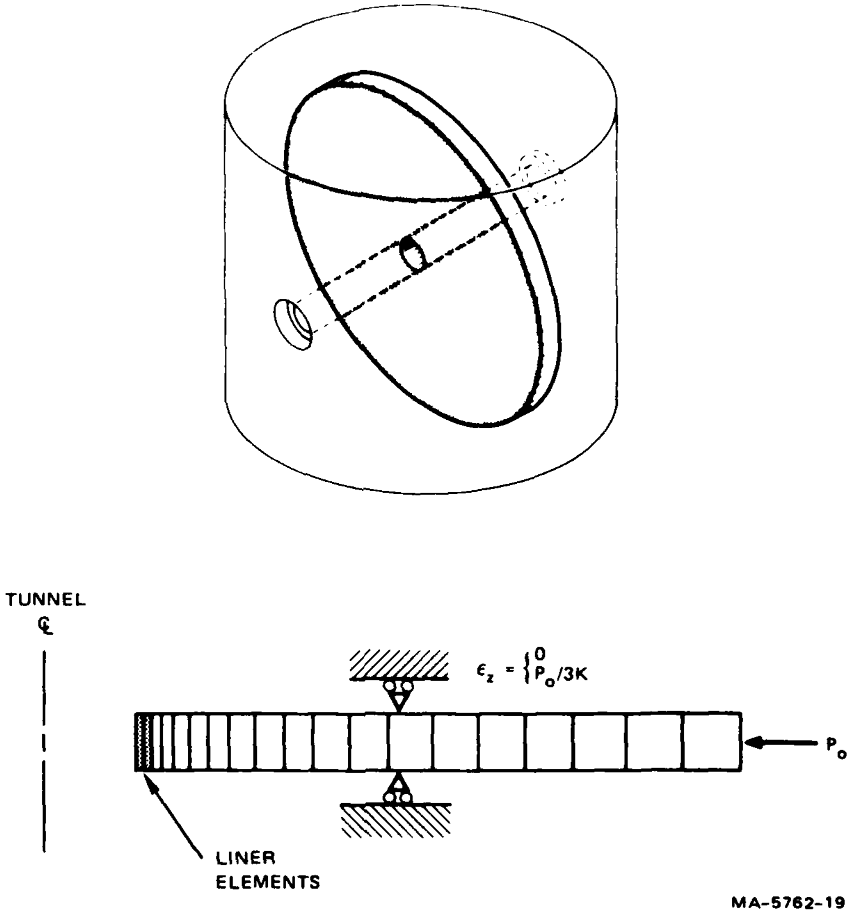

FIGURE 2.4 FINITE ELEMENT MESH THAT MODELS THIN DISC CUT FROM CENTER OF LABORATORY SPECIMEN

Elements are drawn to scale.

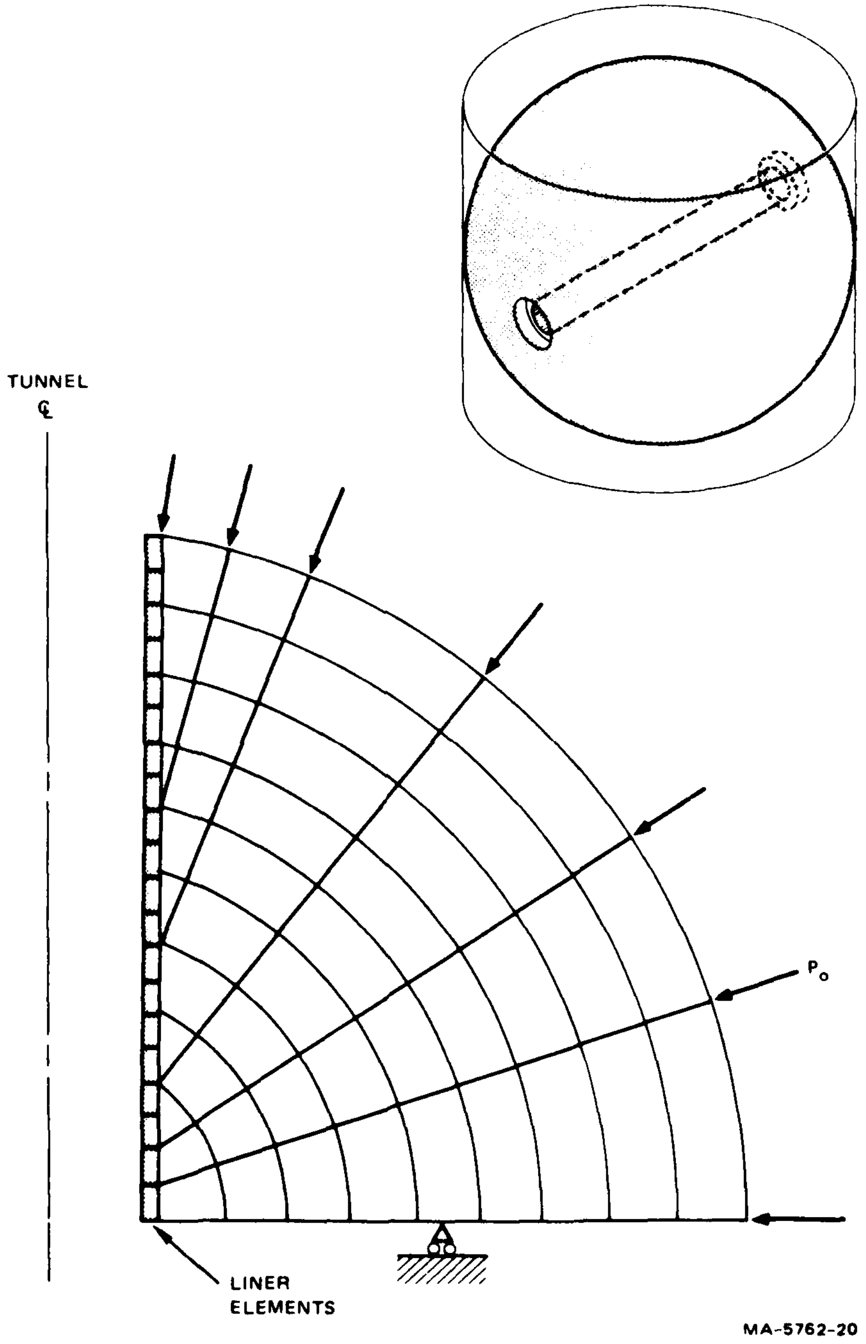

FIGURE 2.5 FINITE ELEMENT MESH THAT MODELS SPHERE CUT FROM LABORATORY SPECIMEN

Elements are drawn to scale.

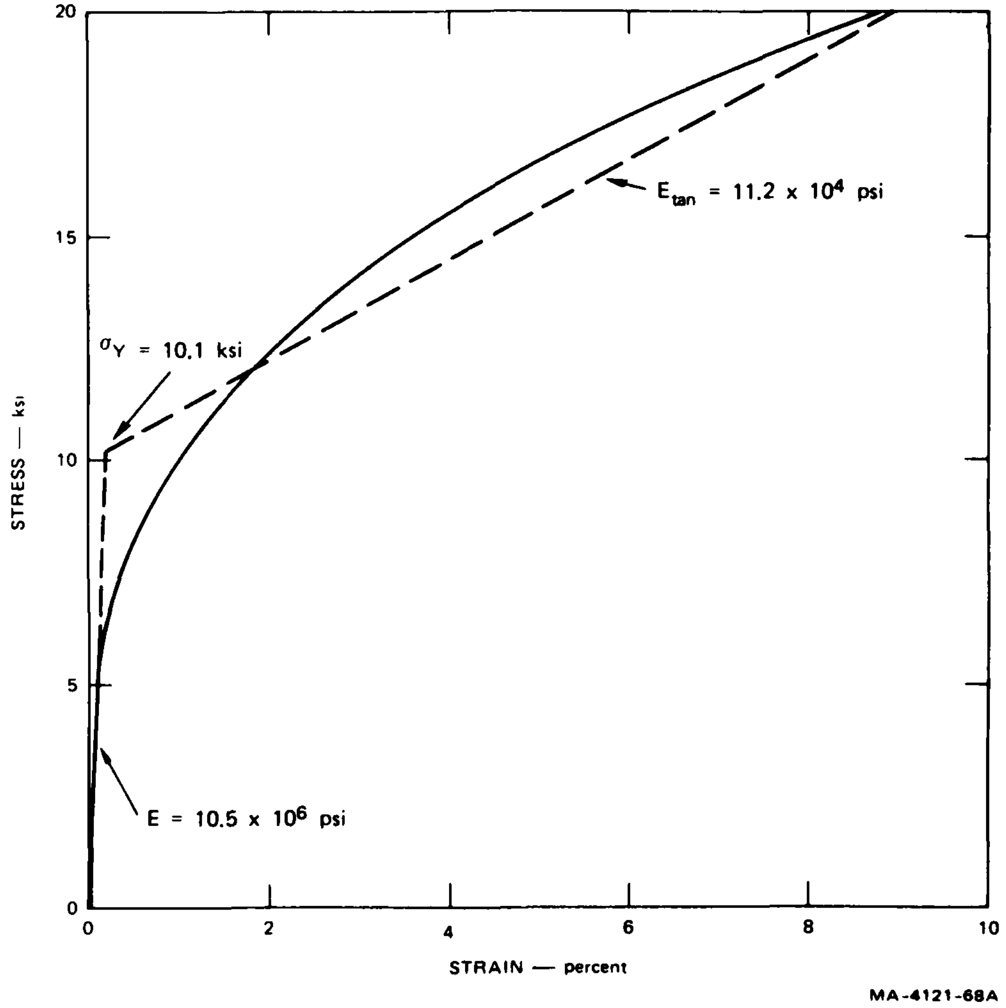

FIGURE 2.6 BILINEAR APPROXIMATION OF THE UNIAXIAL STRESS-STRAIN CURVE FOR Aℓ 6061-T0 IN COMPRESSION

2.2.1 Code Verification

We performed three calculations to check our numerical procedures. All used the discoid mesh. The first was a plane strain calculation performed to verify the Mohr-Coulomb constitutive package added to NONSAP by SRI International.* The results of this calculation were compared with a closed-form solution. For the material and loading parameters chosen, the stress state moved from one face of the failure surface to an adjacent face. The numerical results show excellent agreement with the closed-form solution when the stress state is on either face of the failure surface as well as when it lies on the edge of the failure surface joining the two adjacent faces [4].

The second calculation investigated the influence of the ratio of the mesh radius to the tunnel radius on the computed tunnel closure. Laboratory experiments performed previously [2] showed that increasing the ratio of specimen diameter to tunnel diameter from 6.4 to 12.8 does not appreciably affect the measured tunnel closure. In this second calculation, then, we increased the mesh-radius-to-tunnel-radius ratio from 6.4 to 12.8. The resulting tunnel closure was about 7.5 percent smaller than for the small mesh, which was consistent with our experimental measurements.

In the third calculation, we studied the effect of changing the element order. For this calculation, we replaced our eight-node isoparametric elements with four-node isoparametric elements of the same size. The difference in tunnel closure results was small, less than 1.5 percent, indicating that element order has little effect on our results.

---

*Adding the Mohr-Coulomb constitutive package to NONSAP as well as obtaining the closed-form results were completed by L. E. Schwer and A. L. Florence as part of an internal research and development project.

2.2.2 Results

We performed four calculations to determine closure of tunnels lined with a 6061-T0 aluminum liner having $a/h = 6.5$. The first, using the discoid mesh, was a plane strain calculation that served as a baseline for our other calculations; it was also compared with our closed-form plane strain solution. The second and third calculations were performed to model our isotropic laboratory experiments. In one, we used the discoid mesh and the condition $\varepsilon_z = P_o/3K$ to account for the three-dimensional aspects of our laboratory specimen. In the other, we used the spherical mesh and traction boundary conditions. The fourth calculation was performed to simulate end-on loading of a structure in the field.

Figure 2.7 compares the tunnel closures from our plane strain calculation with tunnel closures calculated using the closed-form plane strain analysis presented earlier. Although both closure curves result from plane strain analyses, the closed-form analysis assumes, incorrectly, that both the elastic and plastic components of ε_z vanish individually. Because the closed-form analysis does not account for the contribution to tunnel closure of plastic flow in the out-of-plane direction, it overestimates the pressure required to obtain a given closure. For example, for a tunnel closure of 5 percent, the closed-form analysis predicts a loading pressure 20 percent greater than the numerical analysis. This difference is significant because it indicates that structures designed using the closed-form analysis will fail before the design load is reached.

The tunnel closures from the two calculations of our isotropic loading experiments are shown in Figure 2.8. For comparison, the plane strain tunnel closure as well as experimental data are also plotted. The effect of modeling the three-dimensional loading of our laboratory specimen is to shift the closure curves to the right of the plane strain closure curve. The calculation using the spherical mesh gives slightly less closure than the discoid mesh, but the difference between the two

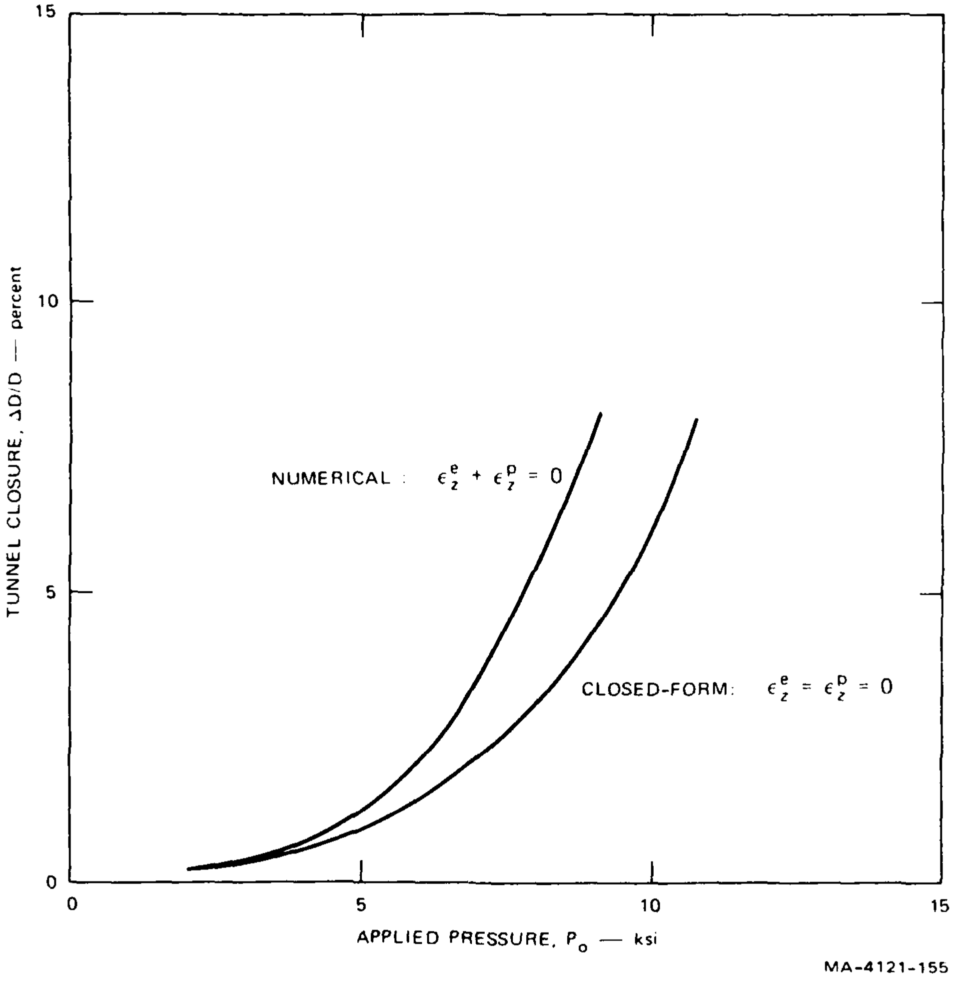

FIGURE 2.7 COMPARISON OF PLANE STRAIN TUNNEL CLOSURE VERSUS APPLIED PRESSURE FROM NUMERICAL AND CLOSED-FORM SOLUTION. CLOSED-FORM SOLUTION NEGLECTS OUT-OF-PLANE PLASTIC STRAIN

Axisymmetric loading of SRI RMG 2C2, Aℓ6061-TO liner having a/h = 6.5.

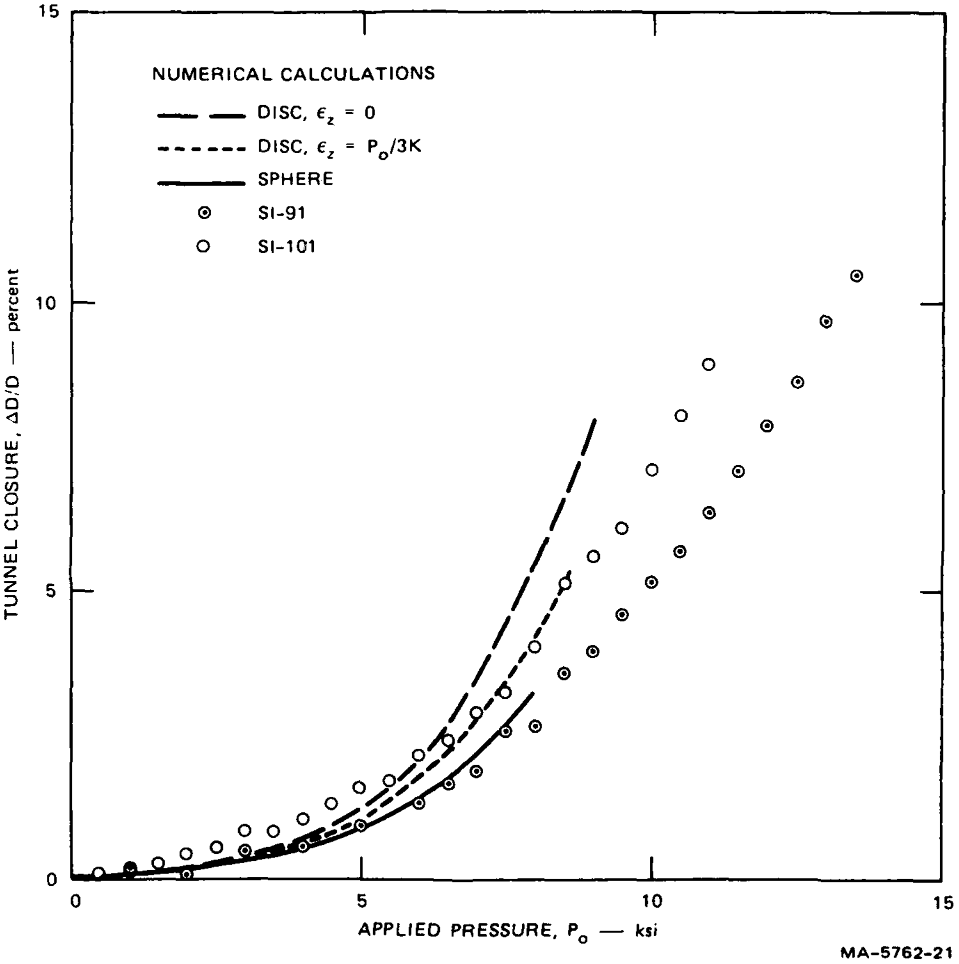

FIGURE 2.8 COMPARISON OF TUNNEL CLOSURE VERSUS APPLIED PRESSURE RESULTS FROM THREE FINITE ELEMENT CALCULATIONS AND TWO LABORATORY TESTS

Isotropic loading of SRI RMG 2C2, Aℓ 6061-T0 liner having a/h = 6.5

is about the same as the scatter in the experimental data. We may conclude, therefore, that the simpler discoid mesh with appropriate ϵ_z constraint is suitable for computing tunnel closures in our laboratory specimens.

The results of our fourth calculation, simulation of end-on loading of structures in the field, are shown in Figure 2.9. For comparison, the results of calculating the isotropic laboratory test are also plotted. Both calculations were performed using the discoid mesh. Tunnel closures for end-on loading are plotted as a function of the applied pressure, P_o, and also as a function of the induced radial pressure at the outer boundary of the mesh, P_r. The tunnel closure curve for the laboratory experiment lies between the two end-on loading curves. From these results we conclude that, while the isotropic laboratory test provides symmetric tunnel response as in end-on loading, substantial theoretical extrapolation of rock response is needed to predict response to end-on loading.

2.3 SUMMARY

In summary, we have accomplished the following theoretical results:

(1) We expanded our previous closed-form solution to include strain-hardening tunnel liners and nonlinear failure envelopes.

(2) We showed that the closed-form solution is not the correct plane strain solution for materials like SRI RMG 2C2. Further, for these materials, use of the closed-form solution in design of deep-based structures overestimates the pressure that produces a given closure.

(3) We performed calculations using discoid and spherical meshes that successfully predicted tunnel closures measured in our isotropic loading laboratory experiments.

(4) We performed a calculation that simulated end-on loading and showed that even though both end-on and isotropic loading produce axisymmetric pressure on the tunnel, substantial theoretical extrapolation of rock response is needed to predict tunnel closures for end-on loading.

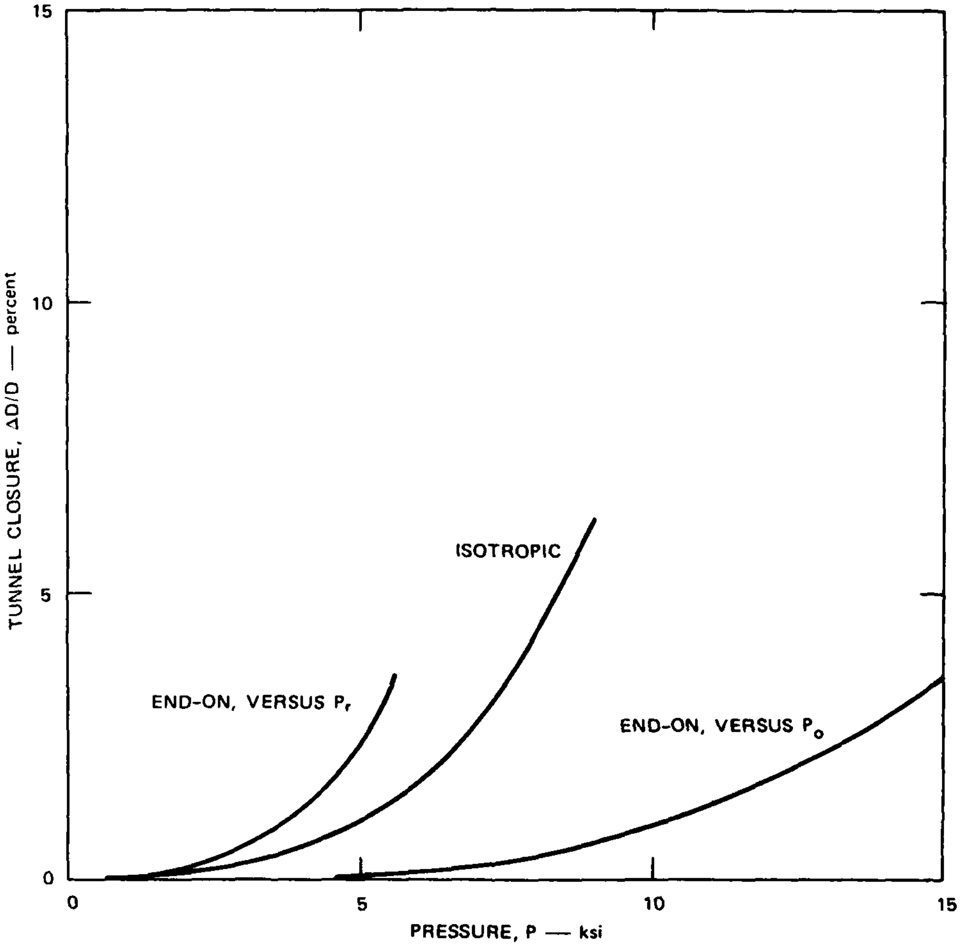

MA-4121-157

FIGURE 2.9 COMPARISON OF TUNNEL CLOSURE VERSUS PRESSURE FOR END-ON AND ISOTROPIC LOADING

Tunnel closures for end-on loading plotted against loading pressure, P_o, and induced radial pressure, P_r. SRI RMG 2C2, Aℓ6061-T0 liner having a/h = 6.5.

3. TESTING MACHINES AND SPECIMENS

The testing machines and specimens used in the laboratory experiments have been described in detail previously [2]. The general approach in the experiments is to load the specimens to simulate the stresses that exist around a buried structure that is subjected to a nuclear ground shock in the field. Two different loading types are applied: isotropic loading and uniaxial strain loading. For isotropic loading, the vertical and lateral pressures applied to the specimen are equal. This type of loading simulates the symmetric stress field around a buried structure in the field subjected to end-on loading. For uniaxial strain loading the lateral pressure is varied with vertical pressure such that the lateral boundary of the specimen undergoes no radial displacement. This simulates the constraint provided by the surrounding rock during the side-on loading of a buried structure in the field.

3.1 DYNAMIC TESTING MACHINE

The basic operating feature of the dynamic testing machine is the controlled release of explosive gases from a vented chamber charged with low-density explosive (a mixture of PETN and microspheres). The machine has the capability to apply isotropic, uniaxial strain or more general triaxial loadings that may be imposed on deep buried structures under nuclear attack. During the current program, we modified the test procedure and the testing machine itself to eliminate oscillations in the pressure pulses that load the specimen. A detailed discussion of the pressure pulse oscillations and the diagnostic procedure that led to the modifications is given in Appendix C.

An assembly drawing of the dynamic testing machine in the triaxial loading configuration is shown in Figure 3.1. Independent control of vertical and lateral pressures is possible because loading is applied

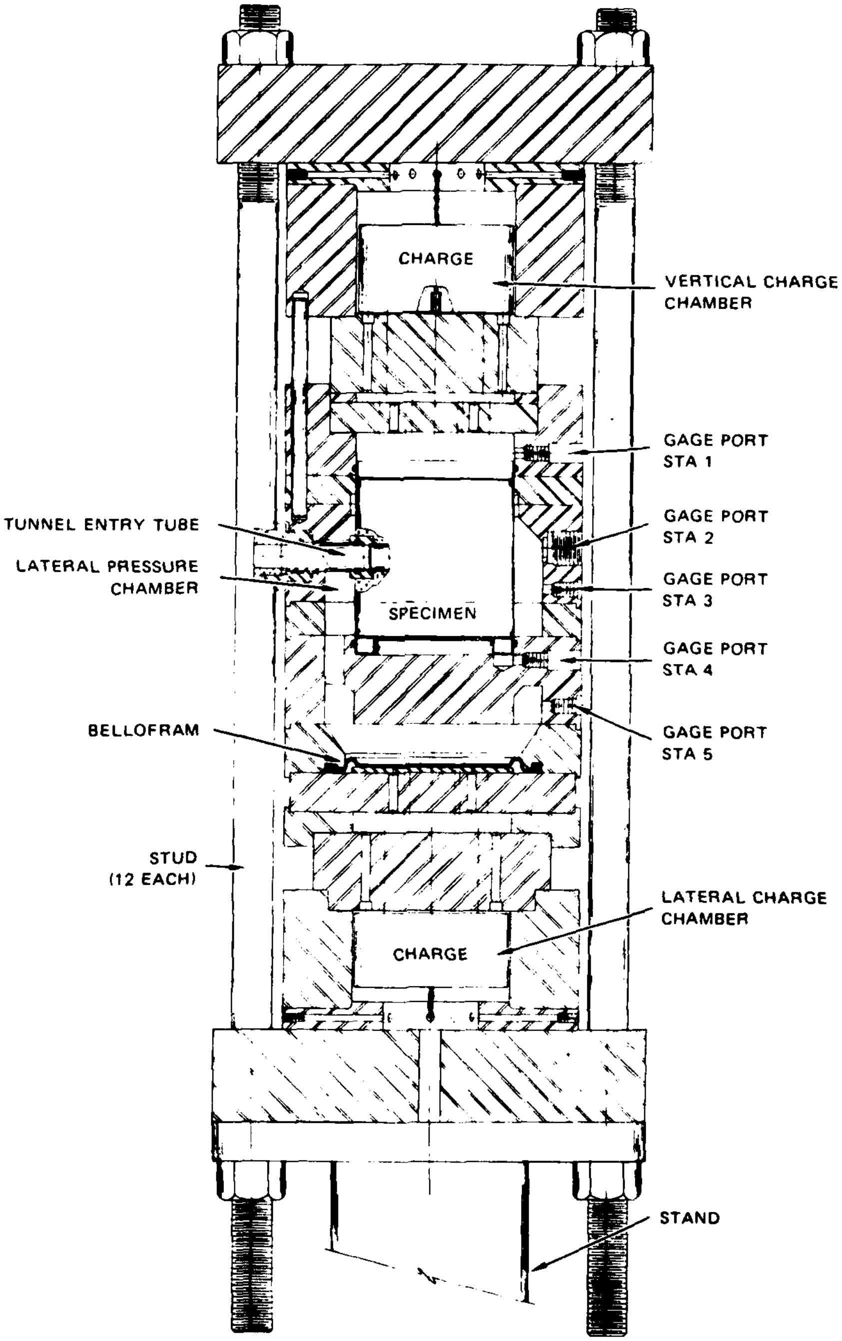

FIGURE 3.1 DYNAMIC TESTING MACHINE–TRIAXIAL LOADING CONFIGURATION

by two separate explosive chambers. Figure 3.2 shows records of both the vertical and lateral loading pressure pulses from a dynamic uniaxial strain loading test, DUX-74. Risetime for the pressure pulses is about 4-1/2 ms; the total pulse duration is about 50 ms.

Figure 3.3 shows an assembly drawing of the dynamic testing machine in the isotropic loading configuration. This configuration is essentially the same as the triaxial configuration, except that there is only one explosive chamber and one expansion chamber.

Figure 3.4 shows records of the loading pressure pulse from a dynamic isotropic loading test, DI-65. The risetime of the pressure pulse is 2 ms; the decay time is about 25 ms. The pressure pulse shown in Figure 3.4(c) was obtained before we began using lead shot to damp out the high frequency oscillations, as described in Appendix C.

3.2 STATIC TESTING MACHINE

The static testing machine is used to apply triaxial loading on the specimens. The loads are applied hydraulically by high-pressure hand pumps. Figure 3.5 shows an assembly drawing of the machine.

3.3 SPECIMENS

The specimens tested in this program are right circular cylinders of SRI RMG 2C2, 4 inches (0.1 m) in diameter and 4 inches (0.1 m) high. They are cut from a longer 4-inch- (0.1-m) diameter cast cylinder and ground to length. A 0.625-inch- (16-mm) diameter tunnel is drilled through the specimen along a diameter at midheight. The grout used to fabricate the rock specimens, SRI RMG 2C2, is a tuff simulant consisting of the following components:

Portland cement (type 1 or class G)	31.14 wt%
Monterey sand (20-40 mesh)	20.86
Barium sulfate	19.89
Betonite	2.73
Concrete friction reducing compound 2 (detergent powder)	0.076
Water	25.31

The specimens were tested in the fully saturated condition by keeping them submerged in water until they are ready for test. Exposure time to the atmosphere during assembly into the air tight copper top and bottom caps and central rubber membrane is at most five minutes.

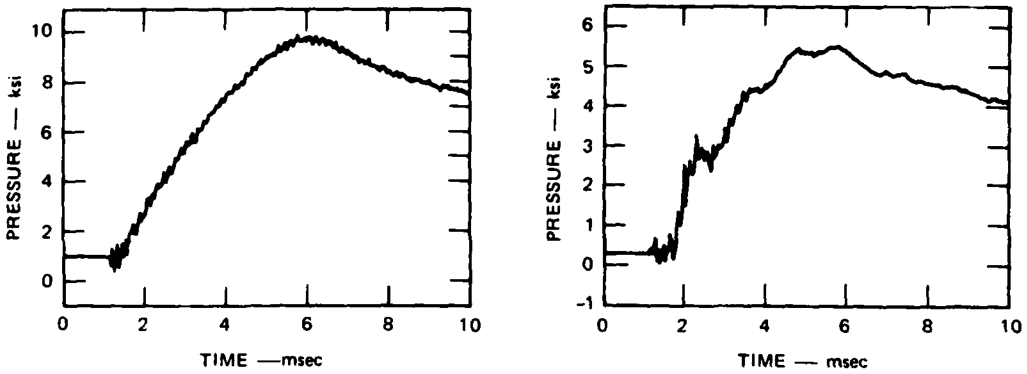

(a) P1-GAS PRESSURE ABOVE SPECIMEN

(c) P2-OIL PRESSURE IN LATERAL CHAMBER (NEAR CENTER)

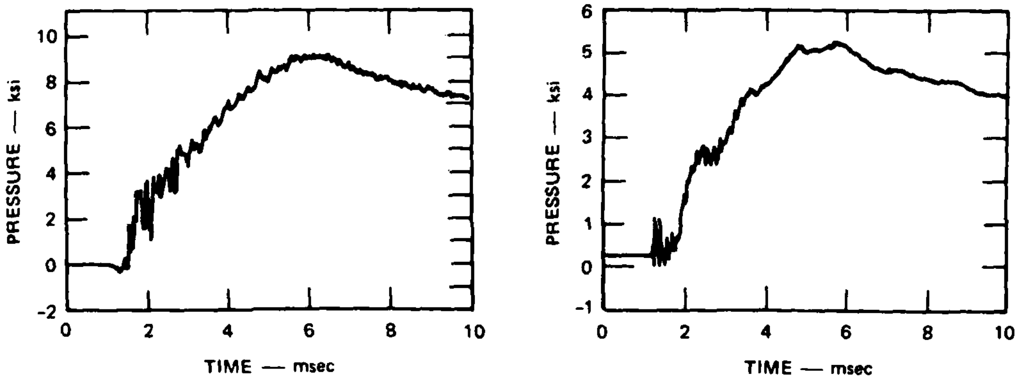

(b) P4-OIL PRESSURE BELOW SPECIMEN

(d) P3-OIL PRESSURE IN LATERAL CHAMBER (SLIGHTLY LOWER)

MA-4121-75

FIGURE 3.2 PRESSURE DATA FROM UNIAXIAL STRAIN LOADING TEST DUX-74

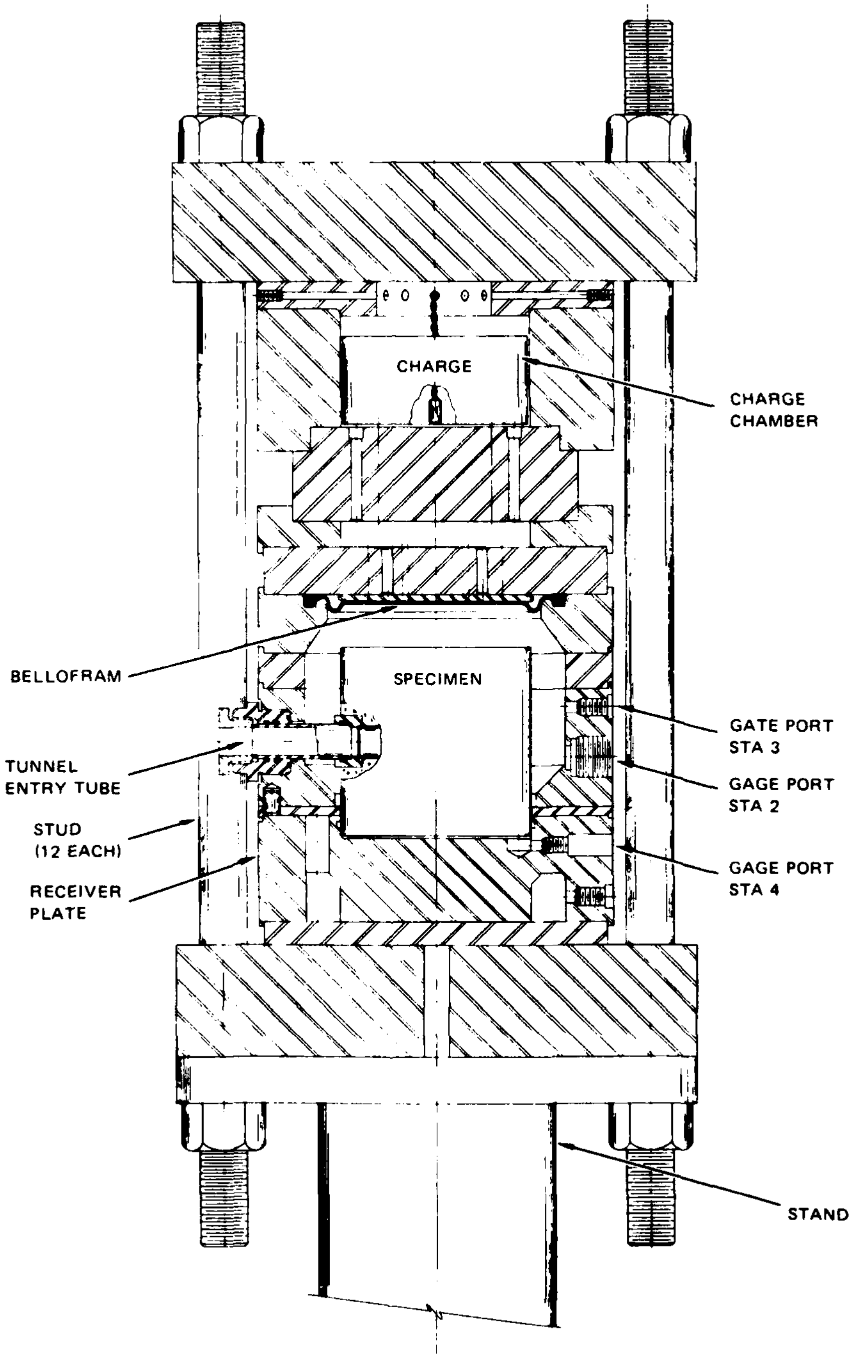

FIGURE 3.3 DYNAMIC TESTING MACHINE–ISOTROPIC LOADING CONFIGURATION

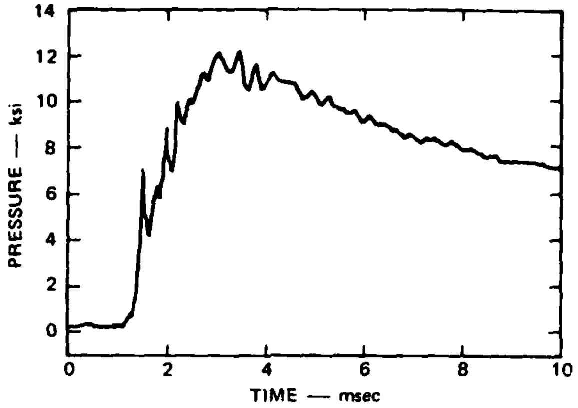

(a) P2-OIL PRESSURE IN LATERAL CHAMBER (JUST BELOW MIDHEIGHT OF SPECIMEN)

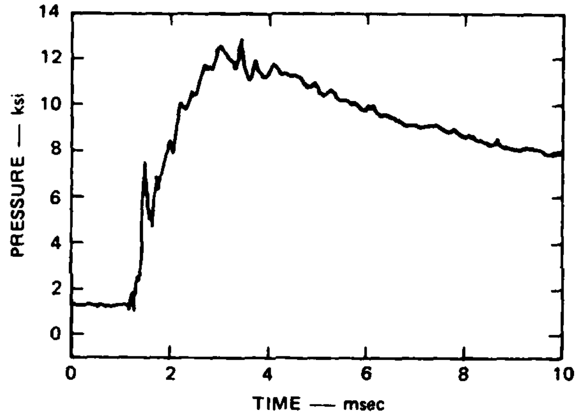

(b) P3-OIL PRESSURE IN LATERAL CHAMBER (JUST ABOVE MIDHEIGHT OF SPECIMEN)

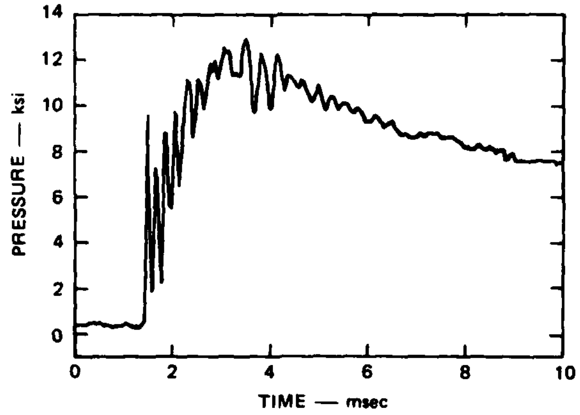

(c) P4-OIL PRESSURE BELOW SPECIMEN

MA-4121-152

FIGURE 3.4 PRESSURE DATA FROM ISOTROPIC LOADING TEST DI-65

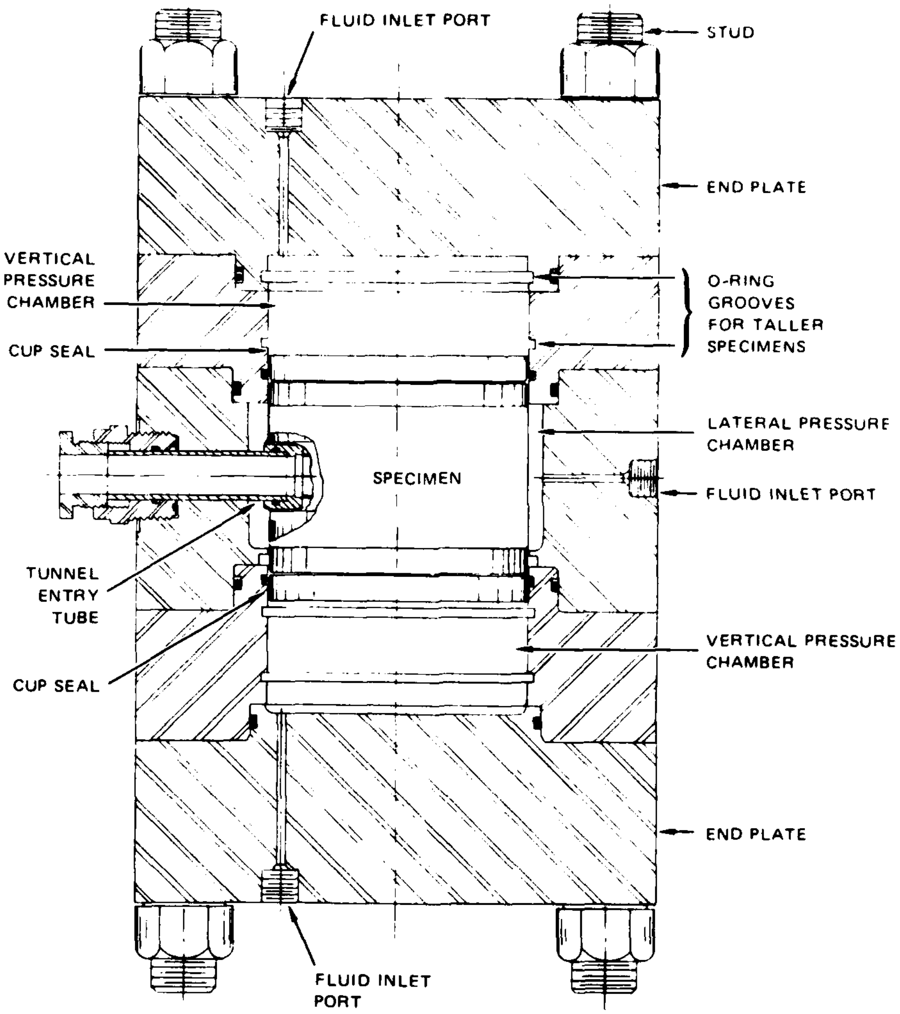

(c)

MA-3743-92A

FIGURE 3.5 STATIC TESTING MACHINE–TRIAXIAL LOADING CONFIGURATION

The tunnels in the rock specimens are reinforced with scale models of structures fielded in Mighty Epic. A typical scale model structure, a circumferentially stiffened cylindrical steel liner, is shown in Figure 3.6. The reinforcing tunnel liners are grouted into the rock specimen with hydro-stone.* Thickness of the hydro-stone layer is about 0.03 inches (0.75 mm). The ends of the tunnels are counterbored to a 1-1/8-inch- (29-mm) diameter to accept the end fittings that connect the tunnel to the outside of the testing machine through the access ports. The end fittings are also grouted into the rock specimen. The junctions of tunnel liner and end fittings are sealed with O-rings. If porewater is permitted to drain from the specimen, eight 1/32-inch- (0.8-mm) diameter holes are drilled through the wall of the tunnel liner near the ends of the tunnel. Any porewater that drains from the specimen seeps into the tunnel through these holes in the tunnel liner.

The specimen is sealed from the oil in the testing machine by enclosing the specimen in two copper cans. One encloses the top portion of the specimen and the other the bottom, as shown in Figure 3.7. Two strain gages are mounted on the upper copper can, and their outputs are used to determine the radial displacement of the lateral surface of the specimen. A Wilson seal is placed around the midsection of the sample to seal the end fittings, as shown in Figure 3.8. The Wilson seal consists of a section of a motorcycle inner tube with two small holes cut in the center.

---

* Hydro-stone is a United States Gypsum Company tradename for super strength gypsum cement.

MP-4121-41

FIGURE 3.6 CIRCUMFERENTIALLY STIFFENED STEEL LINER — a/h = 18 (5/8-INCH DIAMETER)

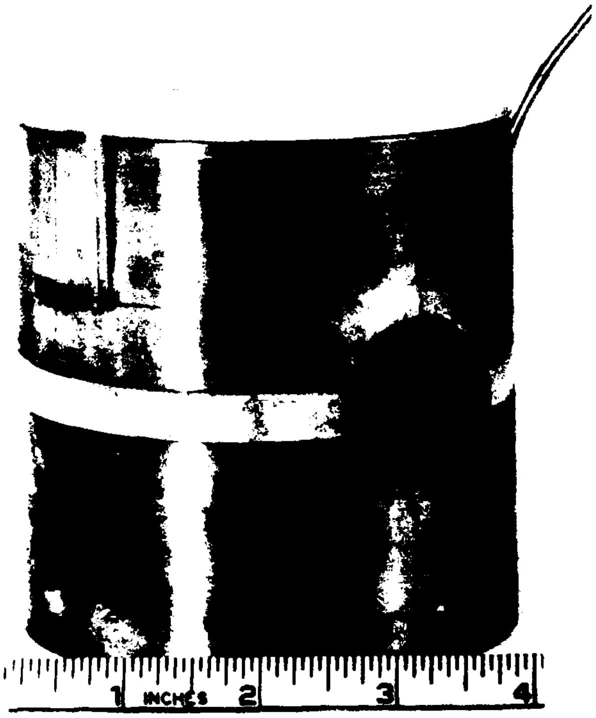

MP-4121-11

FIGURE 3.7 STRAIN GAGES ON COPPER CANS TO MONITOR LATERAL EXPANSION OF ROCK

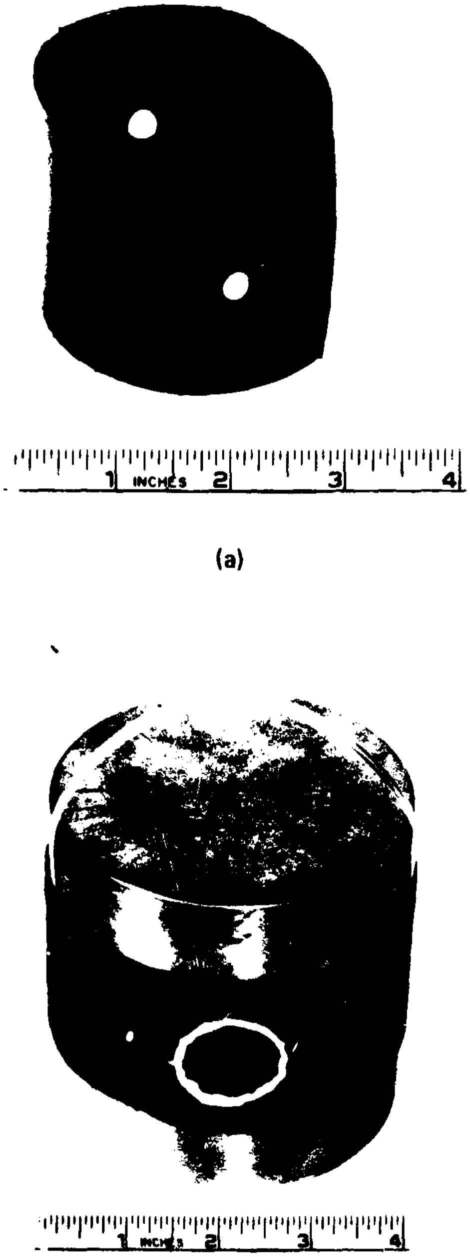

(a)

(b)

MP-3743-85

FIGURE 3.8 WILSON SEAL ASSEMBLY

4. ISOTROPIC LOADING EXPERIMENTS

4.1 STATIC TESTS

Static isotropic loading tests were performed on 4-inch- (0.1-m) diameter specimens of SRI RMG 2C2, whose tunnels were reinforced with 6061-TO Aluminum monocoque cylindrical shell liners having mean-radius-to-wall-thickness ratios, a/h = 4.0, 6.5, and 11.5. The specimens were fully water saturated. To avoid a buildup of porewater pressure, water was allowed to drain from the rock during the test. Previous tests on undrained specimens of saturated 6B rock simulant [2] showed anomalous tunnel liner deformation due to porewater migration under constant load.

In three of the tests, SI-77, SI-91, and SI-92, water was permitted to drain from the rock at only one end of the tunnel. In the other two tests, SI-99 and SI-101, water was permitted to drain from both ends of the tunnel. The presence of porewater pressure was evident in tests SI-91 and SI-92, in which water was permitted to drain from the rock at only one end of the tunnel. The tunnel liners in these two tests were the two weakest structures, having a/h = 6.5 (SI-91) and a/h = 11.5 (SI-92). The a/h = 6.5 liner had a characteristic porewater pressure bulge at the sealed end of the tunnel.

The a/h = 11.5 liner, shown in Figure 4.1, had a particularly mottled surface. A photographic history of the development of this surface as a function of load is shown in Figure 4.2 (the photographs were taken through a concave lens that fit inside the tunnel entry tube). Mottling of the surface began at a loading pressure of about 4 ksi (27.6 MPa). The amplitude of the waves gradually increased with pressure. Although this phenomenon is not understood, it does not appear to be the circumferential buckling observed in other experiments [2], since the waves are not uniform along the length. Similar bulging was observed in some of the static

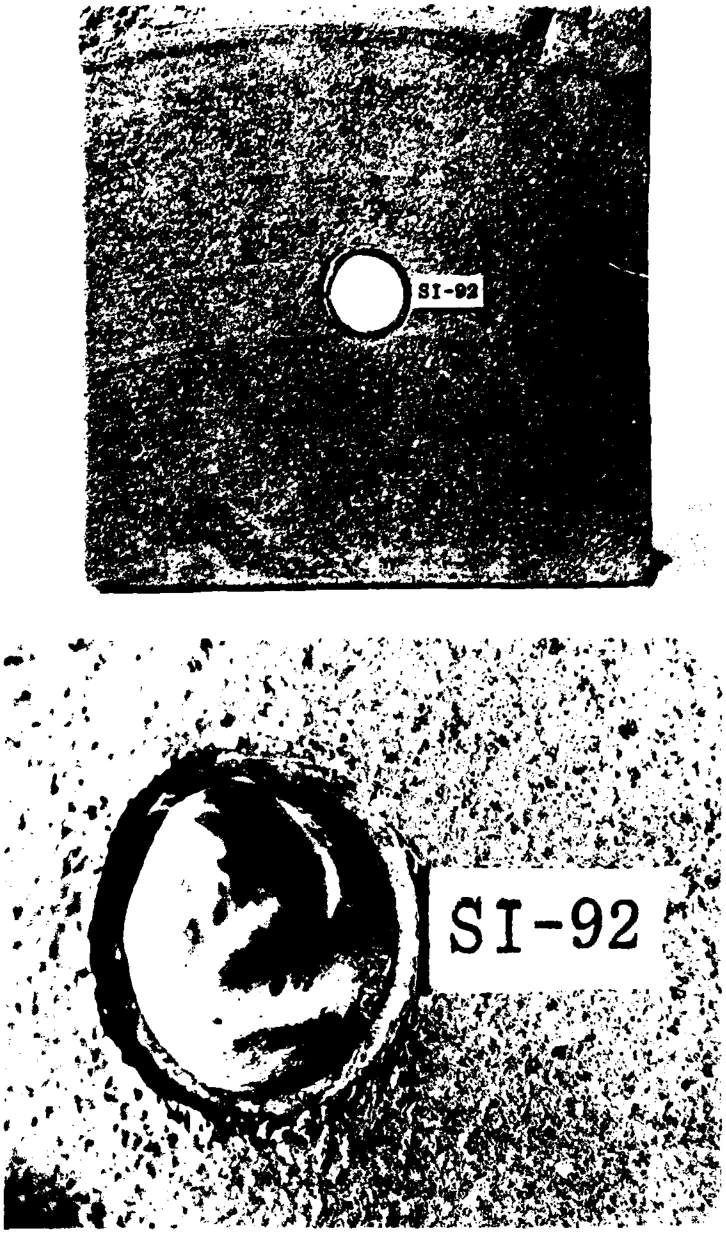

MP-4121-42

FIGURE 4.1 RESPONSE OF A MONOCOQUE Aℓ 6061-T0 LINER IN SRI RMG 2C2 TO STATIC ISOTROPIC LOADING — $a/h = 11.5$, $P_{max} = 10.5$ ksi, $\Delta D/D = 10.5\%$

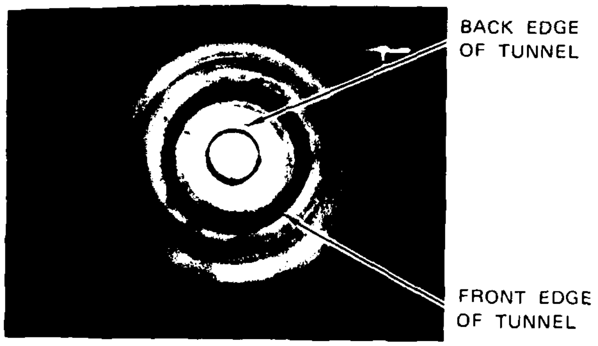

3 ksi, 0.5%

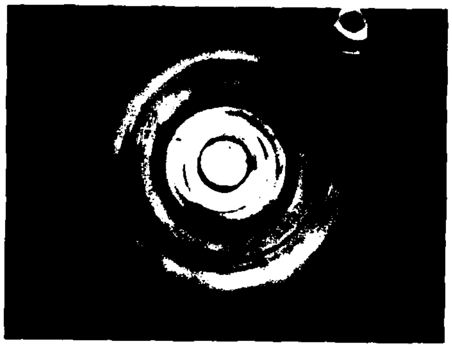

6 ksi, 2.3%

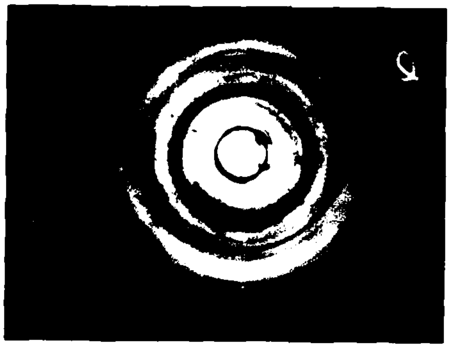

4 ksi, 1.0%

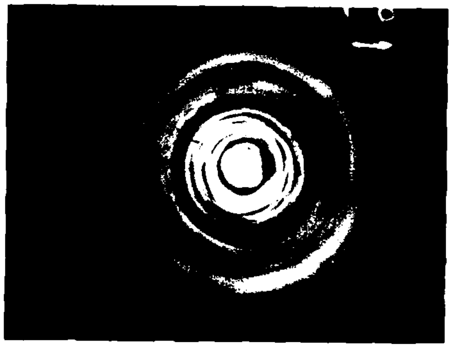

7 ksi, 3.4%

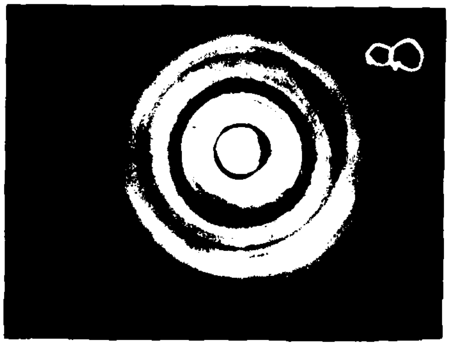

5 ksi, 1.5%

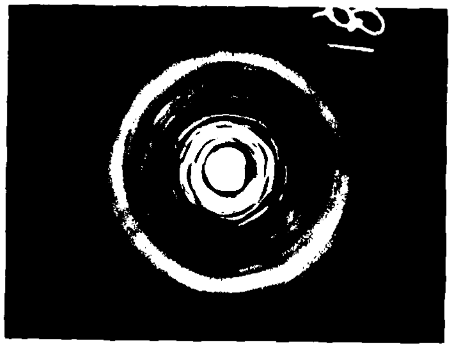

10 ksi, 9.1%

MP-4121-43

FIGURE 4.2 DEVELOPMENT OF MOTTLED SURFACE IN STATIC ISOTROPIC LOADING TEST, SI-92 — Aℓ 6061-T0 LINER WITH a/h = 11.5

uniaxial strain loading tests discussed in the next chapter. Allowing porewater to drain at both ends of the tunnel eliminated liner bulging in these tests also.

Figure 4.3 plots tunnel closure ΔD/D as a function of the applied pressure P for all five tests. Each value of tunnel closure plotted represents the average of the closures at the crown-invert, the springlines, and along a diameter at 45° (0.785 rad) to these two orientations. The data plotted in Figure 4.3 show that in the two tests in which water drained from the rock at both ends of the tunnel, SI-97 and SI-101, the closure is less than in tests of liners having equal strength, SI-77 and SI-91, but in which water drained at only one end of the tunnel. This difference in closure may, perhaps, be attributed to the greater porewater pressure around the tunnel liner in the specimens that were drained at only one end of the tunnel.

If we consider the tests in which water drained from only one end of the tunnel and those in which it drained from both ends as two separate groups (open symbols versus symbols containing dots), then the data from these five tests exhibit the expected trend. The stronger tunnel reinforcing structures (i.e., the liners having the smaller a/h values) suffer less closure than the weaker structures. The data from Test SI-77 do not support this trend entirely. At low applied pressures, the tunnel closure is greater than those from the two tests of weaker structures. However, at applied pressure greater than 8.5 ksi (58.6 MPa), the tunnel closure from SI-77 is less than those from the tests on weaker structures, as expected.

4.2 DYNAMIC TESTS

Dynamic isotropic loading tests were performed on specimens identical to those tested statically. As in the static tests, the specimens were fully water saturated; however, no provision was made for porewater

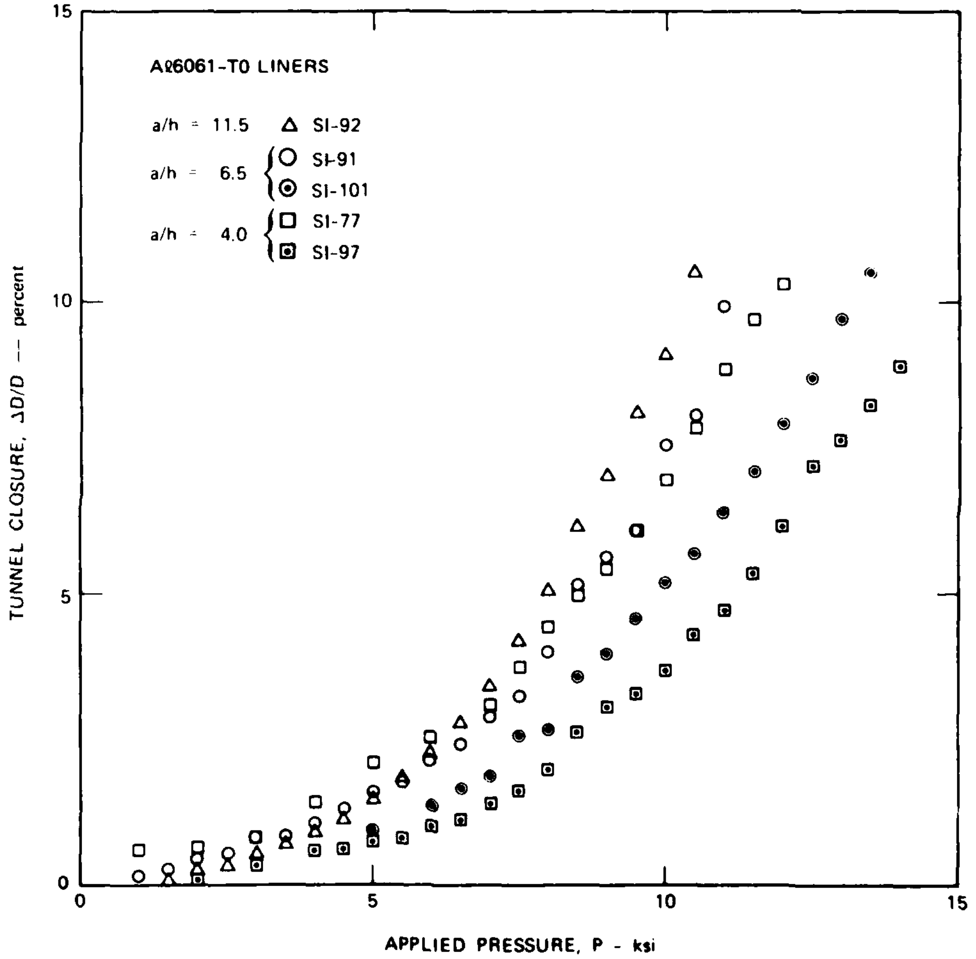

MA-4121-78

FIGURE 4.3 TUNNEL CLOSURE VERSUS APPLIED PRESSURE FOR STATIC ISOTROPIC LOADING OF SRI RMG 2C2 drainage. This better simulates drainage conditions during the dynamic, short-time loading of deep-based structures in the field. In the dynamic laboratory tests, the loading is also short; the pressure pulse has a 2-ms risetime and a 25-ms decay time. This is short enough that porewater migration can be neglected and provisions for porewater drainage are not necessary.

The tunnel closure data from the dynamic tests shown in Figure 4.4 are the residual tunnel closure obtained by measuring the diameter of the tunnel after the test and comparing it with the original diameter of the tunnel. We expect that residual closures are slightly smaller than closures measured while the specimen is under load, but we assume that this difference is small. Measurements of the tunnel diameter in specimens tested statically indicate that there is less than 10 percent difference between residual tunnel closure and tunnel closure at the peak loading pressure.

These residual dynamic tunnel closure data are plotted in Figure 4.4 as a function of the peak loading pressures. There are not sufficient dynamic data to determine the influence of tunnel liner strength on the tunnel closure. Of the limited data, the tunnel reinforced with the weakest liner suffered the least closure, and the tunnel reinforced with the strongest liner suffered the most. However, in every case the tunnel closure is very small and the difference in tunnel closure from one test to another is barely resolvable with the bore gage used to measure the tunnel diameter.

The striking result of the dynamic isotropic loading experiments is that the tunnel closures are very much smaller than those obtained in the static isotropic loading experiments. For example, a loading pressure of 11 ksi (76 MPa) produces a tunnel closure of about 1.5 percent in the dynamic tests and between 4.75 percent and 10 percent in the static tests, depending on the strength of the tunnel liner. In other words, the tunnel closures in the dynamic tests are less than one-third as large

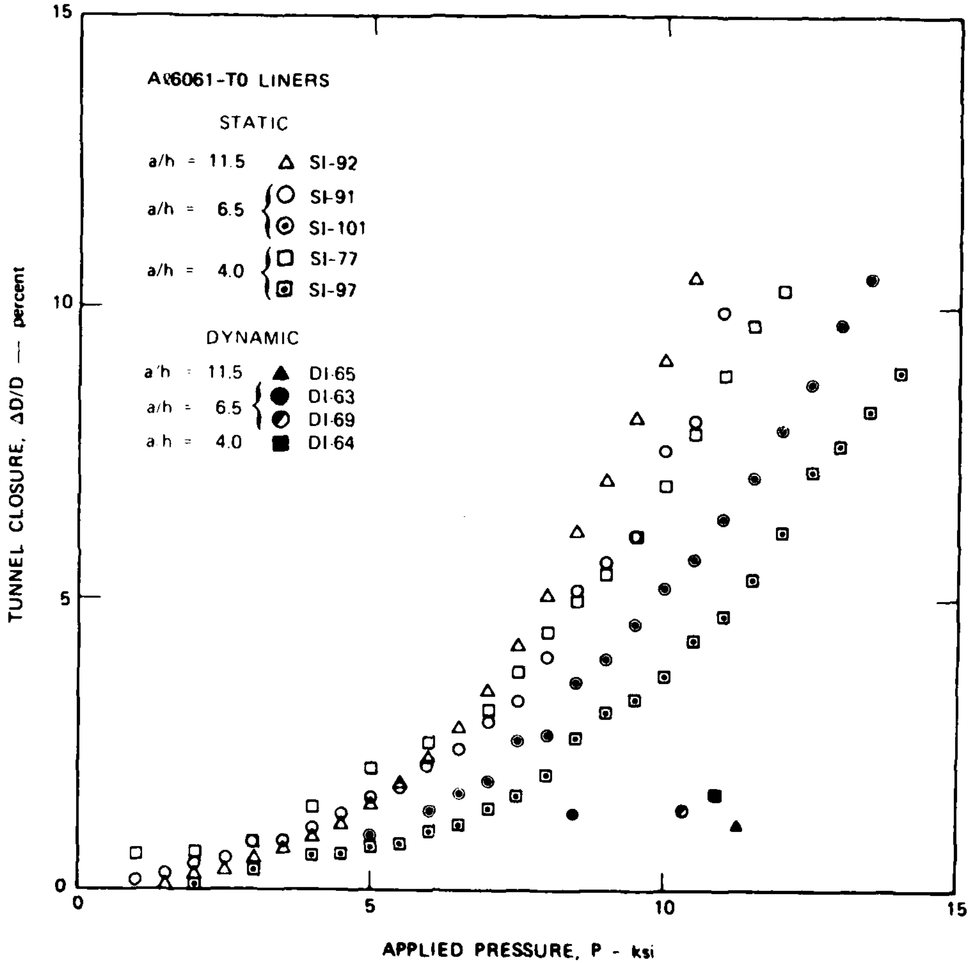

FIGURE 4.4 TUNNEL CLOSURE VERSUS APPLIED PRESSURE FOR STATIC AND DYNAMIC ISOTROPIC LOADING OF SRI RMG 2C2

as the tunnel closures in the static tests at 11 ksi (76 MPa). Interpreting the data another way, achieving a tunnel closure of about 1.5 percent in a static test will require an applied pressure of 5 to 7.5 ksi (34.5 to 52 MPa), depending on the strength of the structure. Achieving the same closure under dynamic loading will require an applied pressure between 8 and 11 ksi (55 and 76 MPa), probably closer to 11 ksi (76 MPa). Taking the upper limit on both the static and dynamic pressures, the applied loading pressure required to produce a tunnel closure of 1.5 percent in a dynamic test is about 1-1/2 times greater than that required in a static test.

One explanation for this large difference between static and dynamic tunnel closure is that porewater carries a greater proportion of the load in the undrained dynamic test than in the drained static test. Another possible explanation is that the deformation of the rock skeleton is strain rate dependent; at high strain rates the stress required for continued plastic flow is greater than at low strain rates. Therefore, in the dynamic tests, the rock material is able to carry the load while permitting smaller deformation than in the static tests.

4.3 CONCLUSIONS

The most striking conclusion to be drawn from the results of the isotropic loading experiments is that the tunnel closures in the dynamic tests are substantially smaller than those in the static tests. Although the data are limited, the results obtained indicate that the pressure required to achieve a 1.5 percent closure under dynamic loading is about 1-1/2 times greater than under static loading. This difference is attributed to the greater strain rate and porewater pressure in the dynamic tests. Therefore, for calculating tunnel closures in dynamic tests, the constitutive relations used in Chapter 2 to calculate static closures should be expanded to include strain rate and porewater effects.

5. UNIAXIAL STRAIN LOADING EXPERIMENTS

5.1 STATIC TESTS

Static uniaxial strain loading tests were performed on the same type rock specimens and aluminum liners as tested in the isotropic loading experiments. Two additional tests were performed with 1015 steel liners, one unstiffened and the other stiffened with external circumferential ribs. Both had a/h = 18. The hoop strength of the 1015 steel liners is about the same as that of the intermediate strength 6061-TO aluminum liner, having a/h = 6.5.

Porewater was permitted to drain from the specimen at both ends of the tunnel in tests SUX-95, SUX-96, SUX-98, SUX-99, and SUX-100 to eliminate liner bulging, as discussed in the previous chapter. The tunnel liners in these tests were one of each type: the unstiffened and stiffened steel liners and each of the three thicknesses of aluminum liners. In three earlier tests, SUX-78, SUX-93, and SUX-94 (the three aluminum liners), porewater was permitted to drain at only one end of the tunnel. In two of these earlier three tests, SUX-93 and SUX-94, significant porewater pressure was evident; the liners, having a/h = 11.5 and a/h = 6.5, bulged under porewater pressure loading at the sealed end of the tunnel, similar to the bulging observed in the early static isotropic tests.

The liners tested under uniaxial strain conditions ovalled without buckling, with the exception of the monocoque steel a/h = 18 liner, tested in SUX-95. This liner had a buckle along one springline, as shown in Figure 5.1. The development of the buckle as a function of load is shown in Figure 5.2. The surface of the liner ranges from smooth to mottled between P_V = 3 and 7.5 ksi (21 and 52 MPa). At P_V = 4 ksi (28 MPa), water drops appear at the holes drilled into the liner for drainage. At P_V = 9 ksi (62 MPa), a buckle at the springline is clearly visible and at P_V = 11 ksi (76 MPa), the buckle is well developed.

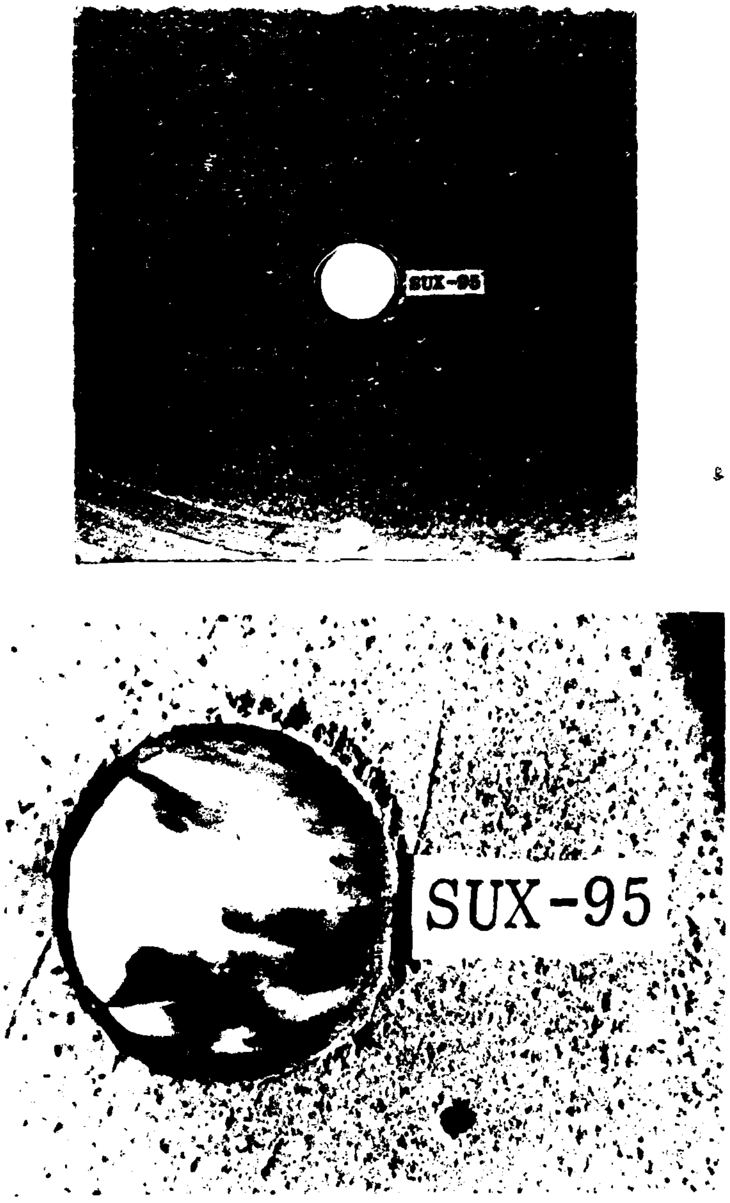

MP-4121-45

FIGURE 5.1 RESPONSE OF A MONOCOQUE STEEL LINER IN SRI RMG 2C2 TO STATIC UNIAXIAL STRAIN LOADING — $a/h = 18$, $P_{V\max} = 11{,}000$ psi, $\Delta D_V/D_V = 9.8\%$

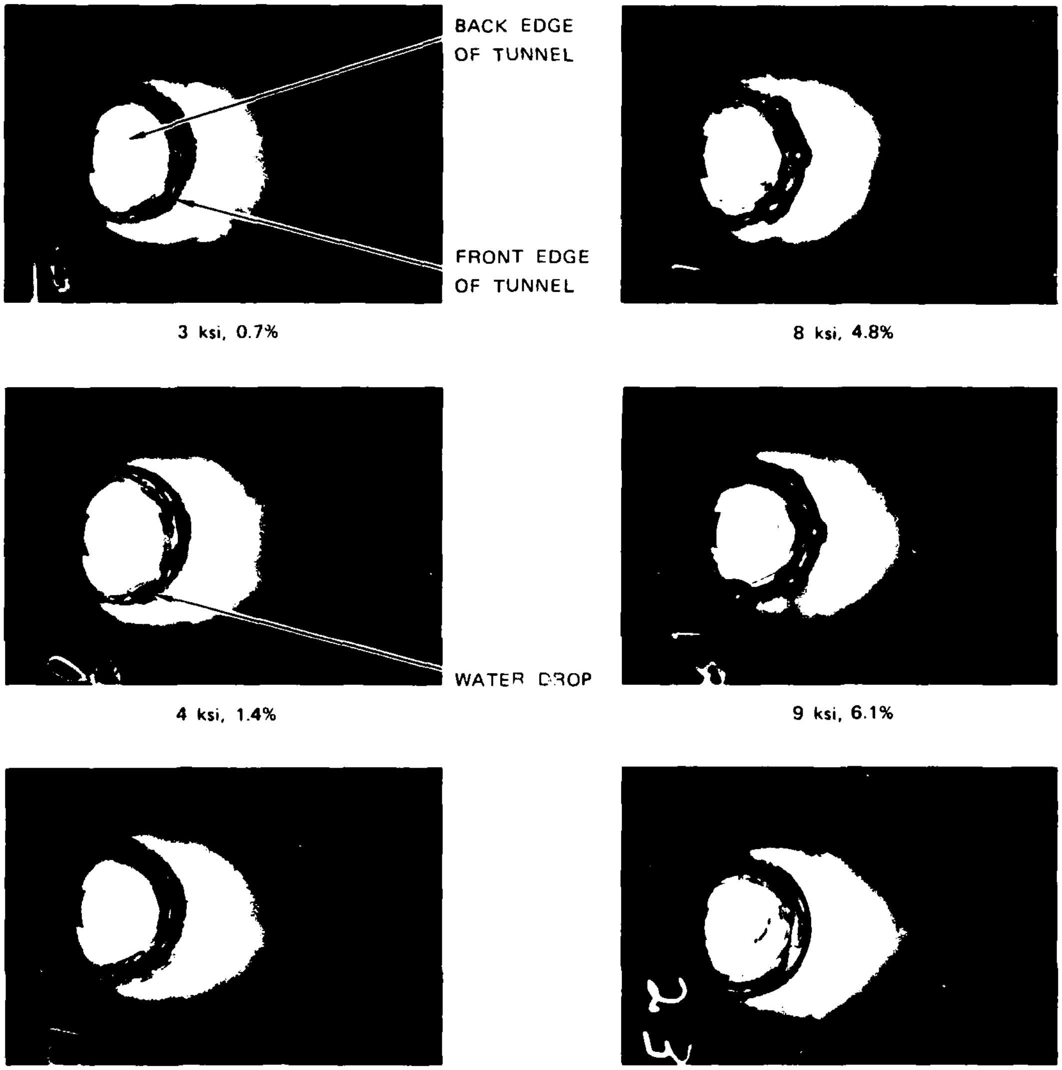

3 ksi, 0.7%

8 ksi, 4.8%

4 ksi, 1.4%

9 ksi, 6.1%

7.5 ksi, 4.2%

11 ksi, 9.8%

MP-4121-46

FIGURE 5.2 DEVELOPMENT OF BUCKLING IN STATIC UNIAXIAL STRAIN LOADING TEST, SUX-95. MONOCOQUE STEEL LINER WITH a/h = 18

Vertical tunnel closure $\Delta D_V/D_V$ is plotted as a function of the applied vertical pressure P_V in Figure 5.3. These results are somewhat surprising in that it appears that the strength of the liner has little effect on load-carrying capacity. For example, in the aluminum liner tests, all liners show approximately the same deformation for a given load; in addition, there is actually less deformation for a given load in the $a/h = 18$ steel liner with a strength $P_i = 2100$ psi (14.5 MPa) than in the $a/h = 4$ aluminum liner with a nominal strength $P = 3300$ psi (22.75 MPa).

A possible explanation for the small influence of tunnel liner strength is that the entire rock specimen yields before P_V reaches 5 ksi (34.5 MPa). Far-field yield is inconsistent with the usual deep-base scenario in which the liner, by applying pressure to the tunnel wall, increases the stress levels in a localized plastic region in the rock surrounding the tunnel. A corollary is that, for a given load, stronger liners give rise to smaller plastic zones. Smaller plastic zones correspond to smaller tunnel closures because of the elastic constraint provided by the material outside the plastic zone. Hence we obtain the expected result: stronger tunnel liners permit less tunnel closure. However, when yielding occurs in the far field, the tunnel liner's effectiveness is reduced drastically. There is no longer a small plastic region around the tunnel in which the stresses are controlled by the liner strength, the constraint of the elastic material outside this plastic region is lost, and tunnel closure is determined by gross plastic flow.

We can see evidence of overall yield of our specimens in the plot in Figure 5.4 of lateral pressure P_H as a function of vertical pressure P_V from our uniaxial strain tests. One straight line is drawn through the data for vertical pressures less than 4 ksi (27 MPa), and a second straight line is drawn through the data for vertical pressures greater than 4 ksi (27 MPa). This bilinear plot is exactly what would be expected for a linear elastic-perfectly plastic frictional material. The slope of the first straight line, during elastic response, is equal to $\nu/(1 - \nu)$, where is Poisson's ratio. For the slope in Figure 5.4, this yields

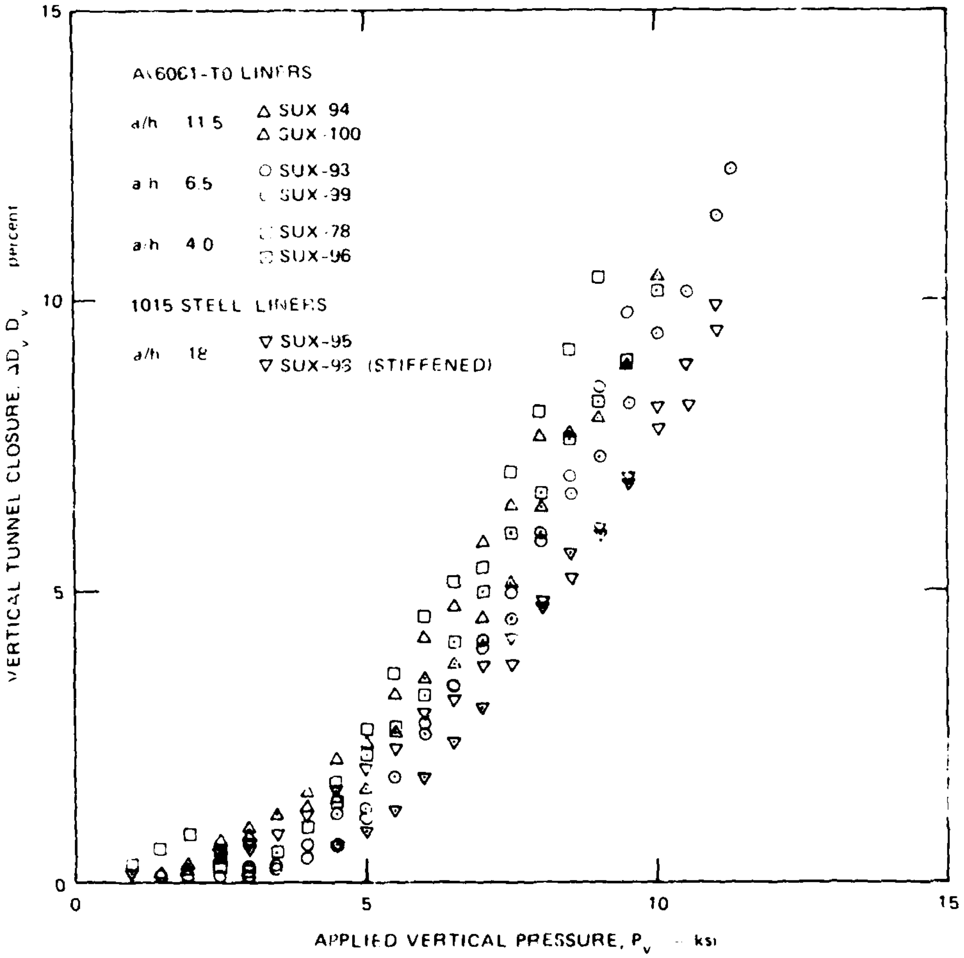

MA-4121-84

FIGURE 5.3 VERTICAL TUNNEL CLOSURE VERSUS APPLIED VERTICAL PRESSURE FOR STATIC UNIAXIAL STRAIN LOADING OF SRI RMG 2C2

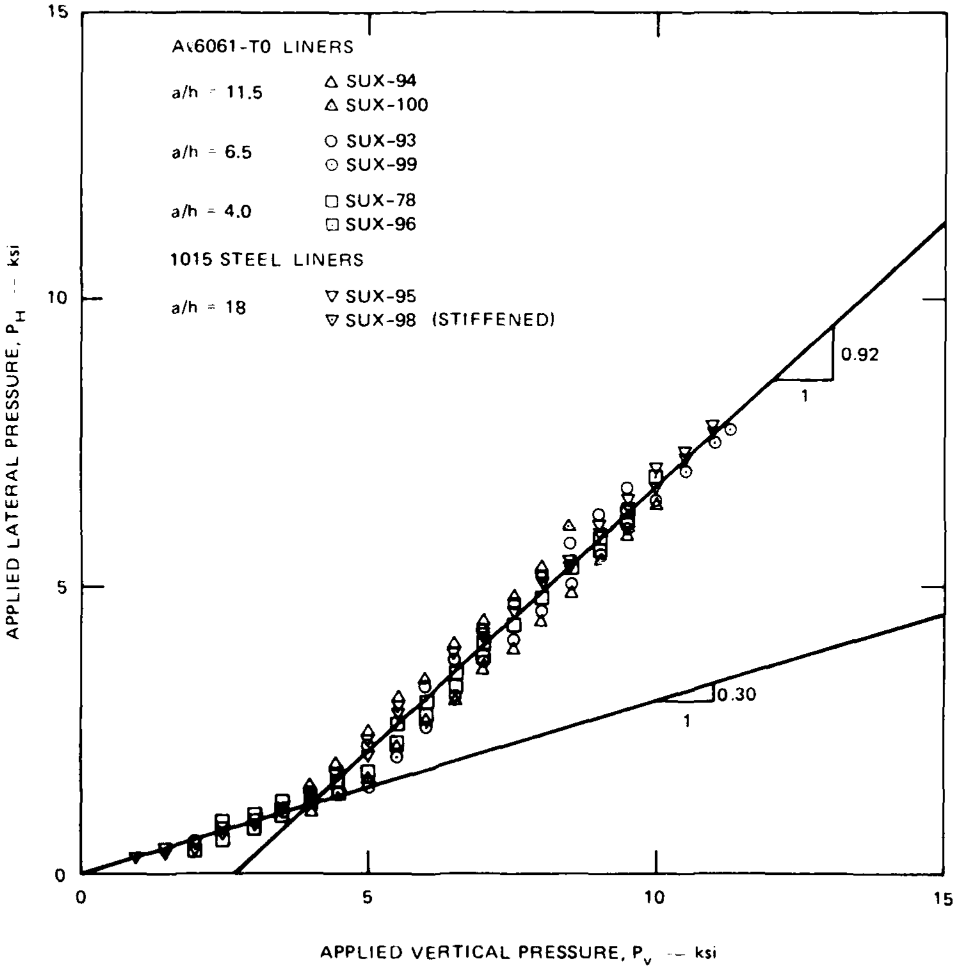

MA-4121-85

FIGURE 5.4 APPLIED LATERAL CONFINING PRESSURE VERSUS APPLIED VERTICAL PRESSURE NEEDED TO MAINTAIN UNIAXIAL STRAIN CONDITIONS IN SRI RMG 2C2 a value of Poisson's ratio for SRI RMG 2C2 of 0.23, somewhat larger than the value of 0.18 given by Terra Tek. The slope of the second line, during plastic response, is equal to $1/N_\phi$, the slope of the triaxial compression failure envelope, where $N_\phi = (1 + \sin\phi)/(1 - \sin\phi)$, and ϕ is the friction angle. For SRI RMG 2C2, $\phi = 2.5°$ (0.044 rad) and $1/N_\phi = 0.92$, precisely the slope of the line through the data. The unconfined compressive strength, σ_u, is given by the point where the second straight line intersects the horizontal axis, the point for which failure occurs with no lateral confining pressure. The value of 2.7 ksi (18.6 MPa) obtained is less than the 3.2 ksi (22.1 MPa) found in unconfined compressive tests. However, the unconfined compressive strength determined in uniaxial strain loading tests is typically 15 percent less than that found in unconfined compressive tests [5].

The results obtained from the uniaxial strain tests shown in Figure 5.4 indicate that modeling SRI RMG 2C2 as a linear elastic-perfectly plastic frictional material is a good representation of its constitutive behavior.

5 2 DYNAMIC TESTS

Dynamic uniaxial strain loading tests were performed on specimens similar to those tested statically, with the same five tunnel liners. As in the dynamic isotropic loading tests, no provision was made for porewater to drain from the specimen.

In our static uniaxial strain tests, the specimen lateral strain was maintained at zero by adjusting the lateral pressure after each increment in vertical pressure. In our dynamic tests, however, we could not control the load path and specimen lateral strain so well. As the load path in the dynamic tests deviated from the uniaxial strain load path, the magnitude of the specimen lateral strain increased. We recorded the output of two strain gages on the specimens that were oriented to measure lateral strain. In all but one of our tests, the lateral pressure was greater than required for uniaxial strain through the test; the specimen was overconfined and the specimen lateral strain was negative. In the other test, DUX-74, the specimen was overconfined initially, but before the vertical pressure reached 75 percent of its peak value, the specimen was underconfined and the specimen lateral strain started to go positive. It is important to discriminate between these two types of tests: overconfined tests give lower bounds on tunnel closure, whereas underconfined tests give upper bounds. We will compare load paths and specimen lateral strains for overconfined and underconfined dynamic tests later in this section. In Chapter 6, we will present results of a static test that was intentionally underconfined to investigate the effect of underconfinement on tunnel closure.

In each of the dynamic uniaxial strain loading tests the tunnel liner ovalled without buckling. Not all liners ovalled to the same extent; some had small outward springline displacements while others had small inward springline displacements, but in every case the deformed liner cross section was ovalled with the major axis at the springlines.

Residual vertical tunnel closure for the dynamic uniaxial strain loading tests is plotted as a function of peak applied vertical pressure in Figure 5.5. As mentioned in the last chapter, results from static tests indicate that the difference between maximum tunnel closure under load and residual tunnel closure is small, if not zero. The tunnel closures for dynamic uniaxial strain loading, like the tunnel closures for dynamic isotropic loading, are very small, typically 1 percent or less for peak vertical pressures between 7 and 10 ksi (48 and 69 MPa). An exception is DUX-74 (the underconfined test), shown as the solid circle in Figure 5.5, where the vertical tunnel closure is more than 3.5 percent for a peak applied vertical pressure of 9.6 ksi (66.2 MPa). At present, only the results of the four overconfined tests will be considered. The tunnel closures reported are therefore lower bounds on the actual dynamic uniaxial strain loading tunnel closure.

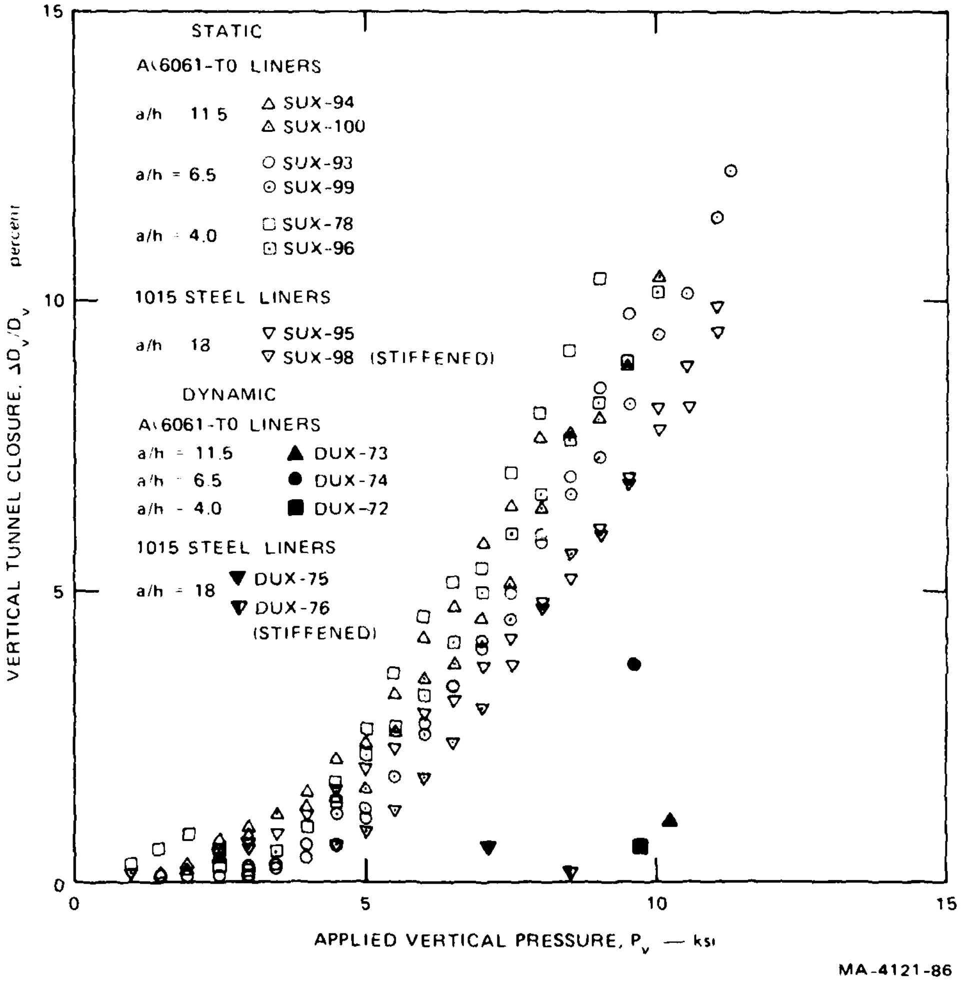

FIGURE 5.5 VERTICAL TUNNEL CLOSURE VERSUS APPLIED VERTICAL PRESSURE FOR STATIC AND DYNAMIC UNIAXIAL STRAIN LOADING OF SRI RMG 2C2

As for the dynamic isotropic loading tests results, the data are too meager to compare the effectiveness of one tunnel liner with another. However, it is clear that tunnel closures obtained under dynamic loading are much smaller than those obtained under static loading. For example, a loading pressure of 10 ksi (69 MPa) produces a vertical tunnel closure of about 1 percent in the dynamic tests and between 7.75 and 10.5 percent in the static tests, so that the vertical tunnel closure in the dynamic tests is less than 15 percent as large as in the static tests at 10 ksi (69 MPa). A vertical tunnel closure of 1 percent would occur when the applied vertical pressure was 3 to 5 ksi (21 to 34 MPa) in a static test, but about 10 ksi (69 MPa) in a dynamic test. Thus, at least for small closures, the structures can withstand a dynamic loading twice as large as the static loading and suffer the same vertical tunnel closure.

For the isotropic loading tests presented in Chapter 3, we stated that this difference in tunnel closure is probably due to strain rate and porewater effects. In addition, the difference between static and dynamic results here is accentuated by comparing overconfined dynamic tests with adequately confined static tests.

We return now to our comparison of underconfined and overconfined dynamic tests. Figure 5.6 shows the difference in lateral confinement between DUX-74 (underconfined) and DUX-75 (representative of the four overconfined tests). The lateral confining pressure in DUX-75 is well above the level necessary to maintain uniaxial strain conditions in the static tests as shown in Figure 5.6(b). Correspondingly, the radial displacement at the lateral surface of the specimen is inward, Figure 5.6(a). The peak recorded by the strain gages on the copper can, -0.07 percent, indicates that the maximum inward radial displacement of the specimen's lateral surface was about 1.5 mils (0.04 mm). This displacement was achieved just as the peaks of the vertical and lateral pressure pulses were reached, after 5.5 ms. For DUX-74, the lateral confining pressure is above the static uniaxial strain level initially, similar to DUX-75, as shown in Figure 5.6(d). At 4.25 ms, however, the lateral confining pressure

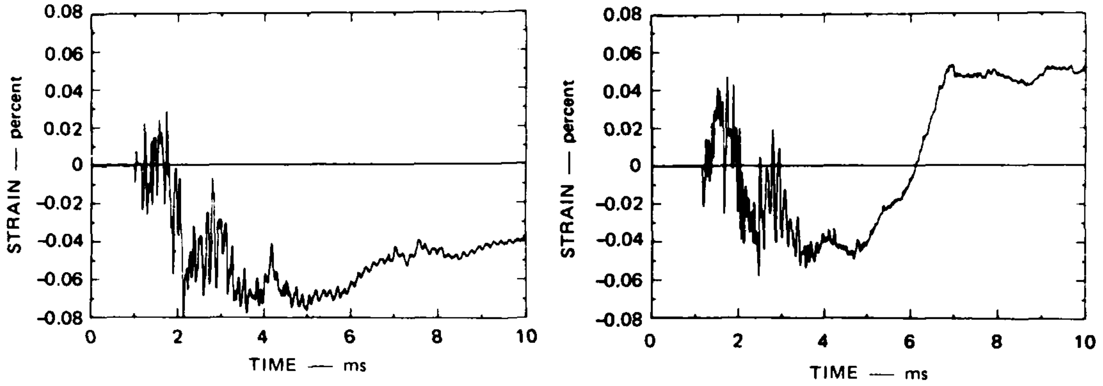

(a) SPECIMEN LATERAL STRAIN FROM DUX-75 (c) SPECIMEN LATERAL STRAIN FROM DUX-74

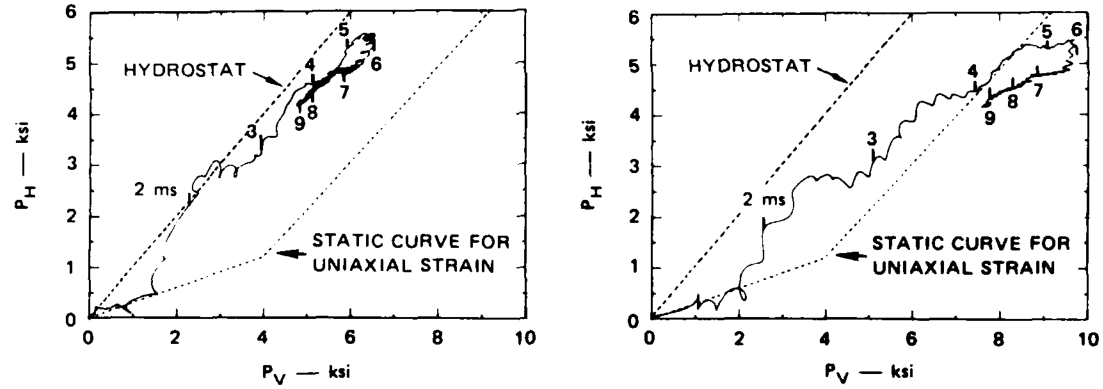

(b) LOAD PATH FROM DUX-75 (d) LOAD PATH FROM DUX-74

MA-4121-154

FIGURE 5.6 COMPARISON OF SPECIMEN LATERAL STRAIN AND LOAD PATH FROM AN OVERCONFINED TEST (DUX-75) AND AN UNDERCONFINED TEST (DUX-74) crosses from above to below the static level and remains there for the remainder of the test. That this has occurred, however, is not manifest in the radial displacement of the specimen's lateral surface until just after 6 ms, nearly 2 ms later, as shown in Figure 5.6(c). This is precisely when the peaks of the vertical and lateral pressure pulses occur. However, as the loading pressures decay, the radial displacement increases to 1 mil (0.025 mm). Without active measurement of tunnel closure, we cannot assess individually the roles of initial overconfinement at low pressure, adequate confinement at peak pressure, and post-peak underconfinement in producing the large tunnel closure measured in DUX-74. We will, however, address this again in the next chapter where we present the results of an underconfined static test.

5.3 COMPARISON OF RESULTS FROM ISOTROPIC LOADING TEST AND UNIAXIAL STRAIN LOADING TESTS

Tunnel closure data for static isotropic and uniaxial strain loading are compared in Figure 5.7. The data points are for isotropic loading. The shaded region includes all the uniaxial strain loading tunnel closure data. For the most part, the isotropic closure data are below the uniaxial strain closure data, indicating that the tunnel and its reinforcing liner are stronger under isotropic loading. This difference in strength is especially evident for data from the two isotropic loading tests in which porewater drained from both ends of the tunnel, SI-97 and SI-101. The reason for the difference in strength is that, for isotropic loading, the liner resists deformation through hoop compression, which is the most efficient means of resistance for a thin-walled shell. The liner carries a significant part of the total load, i.e., the surrounding rock does not carry all the load alone. For uniaxial strain loading, however, the liner resists deformation through a combination of hoop compression and bending, which is a less efficient means of resistance. In this case, the liner carries a smaller part of the load, with the rock carrying the major part, and the reinforced rock cavity is weaker. Another reason

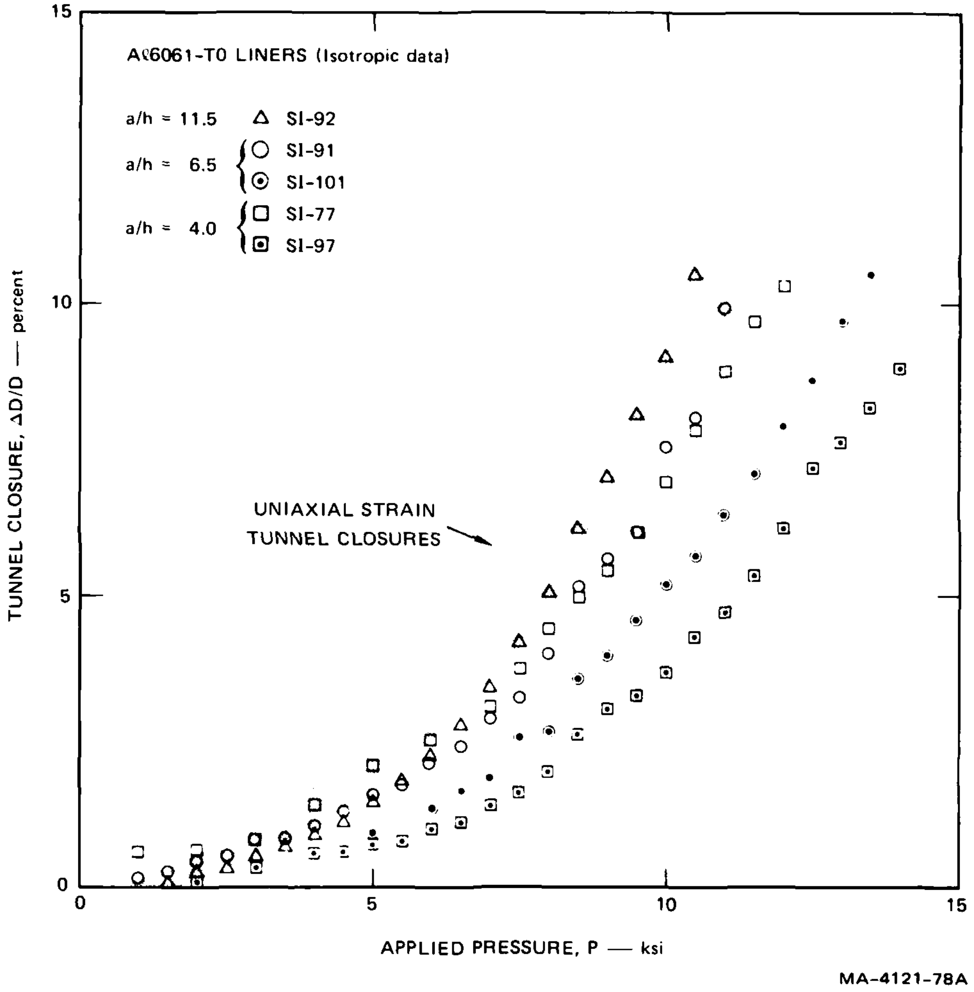

FIGURE 5.7 COMPARISON OF TUNNEL CLOSURES IN SRI RMG 2C2 FOR STATIC ISOTROPIC AND UNIAXIAL STRAIN LOADING

isotropic closures are less than uniaxial strain loading is that the specimen remained elastic in the far field in the isotropic loading tests, whereas the entire specimen yielded at less pressure in the uniaxial strain loading tests.

The tunnel closures resulting from dynamic isotropic and overconfined dynamic uniaxial strain loading tests are about equal; both are much smaller than tunnel closures measured in the static tests for the same applied pressures. More data are needed to determine any trends.

5.4 CONCLUSIONS

The most important conclusion to be drawn from the results of the uniaxial strain loading experiments is that the tunnel closures measured in the dynamic tests are much smaller than those measured in the static tests. This corroborates the similar result found in the isotropic loading experiments. The difference in tunnel closures is attributed to the greater strain rate and porewater pressure in the dynamic tests. Comparing overconfined dynamic tests with static tests contributes to the difference reported.

Unlike the isotropic loading results, tunnel liner strength had little effect on the tunnel closures measured in the static uniaxial strain loading tests because the entire specimen yielded at very low pressure, significantly reducing the influence of the tunnel liner. Thus, in field tests, when the loading stress wave amplitude approaches and exceeds the free-field yield level, we predict that tunnel damage will be severe even for strong liners. This prediction is consistent with the heavy and nearly uniform damage over a range of structure strengths at the high stress drift in Mighty Epic.

6. SPECIAL TESTS

Four static tests were performed on 4-inch- (0.1-m) diameter specimens of SRI RMG 2C2 under conditions that were somewhat different from the monotonic isotropic and uniaxial strain loading experiments presented in the previous two chapters. The tunnels in these four specimens were reinforced with the strongest of the three 6061-T0 aluminum liners, the one having a/h = 4.0.

In the first two of these tests, we subjected specimens to cyclic loading that was either entirely isotropic or entirely uniaxial strain. This simulates a deep-based structure being subjected to multiple end-on or side-on loading. The results of these tests are similar to cyclic loading tests performed on 6B rock simulant [2]. In the third test, we subjected the specimen to uniaxial strain loading followed by isotropic loading. This simulates a deep-based structure being first attacked side-on and then end-on. Finally, we performed an underconfined static uniaxial strain loading test to investigate the effect of underconfinement on tunnel closure. The results of this test have implications for the data obtained from dynamic uniaxial strain loading tests in the laboratory and for the side-on loading of a deep-based structure.

6.1 CYCLIC LOADING TESTS

6.1.1 Cyclic Isotropic Loading Test

In this test, SI-80, the specimen was loaded to 5.5 ksi (38 MPa) and then unloaded to 1 ksi (7 MPa). (We did not unload to zero pressure because we would lose the seals in our testing machine.) The specimen was then loaded to 5.5 ksi (38 MPa), 7 ksi (48 MPa), and 8 ksi (55 MPa) with unloadings again to 1 ksi (7 MPa) between. Figure 6.1 shows the resulting tunnel closure as a function of the applied pressure. The cyclic loading does not reduce the load-carrying capacity of the specimen; greater tunnel

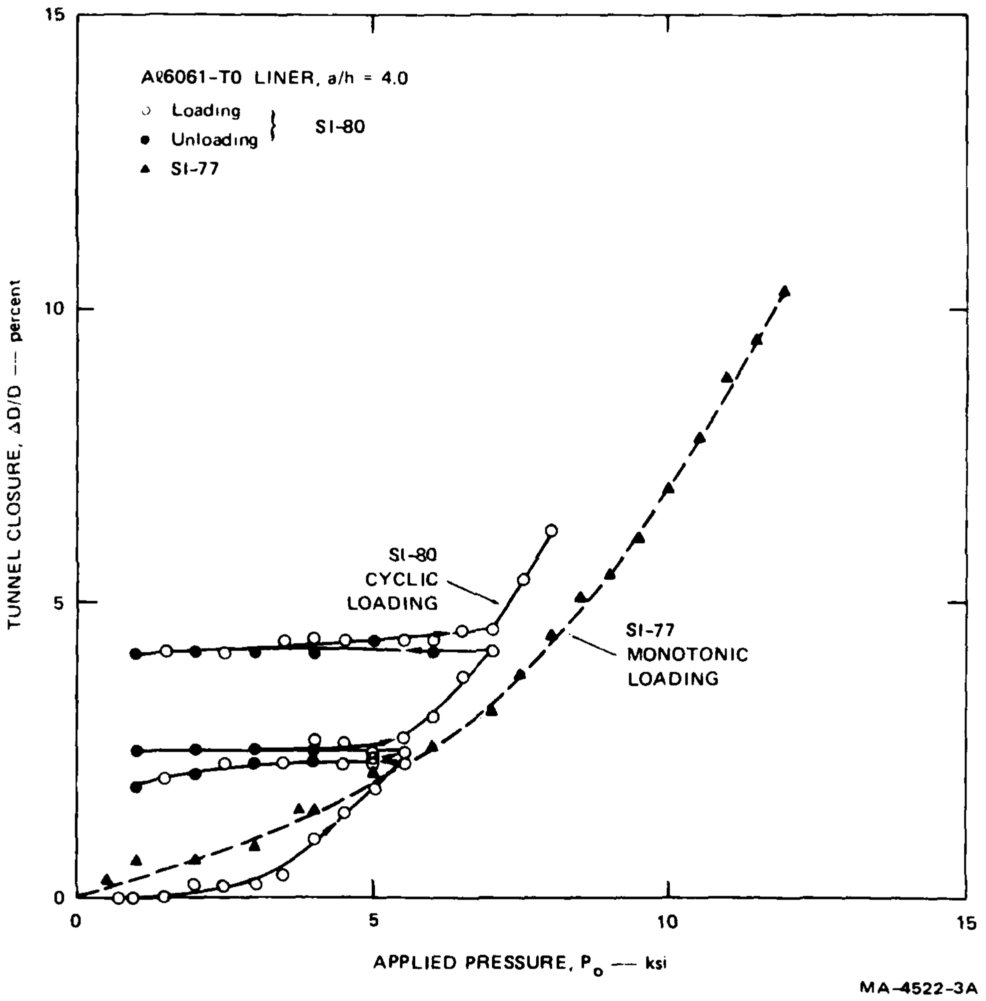

FIGURE 6.1 TUNNEL CLOSURE VERSUS APPLIED PRESSURE FOR SRI RMG 2C2 SUBJECTED TO CYCLIC AND MONOTONIC ISOTROPIC LOADING

closure requires higher pressure just as for monotonic loading. Further, unloading and reloading occur along the same path.

The results of the cyclic loading test are compared with the results of a monotonic loading test, SI-77, also plotted in Figure 6.1. The closures obtained under cyclic loading are somewhat larger than those obtained under monotonic loading, but the divergence between the two closure-versus-pressure curves is not serious and may be due to a variation in the strength of the two specimens. From the results of this test, we conclude that a structure in SRI RMG 2C2 subjected to cyclic isotropic loading "shakes down." Therefore, it is reasonable to conclude that a deep-based structure can survive multiple end-on loadings.

6.1.2 Cyclic Uniaxial Strain Loading Test

In this test, SUX-79, the specimen was loaded to 4.5 ksi (31 MPa) and then unloaded to about 1 ksi (7 MPa). As in the cyclic isotropic loading test, this load-unload cycle was repeated three more times. The vertical and lateral pressures in both the loading and unloading portions of the cycle were controlled such that zero strain was maintained in circumferential strain gages on the rock specimen can, i.e., to produce uniaxial strain in the specimen. Figure 6.2 shows the resulting vertical tunnel closure as a function of the applied vertical pressure. The data are very similar to those obtained in the cyclic isotropic loading test. The cyclic loading does not reduce the load-carrying capacity of the specimen, and unloading and reloading occur along the same path.

The results of a monotonic uniaxial strain loading test, SUX-78, also plotted in Figure 6.2 for comparison with the cyclic strain loading test. The closures obtained under cyclic loading are slightly larger than those obtained under monotonic loading, but this difference is small. We conclude that a structure in SRI RMG 2C2 subjected to cyclic uniaxial strain loading "shakes down." It is therefore reasonable to expect that a deep-based structure can survive repeated side-on loading.

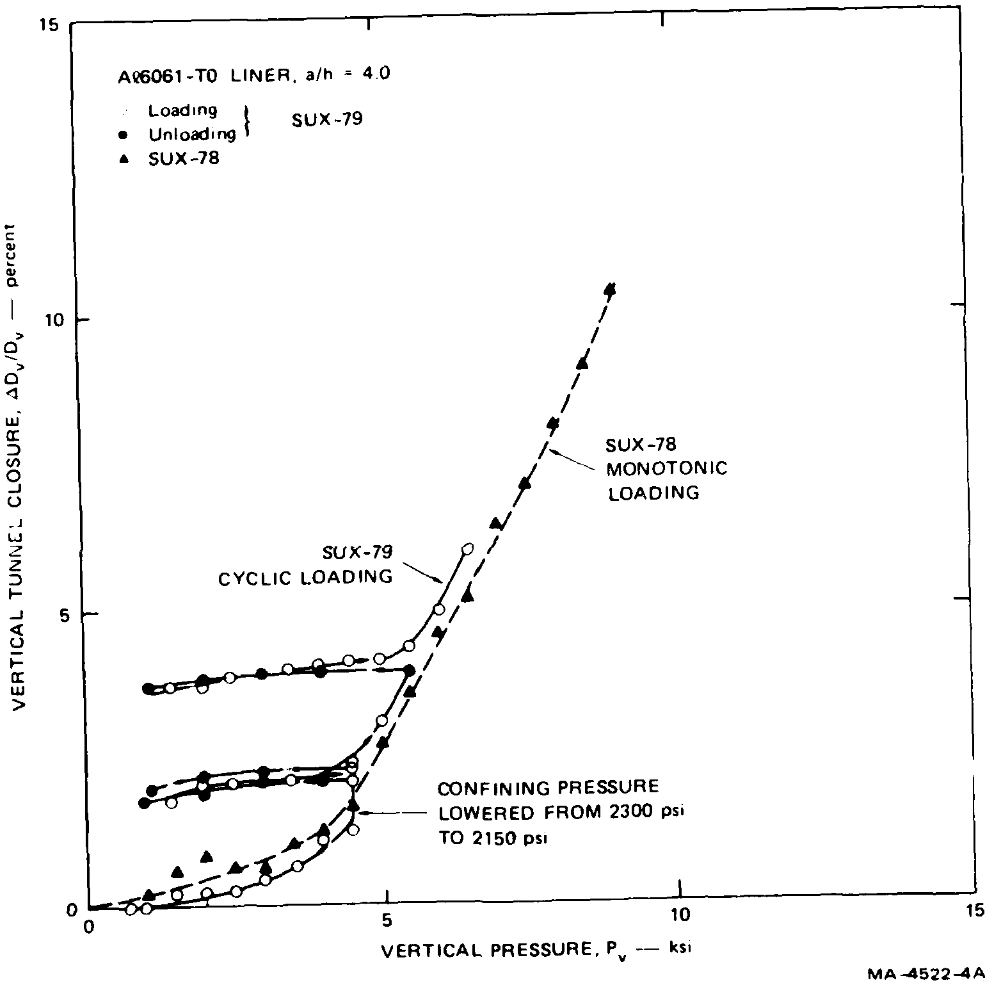

FIGURE 6.2 VERTICAL TUNNEL CLOSURE VERSUS APPLIED PRESSURE FOR SRI RMG 2C2 SUBJECTED TO CYCLIC AND MONOTONIC UNIAXIAL STRAIN LOADING

6.2 UNIAXIAL STRAIN/ISOTROPIC LOADING TEST

We performed this test, SUX/SI-102, to determine the influence of deformation during initial uniaxial strain loading on deformation during subsequent isotropic loading. This loading simulates the uniaxial strain loading followed by the axisymmetric, end-on loading of several structures fielded in both Mighty Epic and Diablo Hawk.

The specimen was first loaded under uniaxial strain conditions to 7.5 ksi (52 MPa). The pressure was then reduced to zero while maintaining uniaxial strain, and the specimen was reloaded isotropically to 14 ksi (97 MPa). At this point the vertical tunnel closure exceeded 10 percent. Figure 6.3 shows the vertical tunnel closure as a function of the applied vertical pressure. During the second portion of the test, when the loading was isotropic, the vertical and lateral confining pressures were, of course, the same. However, due to the asymmetric tunnel deformation during the prior uniaxial strain loading, the vertical and lateral tunnel closures were not the same.

During the uniaxial strain loading portion of the test, the tunnel ovalled. At 7.5 ksi (52 MPa) the vertical tunnel closure was 5.5 percent and the diameter of the tunnel at the springlines increased 1.5 percent. When the load on the specimen was reduced to zero, the vertical tunnel closure dropped to 5 percent, but the springline diameter did not change. Therefore, when the isotropic loading was applied, the tunnel was not circular, but ovalled, with the springline diameter being about 7 percent larger than the vertical diameter. Initially, the effect of the isotropic loading was to increase the vertical diameter and to reduce the springline diameter, i.e., to make the tunnel more circular. At about 5 ksi (39 MPa) the vertical diameter started to decrease again, and by 8.5 ksi (59 MPa) the vertical tunnel closure was as large as it was at the peak of the uniaxial strain loading portion of the test. This indicates that further tunnel closure does not occur until the isotropic loading pressure exceeds the maximum vertical pressure applied during the uniaxial strain portion of the test.

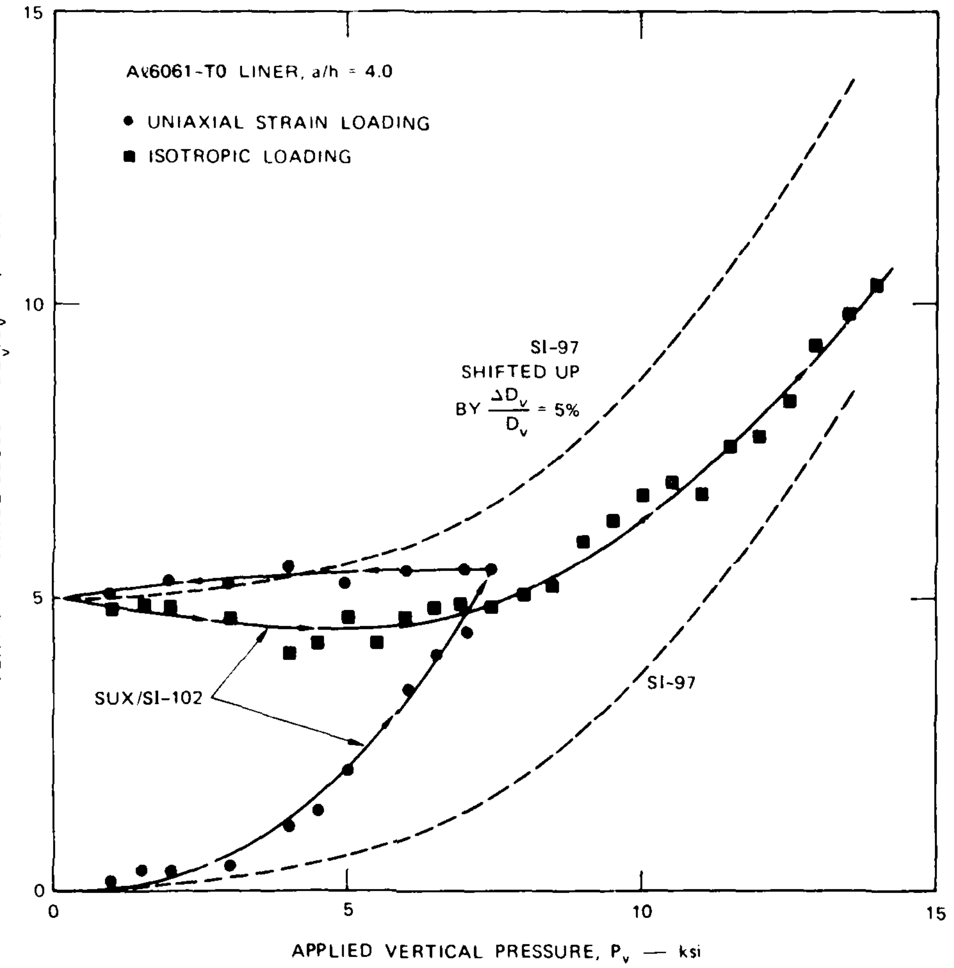

FIGURE 6.3 VERTICAL CLOSURE VERSUS APPLIED VERTICAL PRESSURE FOR STATIC UNIAXIAL STRAIN LOADING FOLLOWED BY STATIC ISOTROPIC LOADING OF SRI RMG 2C2

For comparison, Figure 6.3 plots a curve that was fit through the data from SI-97, a test in which the specimen was subjected to monotonic isotropic loading. At large closures, the tunnel closure data obtained during the isotropic loading portion of SUX/SI-102 approach those obtained during SI-97. This indicates that the ovalling of the tunnel during the initial uniaxial strain loading does not substantially reduce the specimen's capability to carry subsequent isotropic loads. The SI-97 curve is replotted in Figure 6.3, but shifted up by $\Delta D_V/D_V$ = 5 percent so that it begins at the same point as the reloading curve. The tunnel closure data from the isotropic portion of SUX/SI-102 lies well below the shifted SI-97 curve. This is further evidence that the liner-rock structure has "shaken down."

Results of this test indicate that no further vertical tunnel closure should be observed in structures fielded in Mighty Epic and Diablo Hawk unless the loading pressure on the structure in Diablo Hawk exceeds the loading pressure in Mighty Epic.

6.3 UNDERCONFINED UNIAXIAL STRAIN LOADING TEST

Test SUX-90 was performed to investigate the difference in tunnel closure reported by SRI and WES for the uniaxial strain loading of an SRI RMG 2C2 specimen whose tunnel was lined with an Al6061-TO monocoque cylinder having a/h = 4.0. The discrepancy in test results is shown in Figure 6.4. The difference in the tunnel closure data is greater than can be accounted for by experimental error. For example, the vertical pressure required to achieve a tunnel closure of 5 percent is 22 percent less in the WES test than in the SRI test. In terms of deformation at the same load, for an applied vertical pressure of 5 ksi (34 MPa), the vertical tunnel closure in the WES test is twice as great as in the SRI test.

Three possible causes for the discrepancy between the WES and the SRI results are:

(1) The difference in scale. Larger models generally respond at lower loads.

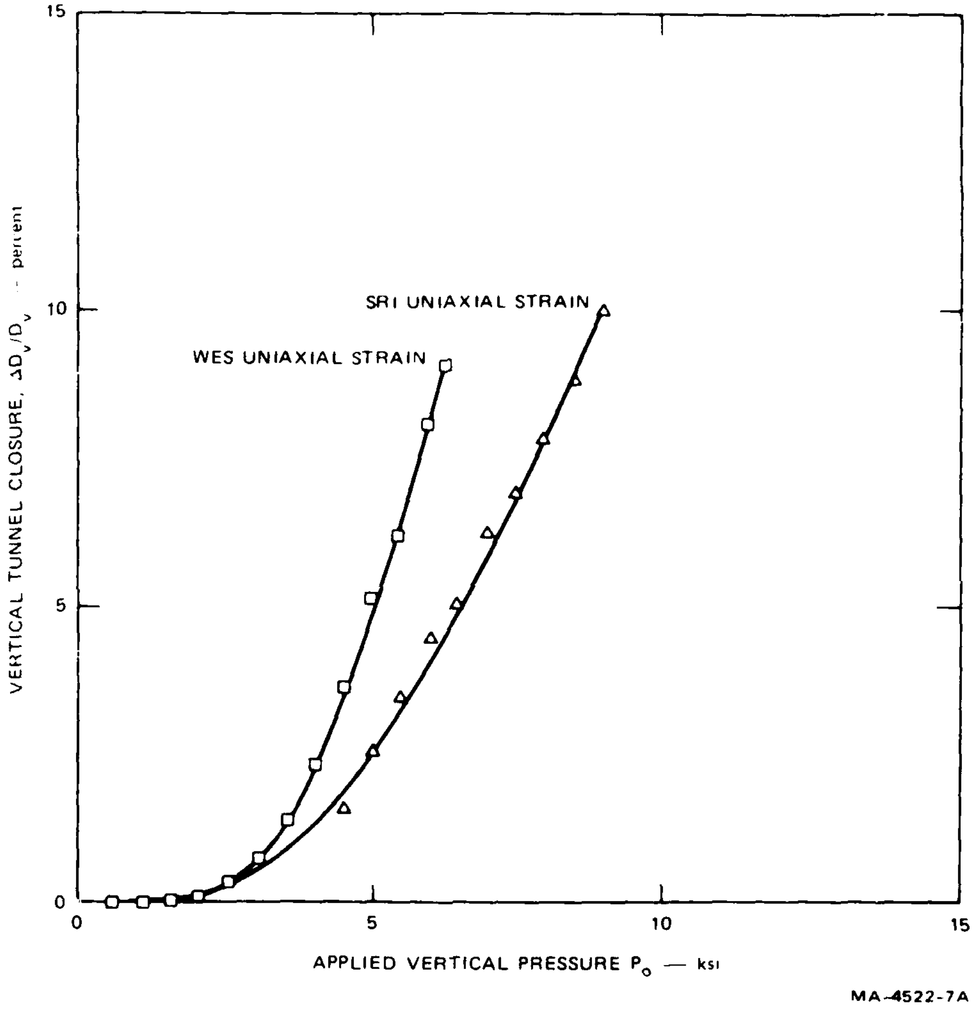

FIGURE 6.4 VERTICAL TUNNEL CLOSURE VERSUS APPLIED VERTICAL PRESSURE — COMPARISON OF DATA OBTAINED BY SRI AND WES FOR STATIC UNIAXIAL-STRAIN LOADING OF SRI RMG 2C2, Aℓ6061-T0 LINER, a/h = 4.0.

(2) Differences in simulated rock properties. Curing could be different at large and small sizes. Also, in the WES rock model the tunnel was cast in place while in the SRI model the tunnel was bored into a solid rock model.

(3) Difference in loading method. At SRI, lateral loading was applied with a hydraulic pressure P_H, which was increased with increasing vertical pressure P_V to maintain zero hoop strain at the rock specimen surface. At WES, lateral loading was applied by mechanical confinement with 7-inch- (178-mm) thick steel rings. It is this last difference that was investigated by performing SUX-90.

The load path for the special test performed at SRI is shown in Figure 6.5. During the initial loading, the lateral pressure P_H was increased with P_V to maintain zero lateral strain, just as in the usual SRI uniaxial-strain experiment. This was done so that a small but finite pressure P_H 0.5 ksi (3.4 MPa), would press the copper can (on which the strain gages are mounted) against the rock, ensuring that the can follows the surface strain of the rock during the finite strains to follow.

As the vertical pressure P_V was increased further, the lateral pressure was held fixed at 0.5 ksi (3.4 MPa). The lateral strain ϵ was then free to increase as shown by the dotted curve. It was originally planned to allow the strain to increase to 0.1 percent and then hold it at that value. However, during the load increment from P_V = 4.5 to 5 ksi (31 to 34 MPa), the strain increased from 0.075 to 0.168 percent. To reduce the strain, we increased the lateral pressure to P_H = 1.8 ksi (12.4 MPa) while P_V was held fixed at 5 ksi (34 MPa). The resulting loading point falls on the uniaxial-strain loading path from previous SRI tests, as shown in Figure 6.5. However, because the present loading path for arriving at this point is different, the lateral strain, while reduced from 0.168 percent, remains finite at 0.12 percent.

During the further increase in P_V from 5 to 6.5 ksi (34 to 45 MPa), the lateral pressure P_H was adjusted to maintain ϵ fixed, as it would if the rock were to come against the rigid 7-inch- (178-mm) thick rings.

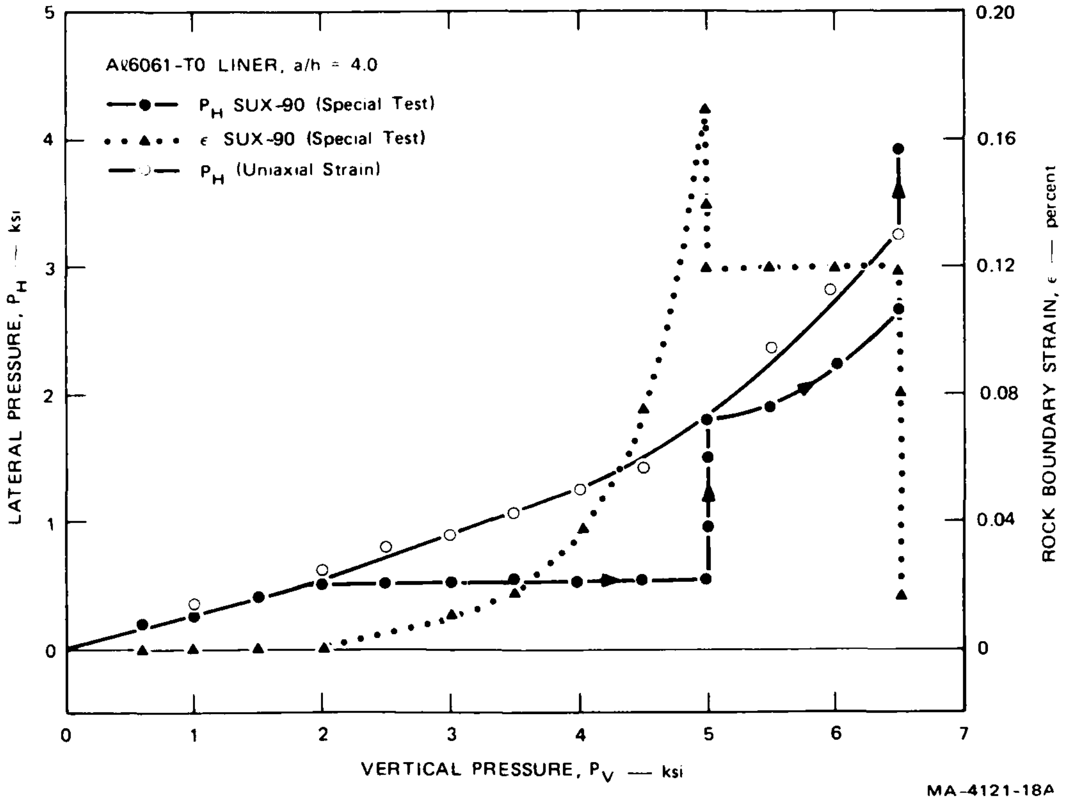

FIGURE 6.5 LOAD PATHS FOR UNIAXIAL STRAIN TEST AND FOR SPECIAL TEST, SUX-90, IN WHICH ROCK BOUNDARY STRAIN ε IS ALLOWED TO INCREASE (AS SHOWN) WITH P_H HELD AT 0.5 ksi

Then, just for curiosity, we increased the lateral pressure to P_H to drive ε back to a value near zero strain. The resulting load point lies above the uniaxial-strain loading path, as expected.

The target value of 0.1 percent for lateral strain was selected on on the basis of the outward springline motion of about 3 percent observed in the WES test as compared with less than 1 percent in the uniaxial strain test at SRI. Calculating roughly, a lateral strain ε (closure) at the rock outer boundary (radius R_r) is reflected in a rock closure $\Delta D/D$ at the tunnel boundary (radius R_t) of $\Delta D/D = (R_r/R_t)^2\varepsilon$. This formula is strictly true only for symmetric, incompressible flow of the rock, but it should give the correct order of magnitude for our purpose. For the WES machine, R_r/R_t = 30 inches/4.5 inches = 6.6 (762 mm/119 mm), and for the SRI machine, R_r/R_t = 4 inches/0.63 inch = 6.4 (101 mm/16 mm). Thus, for ε = 0.1%, $\Delta D/D = (6.5)^2(0.1)$ = 4.2%, which is near the springline motion in the WES test.

Also, a lateral rock boundary strain of 0.1% translates into a gap between rock and confining rings of 0.001 x 15 inches = 0.015 inch (0.38 mm). It is not unreasonable for the inevitable layers of polyethylene, grout, entrapped air, etc., between rock and confining rings to have a resultant compliance equivalent to a 15-mil- (0.38-mm) gap, compared with a 30-inch- (762-mm) diameter rock.

The tunnel closures that result from the loading paths in Figure 6.5 are given in Figure 6.6. The dashed curve is from the SRI uniaxial-strain tests. The load that produces 5% vertical closure is 6.4 ksi (44 MPa). The maximum springline outward movement is 0.8%. The solid curve is from the corresponding WES test. The load that produces 5% vertical closure is 5.1 ksi (35 MPa), and the springline outward motion is 2.7%, and increasing. The points are data from the special test with P_H held at 0.5 ksi (3.4 MPa) while P_V was increased to 5 ksi (34 MPa). These points follow the WES test reasonably closely. Until P_V = 4.5 ksi (31 MPa), points for both the crown-invert and spherical test with P_H held at inside the curves from the WES test (smaller motions). Then, as ε

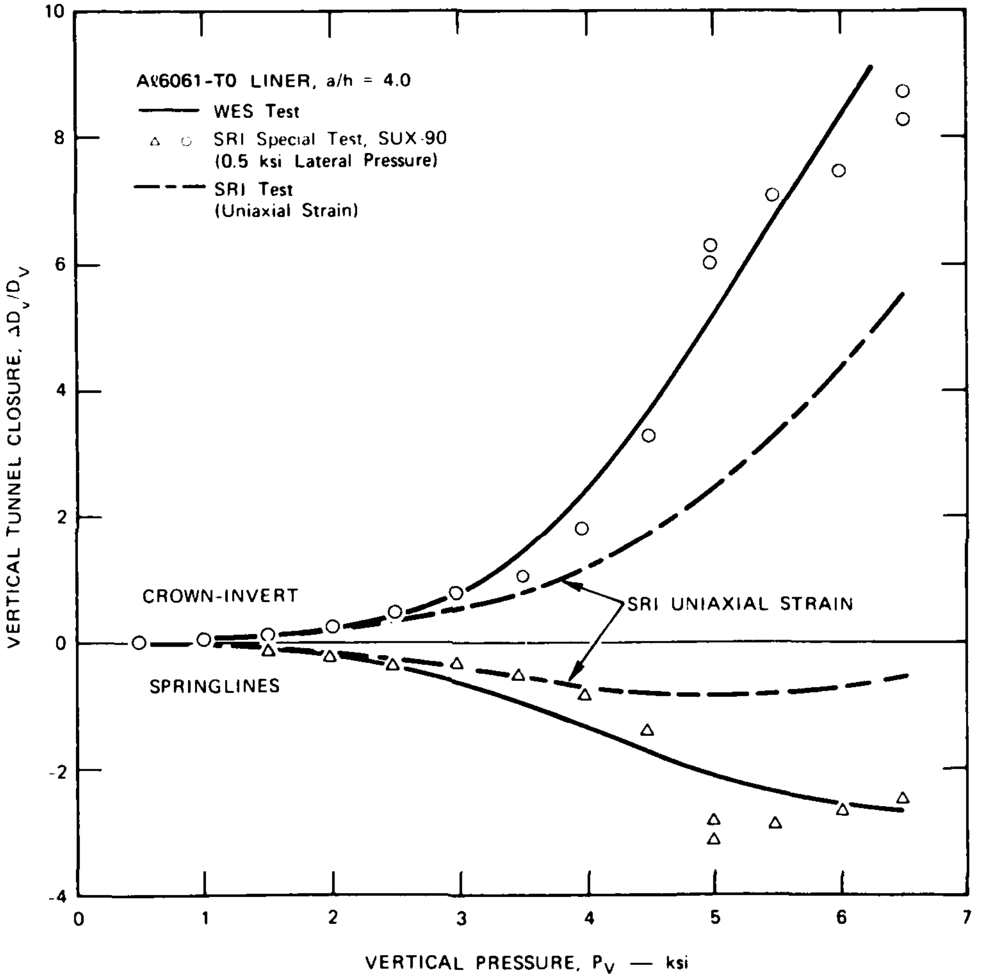

MA-4121-19A

FIGURE 6.6 COMPARISON OF TUNNEL CLOSURES IN WES TEST AND SPECIAL SRI TEST, SUX-90, IN WHICH LATERAL BOUNDARIES OF ROCK ARE ALLOWED TO MOVE OUT 0.1% (REACHED AT P_V = 4.7 ksi) increases rapidly between P_V = 4.5 and 5 ksi (31 and 34 MPa) (see Figure 6.5), the special test tunnel motions also increase rapidly, so that at P_V = 5 ksi (34 MPa), both the crown-invert and springline data points lie outside the WES curves. Tunnel motions in the special test would have been larger for $P_V < 4.5$ ksi (31 MPa) if P_H had been zero rather than the 0.5 ksi (3.4 MPa) conservatively applied to ensure that the copper can was pressed firmly on the rock.

We conclude that a radial expansion of only 15 mils (0.38 mm) on the 30-inch- (762-mm) diameter of the rock in the WES test would be enough to explain the differences between the SRI and WES tests, so this is a possible cause for the discrepancy worth exploring.

The results of SUX-90, namely, that vertical tunnel closure in underconfined tests can be significantly greater than in true uniaxial strain tests,have implications for both laboratory and field tests on deep-based structures. For dynamic uniaxial strain loading tests in the laboratory, the results of SUX-90 indicate that vertical tunnel closures measured in tests for which the lateral confining pressure is too low are upper bounds to the vertical closure that would be measured under truly uniaxial strain loading. Further, if the specimen is so underconfined that the lateral strain reaches 0.1 percent, the upper bound obtained may be 20 to 30 percent larger than the tunnel closure under true uniaxial strain loading. Since the tunnel closure can be significantly greater in tests in which the specimen is underconfined, it is necessary to discriminate between results obtained from tests in which the specimen is confined sufficiently, or perhaps is overconfined, and results obtained from tests in which the specimen is underconfined.

For field tests on deep-based structures, the results of SUX-90 indicate that closures much larger than expected could be obtained if the free-field flow differed from uniaxial strain near the buried structure. The cause for a local variation from uniaxial strain flow could be something as simple as an inhomogeneity in the geological medium at the field site.

7. COMPLEX STRUCTURE MODELS FOR TESTS BY WATERWAYS EXPERIMENT STATION

7.1 COOPERATIVE SRI/WES LABORATORY TESTING PROGRAM

At the request of DNA, a meeting was held at SRI on January 12, 1975, to discuss the application of WES and SRI testing machines to the investigation of deep-based structure response. In particular, a cooperative program of testing was desired to aid in the design and interpretation of structures being tested in the Mighty Epic event. After Mr. James Drake of WES described the WES testing machine capabilities and Dr. Tim Kennedy of SRI described SRI's, it was concluded that parameter studies on small models could be done by SRI, and more extensively modeled and instrumented tests at larger scale could be done by WES. The WES 6000-psi (41-MPa), 47-inch-diameter (1.2-m) testing machine could be modified to apply up to 1 kbar (100 MPa) pressure on 30-inch-diameter (0.76-m) rock specimens by inserting a set of 30-inch-inside-diameter (0.76-m) rings into the machine and adding area-reducing pistons at top and bottom. This would allow tests to be performed with 4.5-inch-diameter (114-mm) rock openings, a factor of 7 larger than the 5/8-inch-diameter (16-mm) openings in the SRI tests.

Work was begun shortly thereafter to modify the WES machine, and SRI began the tests with tuff-matching grout described in the preceding chapters. To ensure uniformity in initial testing, WES prepared grout specimens of SRI RMG 2C2 for both WES and SRI, while SRI made corresponding tunnel reinforcement structures. This section describes the model structures made by SRI for WES. For completeness, we also summarize the WES test procedures and compare them with those used at SRI. Results are also given of tests performed to make a direct comparison between tests at WES and SRI.

Table 7.1 gives the test procedures. It is apparent that, because of the order of magnitude difference in rock specimen size, there are many differences in the details of preparing and testing the rocks. Nevertheless, we will see that the differences in test results, while not insignificant, are within acceptable engineering accuracy so that a useful interchange of results is possible.

7.2 COMPARISON TESTS ON SIMPLE ALUMINUM MODELS

The first test in the WES machine was with a tunnel structure consisting of a simple tube of 6061-T0 aluminum, 28 inches (0.71 m) long, 3.5 inches (89 mm) in inside diameter, and with a 0.5 inch-thick (12.7-mm) wall. In the corresponding SRI test, the tube was 3.7 inches (94 mm) long, 0.49 inches (12.3 mm) in inside diameter, with a 0.069-inch (1.8-mm) thick wall.

Tunnel closure curves for these tests are given in Figure 6.4. The curves are identical in form but differ in that the vertical pressures that cause given vertical closures are about 22% lower in the WES test than in the SRI test. For example, at 5% closure, $P_V = 6.4$ ksi (44 MPa) in the SRI test, while in the WES test $P_V = 5.1$ ksi (35 MPa). This difference is attributed to an accumulation of effects caused by the differences in test specimens and procedures as listed in Table 7.1. Also, note that wherever the direction of an effect is known (procedures 2, 3, 4, and 9), it tends to cause larger deformations in the WES tests. Examination of the effect of procedure 9 was the subject of the final section in the preceding chapter.

A single comparison at SRI between a test with a 1-foot-diameter (0.3-m) RMG 2C2 rock and a 4-inch-diameter (0.1-m) rock showed loading pressures to be 25% smaller in larger rock [9] . Since the only differences in test procedures in these tests were in rock size and test time relative to size, this suggests that size and rate effects (for example, as they affect porewater diffusion) may be the dominant differences between the WES and SRI tests. However, the special tests reported in Figure 6.6 show that small changes in lateral boundary deformations can also have a large effect.

Table 7.1

COMPARISON OF SRI AND WES TEST PROCEDURES[*]

Procedure	SRI	WES
1. Source of ingredient materials for 2C2 simulant	WES stores at NTS[†]	Local Vicksburg supply
2. Rock specimen size[‡]	4-inch dia. x 4-inch tall	30-inch dia. x ?
3. Specimen fabrication[‡]	Cast in 15-inch length, cut and grind into three 4-inch specimens	Cast in machine in polyethylene bag
4. Tunnel fabrication[‡]	Drill, then counterbore at ends for end fittings	Liner cast in place
5. Liner installation	Insert liner, fill back about 30 mils on radius with pourstone	
6. Method of rock saturation	Keep rock submerged in water between all stages of preparation and assembly. Time to insert into sealed unit for test is about 3 min	?
7. Method of porewater drainage	Allow leakage into tunnel at ends and at weep holes near each end	?
8. Vertical Load	Oil pressure across thin diaphragm	Ram and 10-inch thick steel platten
9. Lateral load[‡]	Oil pressure to maintain zero sum of strains from two circumferential gages on copper can. Can is set into intimate contact with rock by initial 500 psi seating pressure. Individual strains are about 50 m strain at 5% closure	Reaction force through watertight polyethylene bag to steel confining rings
10. Transition between rock lateral pressure and tunnel ambient pressure	O-ring seals in end fittings	?
11. Test time	1 to 1½ hours	?

---

[*] Standard laboratory procedures, such as methods for measuring pressures and displacements, are not listed.

[†] For special comparison tests with WES, specimens were cored by WES from block made of same raw materials as for WES models.

[‡] These procedures have a known direction of influence, tending to cause more deformation (lower critical pressures) in the WES tests than in SRI tests.

7.3 COMPLEX STRUCTURE MODELS

7.3.1 Voussoir Block Structure

The first more complex structure made for the WES machine was the voussoir block structure shown in Figures 7.1 and 7.2. The model was made of the same aluminum 6061-T0 used in the tests just described, but was segmented into eight blocks that were free to rotate relative to one another. The rotation joints were made by simply machining each segment with male and female circular ends, as shown in Figure 7.3 and placing a layer of plastic mending tape in the joint to act as a lubricant.

In full-scale, the purpose of the Vussoir block construction is to allow relative rotation of the blocks and thereby reduce the bending moment. This is important for concrete materials that cannot carry large tensile stresses. By rotating, the blocks can conform to asymmetric tunnel deformation while applying the desired structure-rock interface pressure, with the segments acting almost entirely in compression.

The objective of the model test was to demonstrate that the structure would act in this way without the blocks rotating away from the rock cavity and falling into the tunnel. Results summarized in the next subsection show that the voussoir blocks behaved just as desired. so that the overall response was indistinguishable from that of the simple aluminum tube.

7.3.2 Built-Up Structure

The so-called built-up structure avoids tensile stresses, in fact excessive stresses and strains of any kind, by isolating the liner from the rock cavity by means of a crushable backpacking layer. The crush stress of the backpacking is selected to be equal to the desired

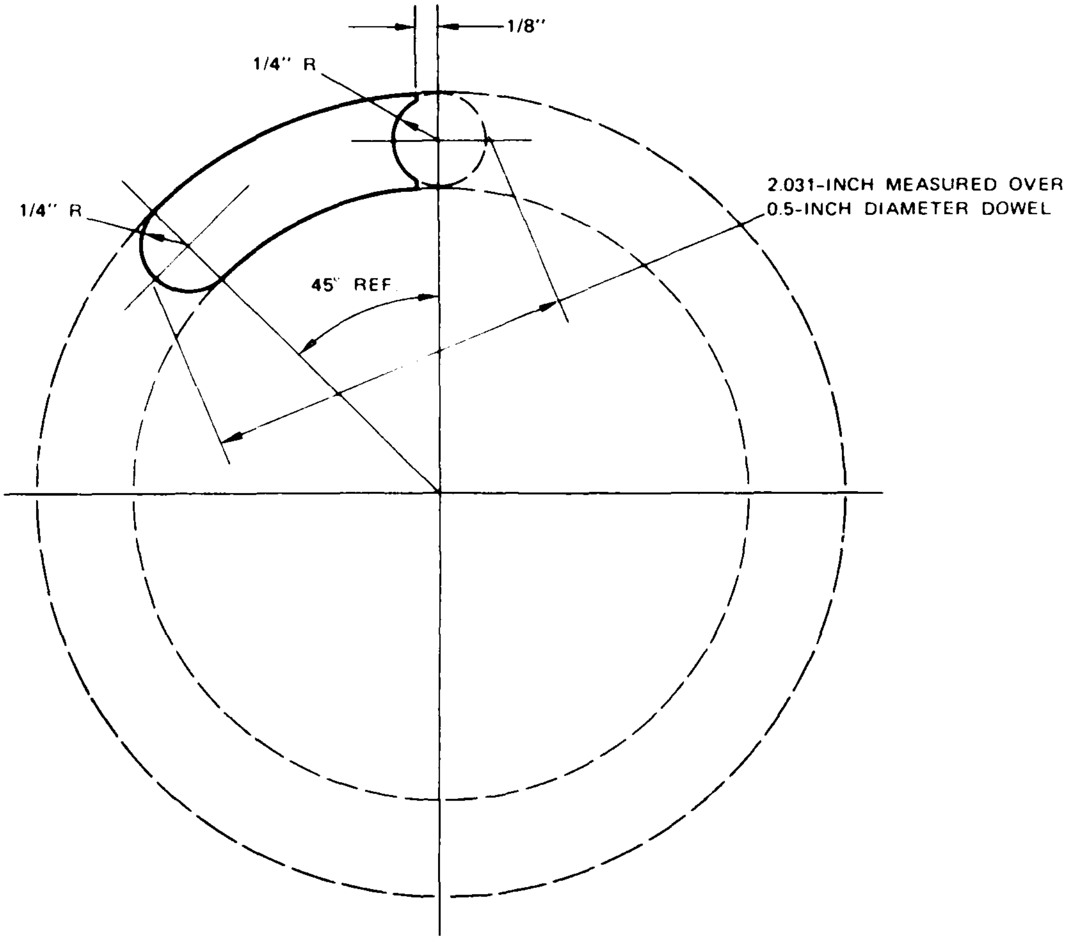

8 REQUIRED
CUT FROM 3.5-INCH-I.D. x 0.50-INCH-THICK
WALL EXTRUDED TUBING LENGTH 28 INCHES

MATERIAL: ALUMINUM 6061-T6
AFTER MACHINING, ANNEAL TO
6061-T0 CONDITION
ASSEMBLE SEGMENTS WITH SCOTCH
BRAND MAGIC TRANSPARENT TAPE
NO. 810 BETWEEN SEGMENTS

MA-4121-1

FIGURE 7.1 DESIGN DETAIL FOR THE ALUMINUM VOUSSOIR BLOCK MODEL

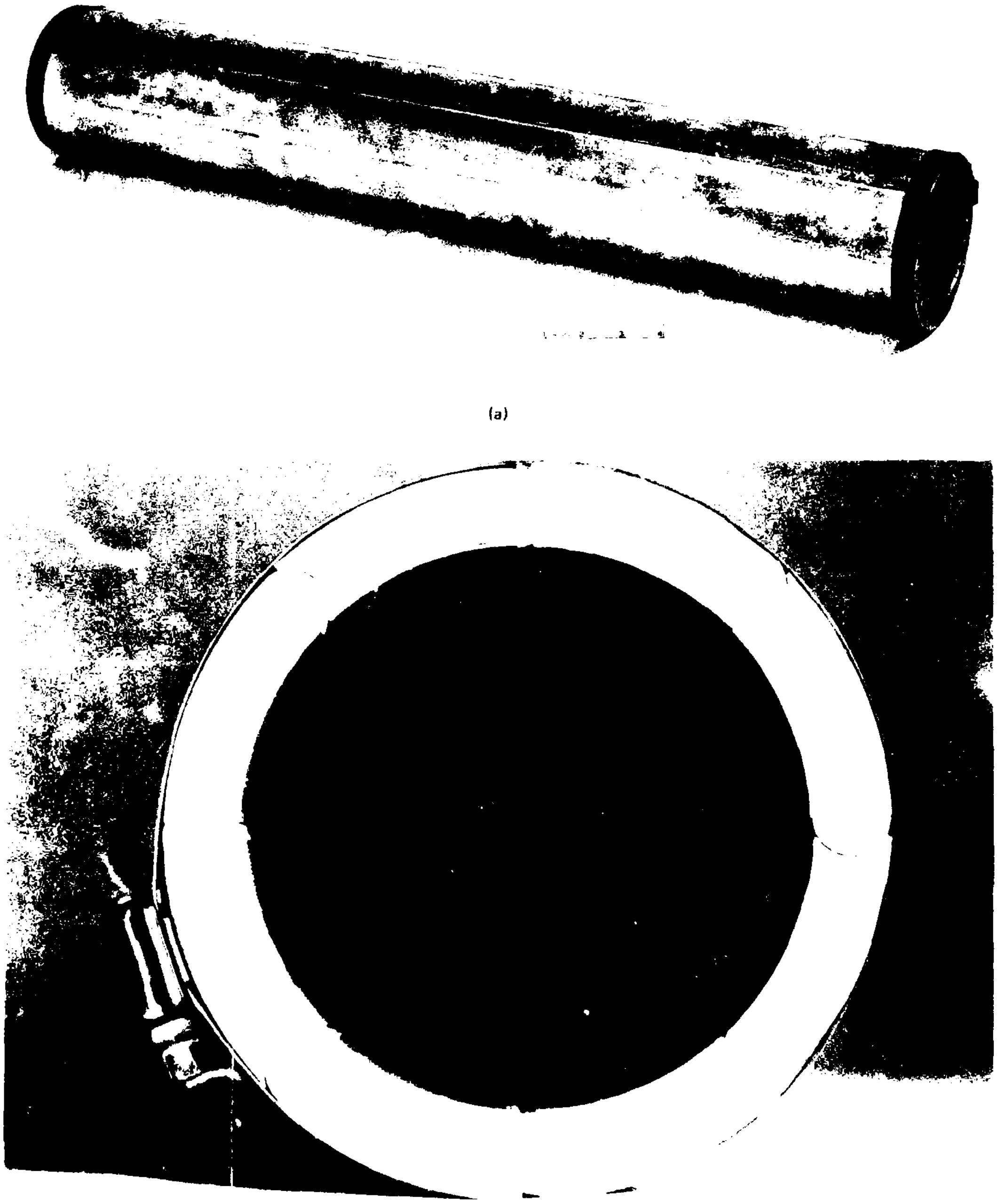

(a)

(b)

MP 4121 2

FIGURE 7.2 ASSEMBLED VOUSSOIR BLOCK MODEL (LENGTH 28 INCHES, INSIDE DIAMETER 3.5 INCHES, WALL THICKNESS 0.50 INCH, 1 INCH = 25.4 mm)

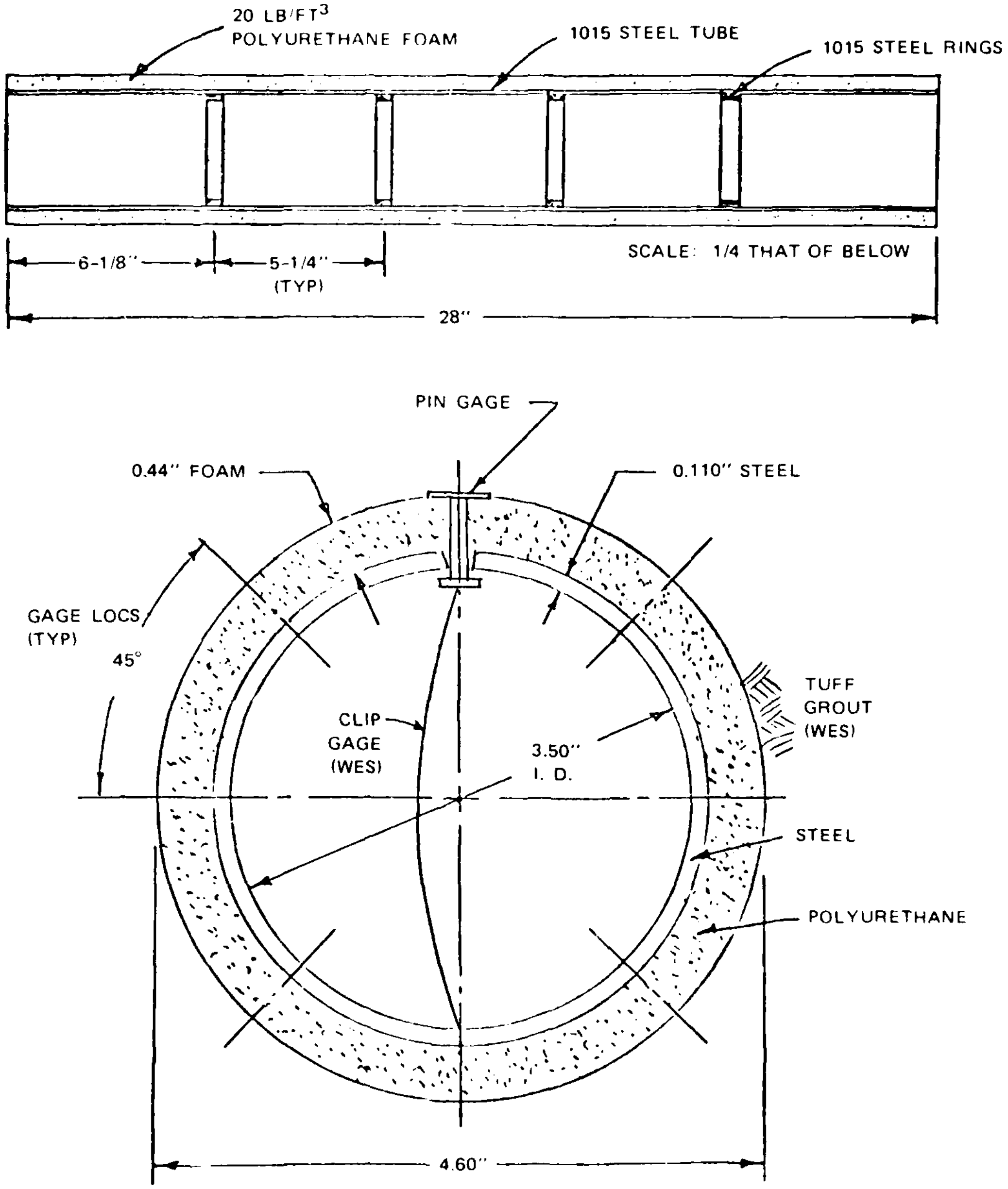

MA-4121-159

FIGURE 7.3 SECTION DRAWINGS OF BUILT-UP STRUCTURE MODEL supporting pressure at the interface with surrounding rock. The internal liner is then designed to carry this pressure elastically. Because the liner loads are elastic, even though the cavity closure is several percent, the liner can be "built-up" in place from relatively thin steel members because they have a buckling strength proportional to the elastic modulus, which is two orders of magnitude larger than the plastic modulus.

Figures 7.3 through 7.8 show the model structure used to test this approach. The backpacking is modeled with nominal 20 lb/ft^3 (32 kg/m^3) density urethane foam, which has a mean crush stress of about 1500 psi (10.4 MPa) as shown by the measured stress-strain curves in Figure 7.4. The liner is a simple cold-drawn 1015 steel tube with periodic internal ring stiffeners as shown in Figure 7.3. (Other tests, performed on similar steel liners after this structure had been designed [2], show that these rings are not really needed to avoid buckling.)

Because much of the response of the rock and reinforcing structure system takes place in the form of crushing of the backpacking, the models were equipped with radial pins (Figure 7.3 to measure this crush. Eight pins were installed at 45-degree ($\pi/4$-rad) increments around the liner and spaced along the length of the model so that there was at least one inch (25 mm) between pins. This allowed room for WES to install clip gages (as shown in the figure) to measure backpacking crush continuously throughout the test. The clip gages were installed in pairs so that one measured the local inside diameter of the liner while the other measured inside diameter to the crush pin, as in the gage shown. Backpacking crush was the difference between these measurements. The pins at the springlines had external anchors attached (Figure 7.5) so that if there was any tendency for a gap to open between the rock opening and the backpacking, the pin would follow the rock and monitor this opening.

The model and instrumentation performed well and showed that about half the elliptical rock cavity deformation was accommodated by crushing of the backpacking and half by the liner becoming oval. These

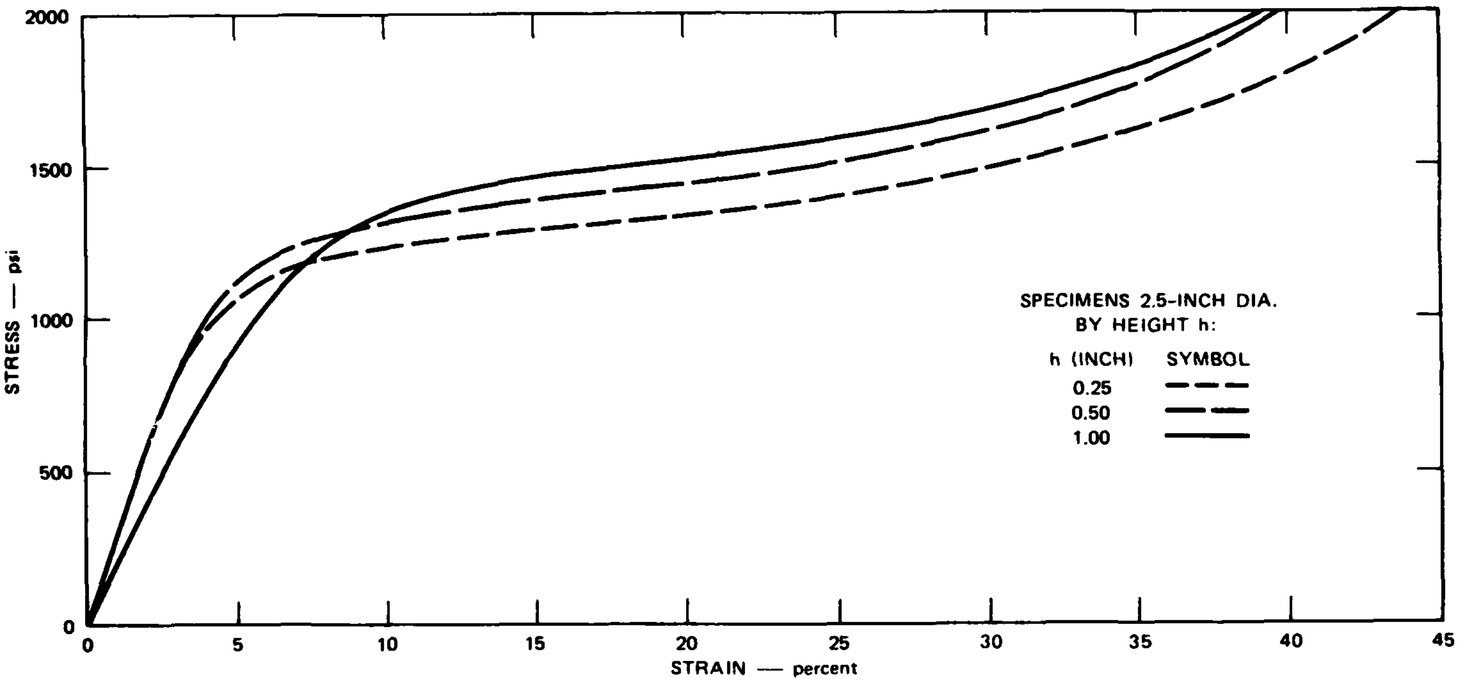

MA-4121-160

FIGURE 7.4 STRESS-STRAIN CURVES FOR URETHANE FOAM BACKPACKING IN BUILT-UP STRUCTURE MODEL
1000 psi = 6.9 MPa

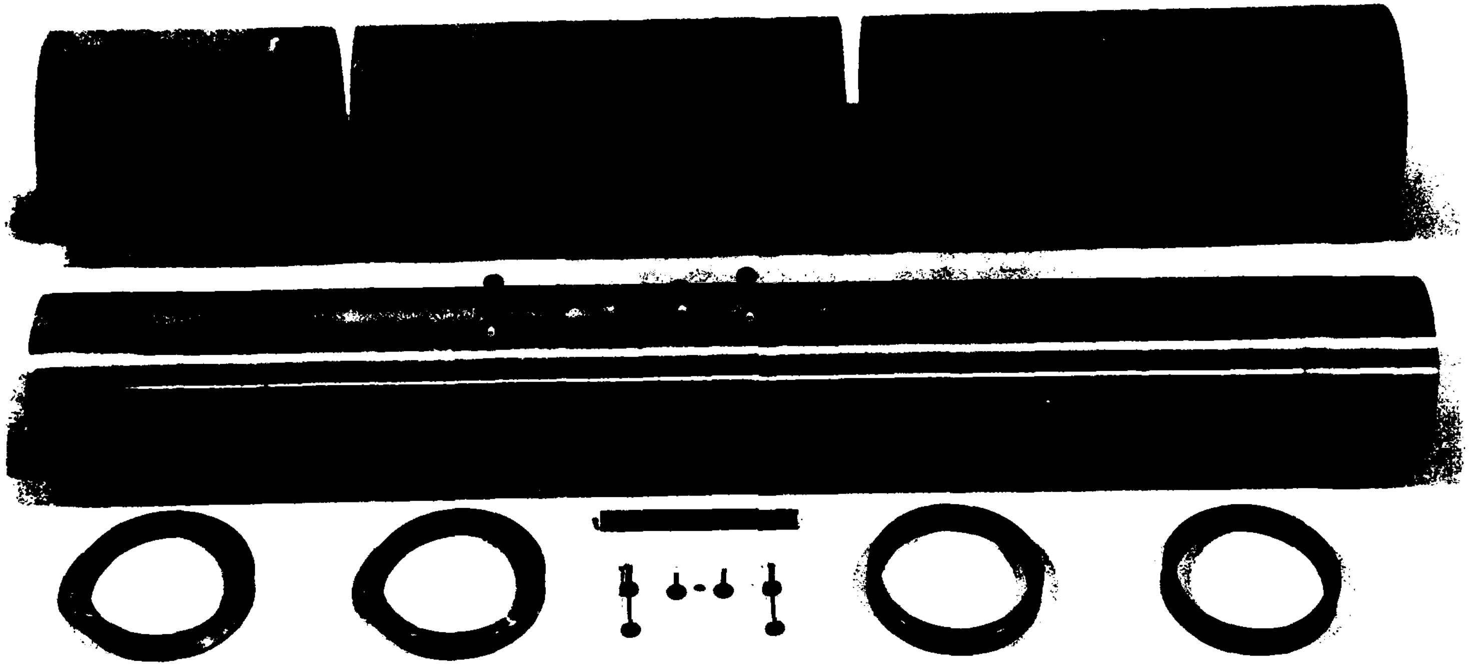

MP-4522-2

FIGURE 7.5 SCALE MODEL OF THE SRI BUILT-UP STRUCTURE PRIOR TO ASSEMBLY

Upper cylinders are 20 lb/ft^3 rigid polyurethane, center cylinder is 3.5-inch inside diameter steel liner, rings in foreground are stiffeners to be epoxied in place, and pins are foam-crush gages to be inserted through aligned holes in the foam and steel cylinders.

FIGURE 7.6 END VIEW OF 3.5 INCH I.D. SCALE MODEL OF SRI BUILT-UP STRUCTURE
Photograph shows polyurethane foam thickness, steel thickness, and internal stiffners in place.

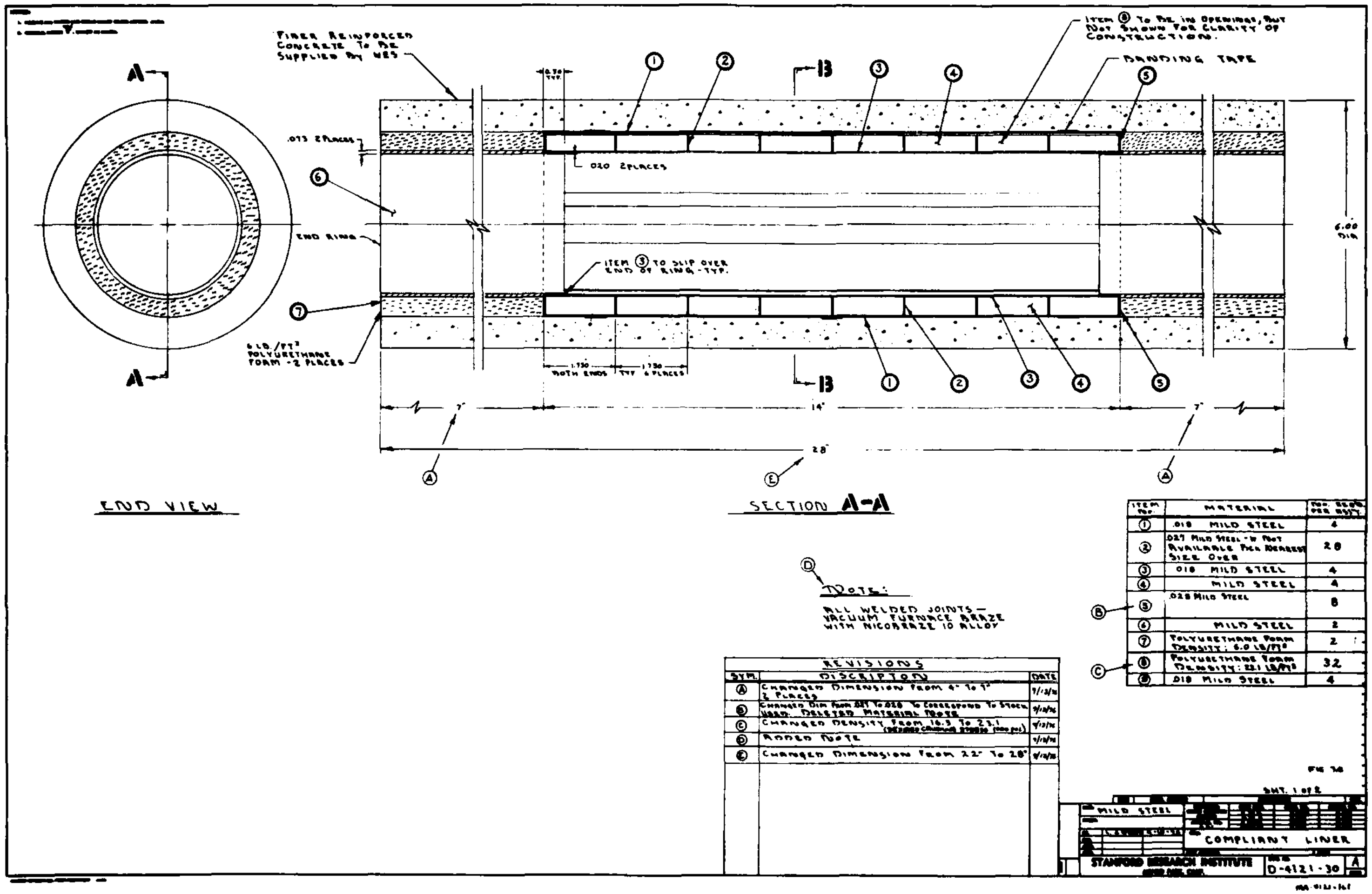

ITEM NO.	MATERIAL	NO. REQD. PER ASSY.
①	.018 MILD STEEL	4
②	.027 MILD STEEL - IF NOT AVAILABLE PICK NEAREST SIZE OVER	28
③	.018 MILD STEEL	4
④	MILD STEEL	4
⑤	.028 MILD STEEL	8
⑥	MILD STEEL	2
⑦	POLYURETHANE FOAM DENSITY: 6.0 LB/FT³	2
⑧	POLYURETHANE FOAM DENSITY: 23.1 LB/FT³	32
⑨	.018 MILD STEEL	4

REVISIONS

SYM.	DISCRIPTION	DATE
Ⓐ	CHANGED DIMENSION FROM 4" TO 7" 2 PLACES	7/13/76
Ⓑ	CHANGED DIM FROM .027 TO .028 TO CORRESPOND TO STOCK USED. DELETED MATERIAL NOTE	9/13/76
Ⓒ	CHANGED DENSITY FROM 16.3 TO 23.1 ([illegible])	9/13/76
Ⓓ	ADDED NOTE	9/13/76
Ⓔ	CHANGED DIMENSION FROM 22" TO 28"	9/13/76

FIGURE 7.7 ASSEMBLY DRAWING OF COMPLIANT LINER

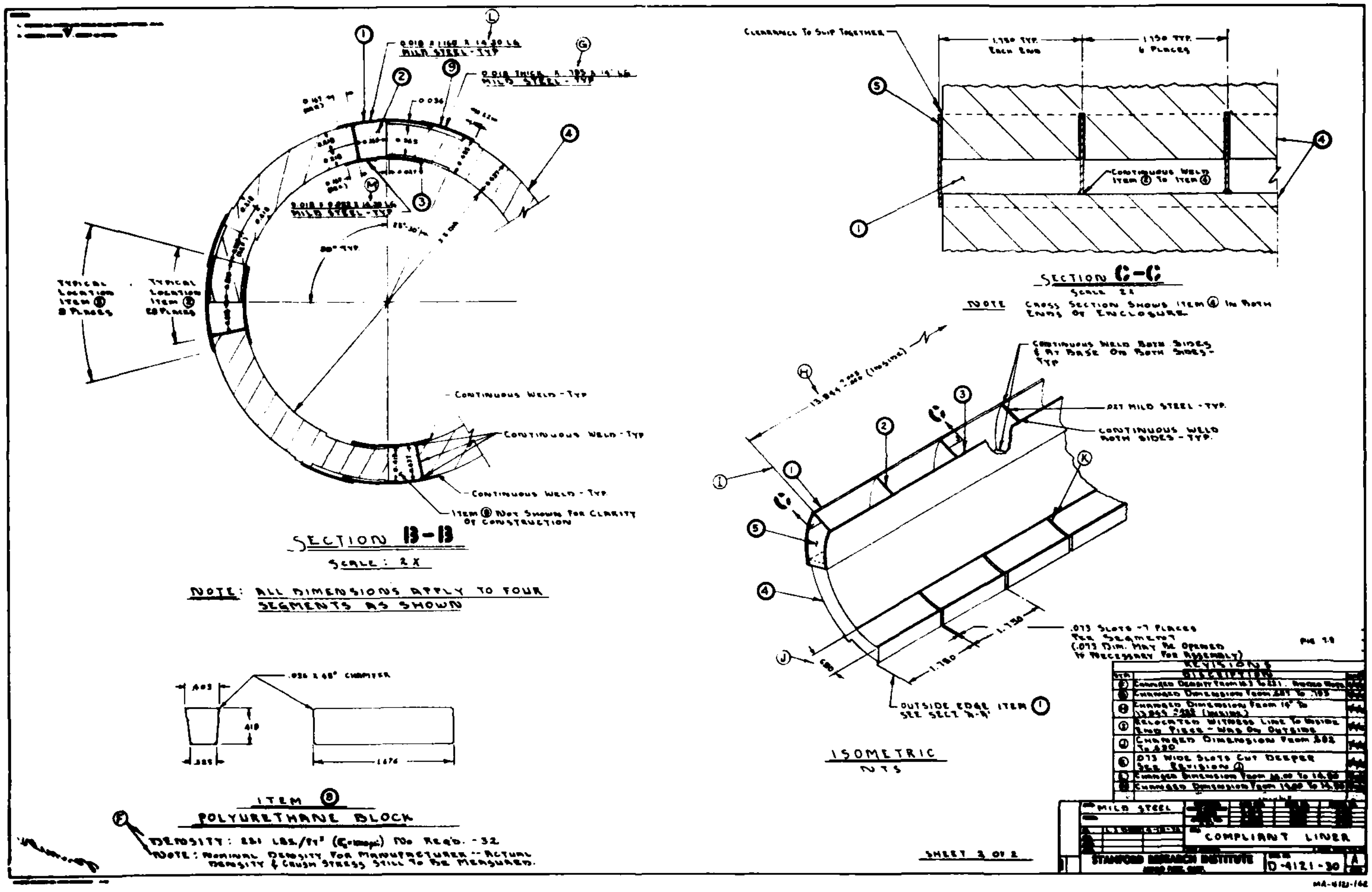

FIGURE 7.8 SEGMENT DETAIL DRAWING OF COMPLIANT LINER

results proved to be an accurate prediction of response observed in 4-foot-inside-diameter (1.3-m) structures tested in Mighty Epic [10].

7.3.3 Compliant Structure

The compliant structure avoids large plastic strains in the interior liner by introducing compliant pistons between arc segments of the liner. Imagine, for example, that in the voussoir block liner in Figure 7.2 the block segments are connected by piston-receiver joints rather than by rotating joints. The overall hoop strain of the liner is then concentrated into rigid body displacements between joints. The joints and therefore liner are given hoop strength by introducing a finite strength, crushable foam into the receiver chamber at each joint. Construction drawings of these joints and the entire model structure made for WES are given in Figures 7.7 and 7.8.

These drawings are the result of designing a scale model of the 48-inch-inside-diameter (1.3-m) compliant structure design given by Merritt-CASES, Drawing No. 7500. This design is of a structure that was originally proposed to be fielded in Mighty Epic but was instead tested in this scale model program. In the larger structure, the segments were to be made of reinforced concrete and the crushable insert material was to be 1000-psi (6.9-MPa) cellular concrete. Since the unique feature of the compliant structure is the crushing joints, our model focused on accurately modeling these joints while keeping the remainder of the model strong and simple so that it would not fail and confuse the test results. The main features of the small-scale model are:

- The steel-bar reinforced concrete in the four segments in the 4-foot (1.3-m) structure is modeled with solid steel, under the assumption that in a full-scale structure the reinforced concrete remains elastic (our model focuses on the compliant joint action and overall interaction with the surrounding rock).

- All materials and dimensions in the compliant joints are scale replicas of those in the 4-foot (1.3-m) structure (the interior of the male side of the model is solid steel, assuming that in a full-scale structure this element can always be made very strong compared with the rest of the joint).
- The crushable material in the joints is urethane foam rather than cellular concrete, but with the same nominal 1000-psi (6.9-MPa) crushing strength (actual crush properties measured on the material used to make the models showed an average strength of about 800 psi (5.5 MPa, Figure 7.9).
- All dimensions in the model are 3.5 inches/48 inches = 1/13.72 times the corresponding dimensions in the 4-foot (1.3-m) structure, including the length.
- To accommodate the resulting 14-inch (0.35-m) length of the model to the 28-inch (0.7-m) length required for the WES testing machine, we added 7-inch (0.18-m) long extensions to each end of the model. These extensions consisted of a 0.073-inch-thick (1.85-mm) steel liner (which scales to 1-inch (25-mm) thickness in a 4-foot (1.3-m) structure) surrounded by a layer of 6 lb/ft^3 (9.5 kg/m^3) density urethane foam with a crushing strength of 100 psi (0.69 MPa). The 100 psi (0.69 MPa) is somewhat smaller than the uniform pressure exerted on the compliant liner when the 800 psi (5.5 MPa) urethane inserts in the joints are crushing (that is, 160 psi (1.1 MPa) = 800 psi (5.5 MPa) x 6-inch (.15-m) wall thickness/30-inch (0.76-m) radius at compliant liner surface). Thus these extensions are the closest possible simple structural match to the compliant liner, to minimize any discontinuity at the end of the compliant liner. Also, since these end extensions are crushable and flexible, they minimize any tendency of the testing machine end fittings to bind up the compliant mechanisms.
- The fiber-reinforced concrete around the compliant liner was made by WES by casting directly around the structure assembly provided by SRI.

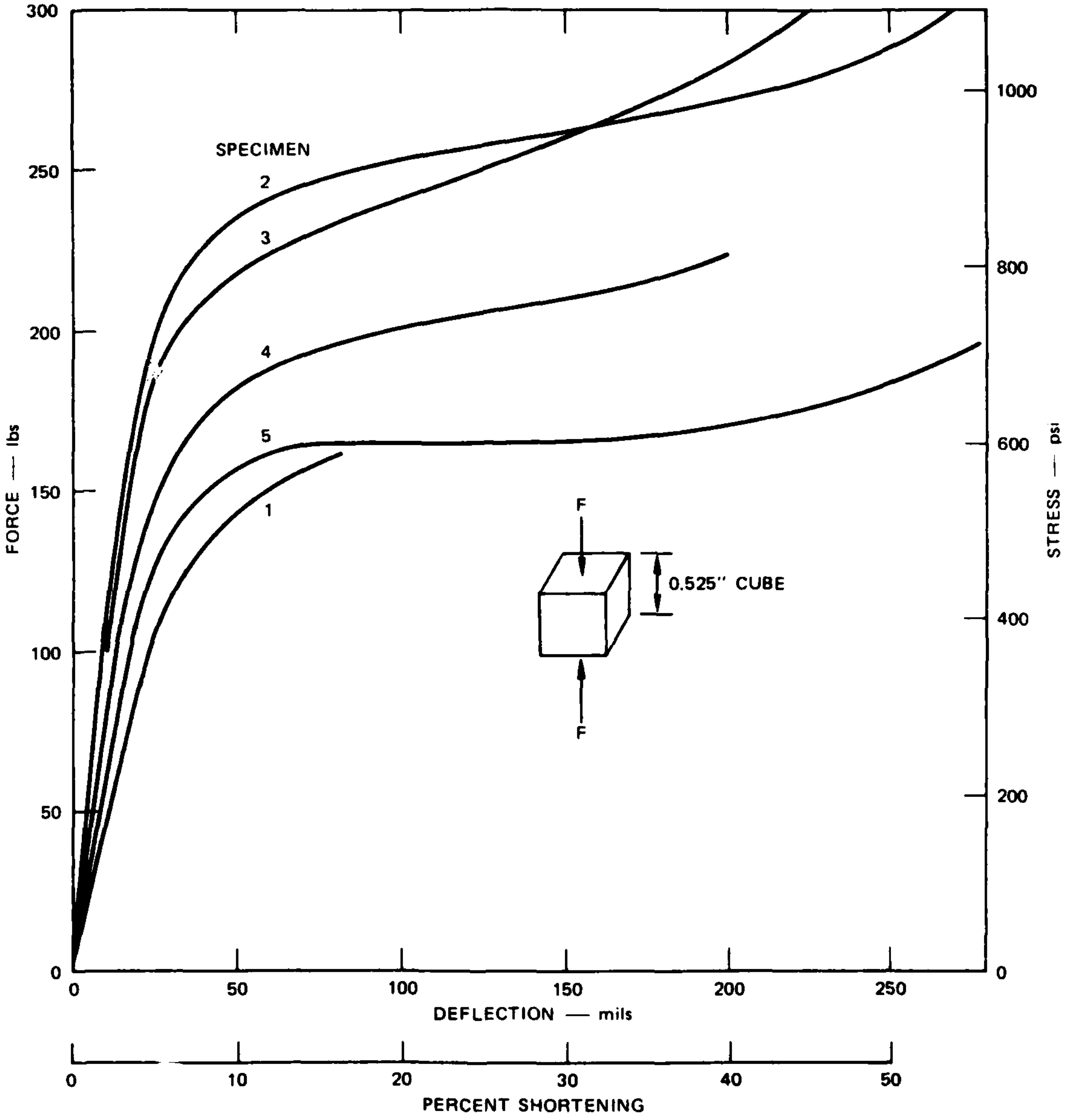

MA-4121-163

FIGURE 7.9 STRESS-STRAIN CURVES FOR URETHANE FOAM USED IN COMPLIANT LINER SEGMENTS (1 psi = 6.9 kPa)

Photographs of the scale-model compliant liner are shown in Figures 7.10 and 7.11. The first photograph, Figure 7.10 (a), shows one segment of the liner completely disassembled. The second photograph shows a segment with the male and female sections welded together and one crushable polyurethane foam insert in place in the female section. The photograph in Figure 7.11 (a) shows one end of the fully assembled compliant liner. The four segments that make up the liner are held together with three bands of glass tape. The outer segment seams (between each grout shield plate and the adjacent segment) have been sealed with glass tape to prevent water damage to the foam. The fourth photograph shows an overall view of the assembled model with the extensions in place.

The completed model was received at WES on July 8, 1976. At WES, the fiber-reinforced concrete outer structure was added and then the entire model was cast in place into an SRI RMG 2C2 grout block in the WES testing machine. The test was performed on October 13 and was witnessed by Sun Ju Hung of CASES and H. E. Lindberg of SRI, in addition to the WES staff and program director Capt. R. Kanda. The test went well, with the active instrumentation indicating that the model performed as planned. Detailed results of this test and those on the other models are available from WES.

7.4 EXAMPLE TEST RESULTS

Figure 7.12 gives section photographs of rocks and structures after testing for a nominally unlined tunnel and for three of the four structures described here. Springline fractures around the unlined tunnel are very similar to those observed in the Dining Car 1-m-diameter 6B rock models [10]. The similarity in tunnel deformation for the simple aluminum and the aluminum Vussoir block models is apparent.

Figure 7.13 summarizes the vertical pressures required to produce a 0.2-inch (5.1-mm) closure (5.7%) in each of the five liner types. The bar for each type is placed at a pressure corresponding to the nominal hoop strength of the structure. A smooth curve can be

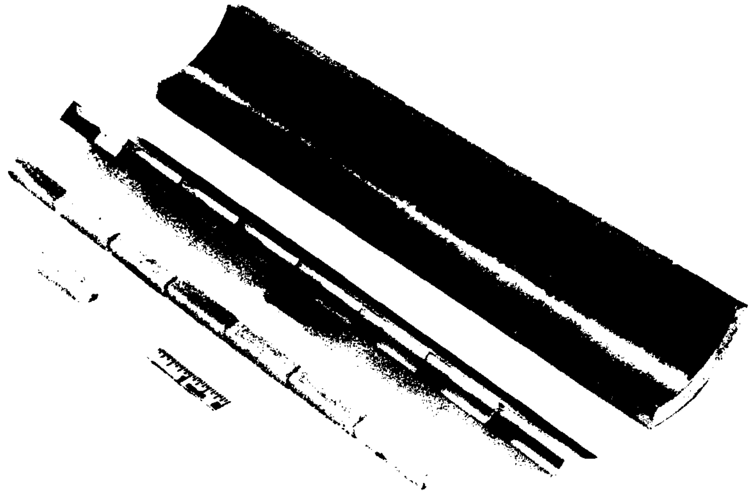

(a) SINGLE SEGMENT, UNASSEMBLED

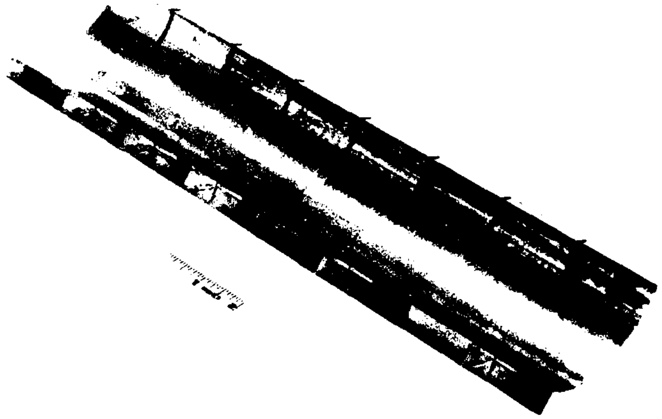

(b) SINGLE SEGMENT, ASSEMBLED SHOWING LOCATION OF POLYURETHANE FOAM

MP-4121-49

FIGURE 7.10 COMPLIANT LINER SEGMENTS

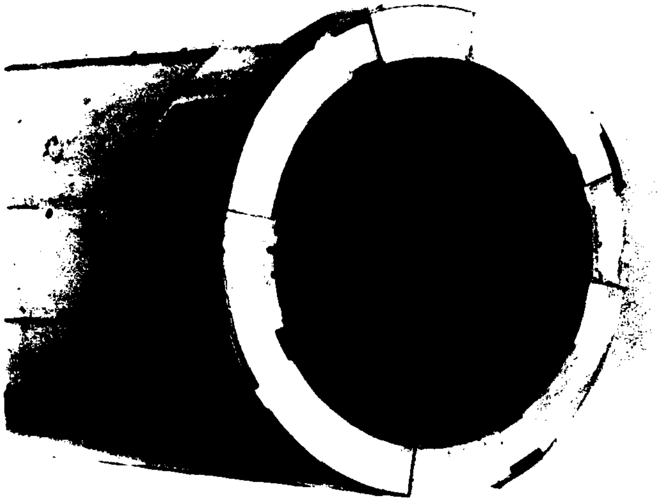

(c) END VIEW OF FULLY ASSEMBLED COMPLIANT LINER MODEL

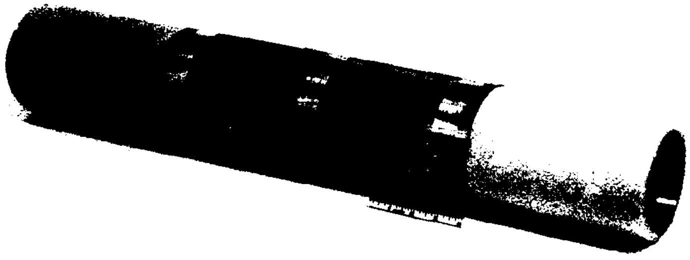

(d) OVERALL VIEW OF FULLY ASSEMBLED COMPLIANT LINER MODEL WITH EXTENSIONS IN PLACE

MP-4121-50

FIGURE 7.11 ASSEMBLED COMPLIANT LINER

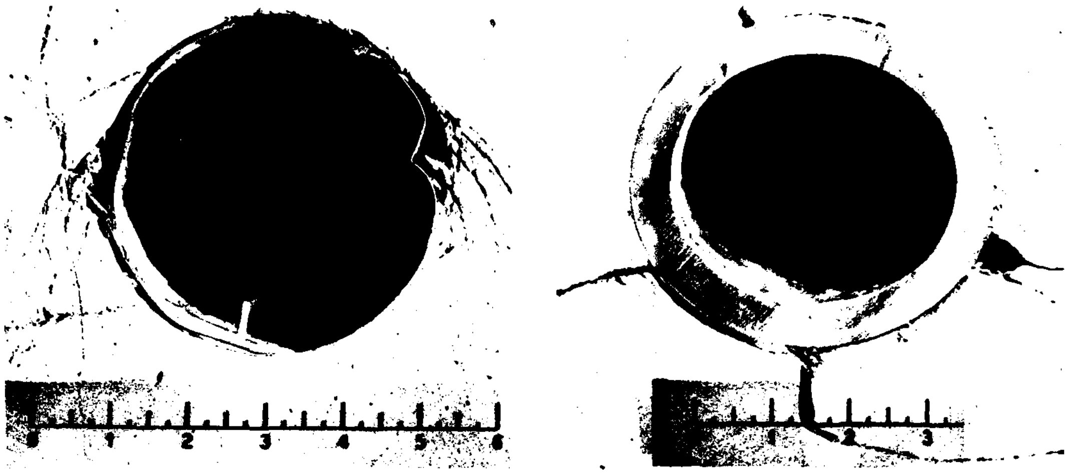

(a) UNLINED TUNNEL

(b) ALUMINUM 6061-T0 STRUCTURE

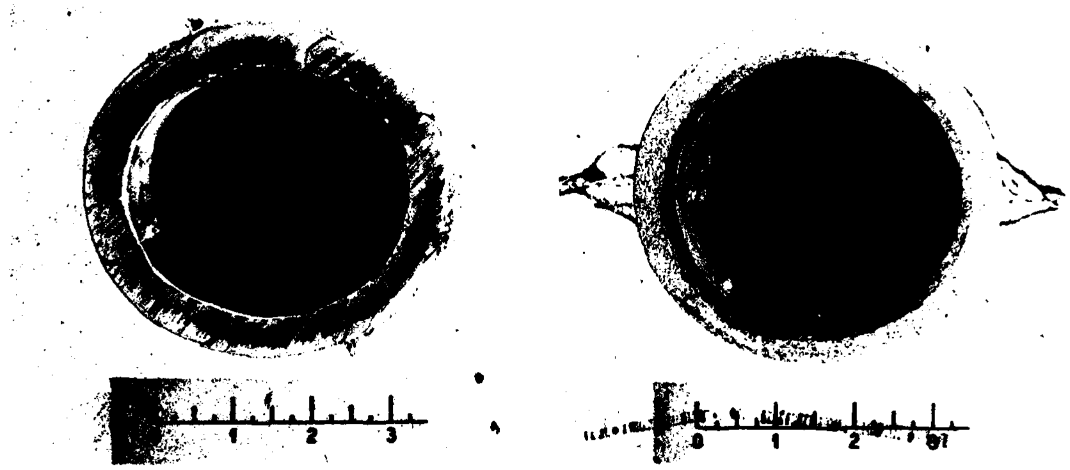

(c) ALUMINUM 6061-T0 VUSSIOR BLOCK STRUCTURE

(d) BUILT-UP STRUCTURE

MP-4121-164

FIGURE 7.12 SECTIONED ROCK AND TUNNEL STRUCTURES AFTER TESTING AT WES

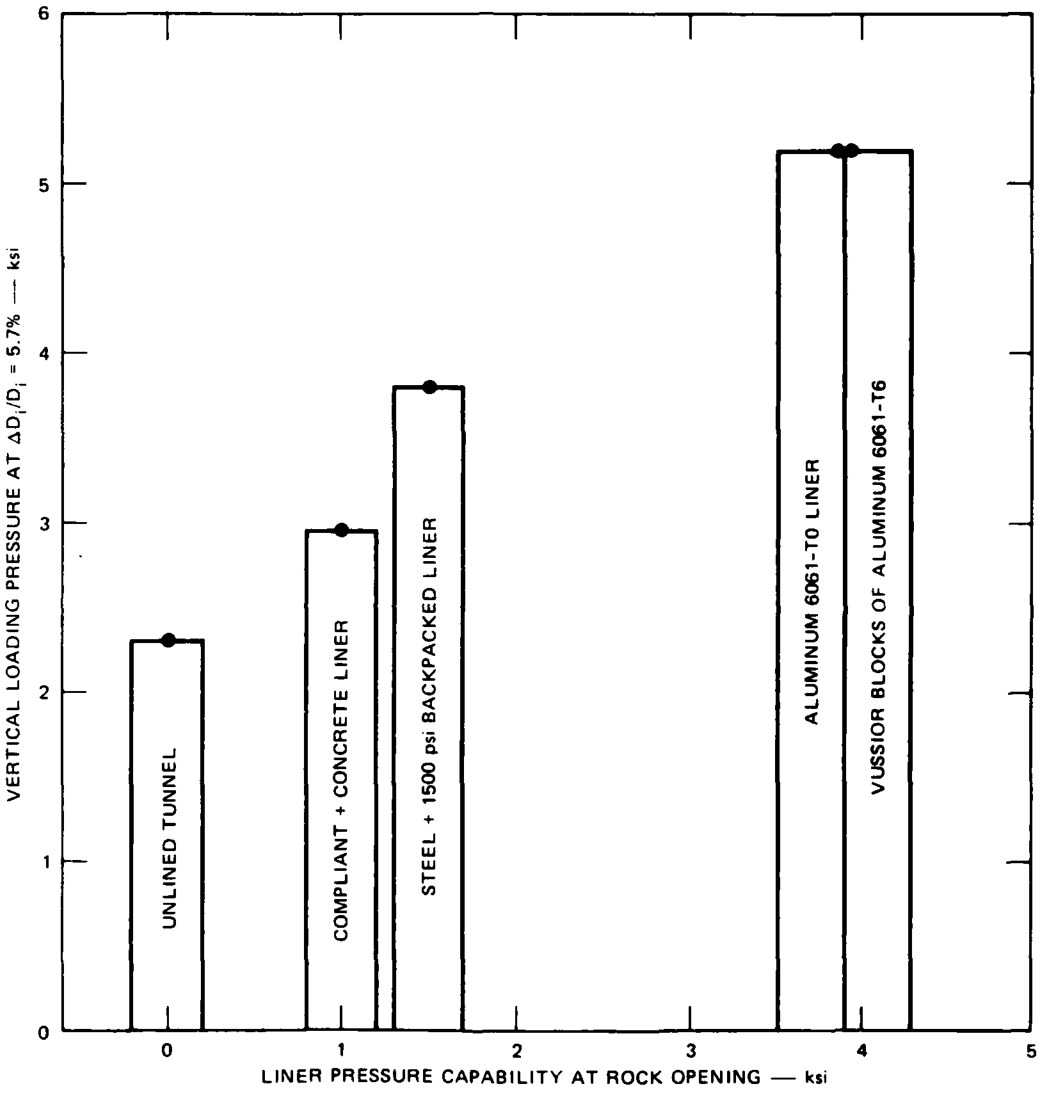

MA-4121-165

FIGURE 7.13 VERTICAL LOADING PRESSURES TO PRODUCE 0.1-INCH INSIDE DIAMETER CLOSURES ($\Delta D_i/D_i$ = 5.7%) IN TUNNELS TESTED AT WES (1 ksi = 6.9 MPa) passed through the data points at the tops of the bars, suggesting that the rock simulant and test procedures were reproducible. More extensive results, including closures, strains, foam crush, for the various models, are being reported by WES. For these relatively complex structures, these detailed results are more important than the overall strength results in Figure 7.13 because they give valuable design information on the mechanisms of deformation.

REFERENCES

1. T. C. Kennedy, J. V. Zaccor, and H. E. Lindberg, "Laboratory Investigation of Deep-Based Structures," SRI International Final Report, DNA 3610F, Menlo Park, California (October 1975).

2. T. C. Kennedy and H. E. Lindberg, "Laboratory Investigation of Rock Cavity Reinforcement," SRI International Final Report DNA 4023F, Menlo Park, California (April 1976).

3. A. J. Hendron and A. K. Aiyer, "Stresses and Strain Around a Cylindrical Tunnel in an Elasto-Plastic Material with Dilatancy," Omaha District, Corps of Engineers, DACA 45-69-C-0100 (September 1972).

4. A. L. Florence and L. E. Schwer, "Axisymmetric Compression of a Mohr-Coulomb Medium Around a Circular Hole," accepted for publication in the *International Journal for Numerical and Analytical Methods in Geomechanics*.

5. Scott W. Butters, Terra Tek, Inc., Salt Lake City, Utah. Personal communication.

6. S. Timoshenko and J. N. Goodier, *Theory of Elasticity*, McGraw-Hill Book Company, New York, New York, (1951).

7. J. C. Jaeger and N.G.W. Cook, *Fundamentals of Rock Mechanics*, Chapman and Hall, Ltd., London, (1971).

8. S. W. Butters, et al., "Mechanical Properties of Nevada Test Site Tuffs from Selected Exploratory Drill Holes," Terra Tek, Inc., Report No. DNA 3181F, (September 1973).

9. P. E. Senseny and H. E. Lindberg, "Theoretical and Laboratory Study of Deep-Based Structures in Support of Diablo Hawk," SRI International Interim Report, PYU 5762, Menlo Park, California, (February 1978).

10. H. E. Lindberg, "Large- and Small-Scale Deep-Buried Structures Experiment," SRI International. Unpublished.

11. T. C. Kennedy and H. E. Lindberg, "Model Structures Experiment on Monocoque and Backpacked Liners," Hussar Sword Series, Dining Car Event, SRI International. Unpublished.

Appendix A

THE EFFECT OF A NONLINEAR MOHR-COULOMB TYPE YIELD ENVELOPE ON TUNNEL CLOSURE

Until now, we have analyzed the closure of deep-based structures under symmetric loading with an elastic-plastic theory incorporating the Mohr-Coulomb yield criterion with the yield envelope assumed to be a straight line (constant friction angle). The yield envelope for tuff and many other rocks is not a straight line but a curve with a continuously decreasing slope, as shown in Figure A.1(a) (σ_1 is the maximum principal stress, and σ_3 is the minimum principal stress). We may represent such a yield envelope, to any degree of accuracy we like, by a series of straight line segments (f_1, f_2, ... f_{n+1}) with different slopes (tan ω, tan ω_2, ... tan ω_{n+1}), as shown in Figure A.1(b). Along each segment, we define the yield function by $f(\sigma_1, \sigma_3) = 0$. This envelope may be interpreted as follows: for values of the minimum principal stress σ_3 less than p_1, the line f_1 is the yield envelope; for values of σ_3 between p_1 and p_2, the line f_2 is the yield envelope; and so on. This may be represented mathematically as:

$$\text{for } p_{j-1} < \sigma_3 < p_j \,, \qquad f = f_j = \sigma_1 - N_j \sigma_3 - \sigma_{uj} = 0 \qquad \text{(A-1)}$$

where

$$N_j = 1 + \tan \omega_j \qquad \text{(A-2)}$$

and σ_{uj} is the point where this line segment, if continued, would intercept the vertical axis. The relation between this yield criterion, given

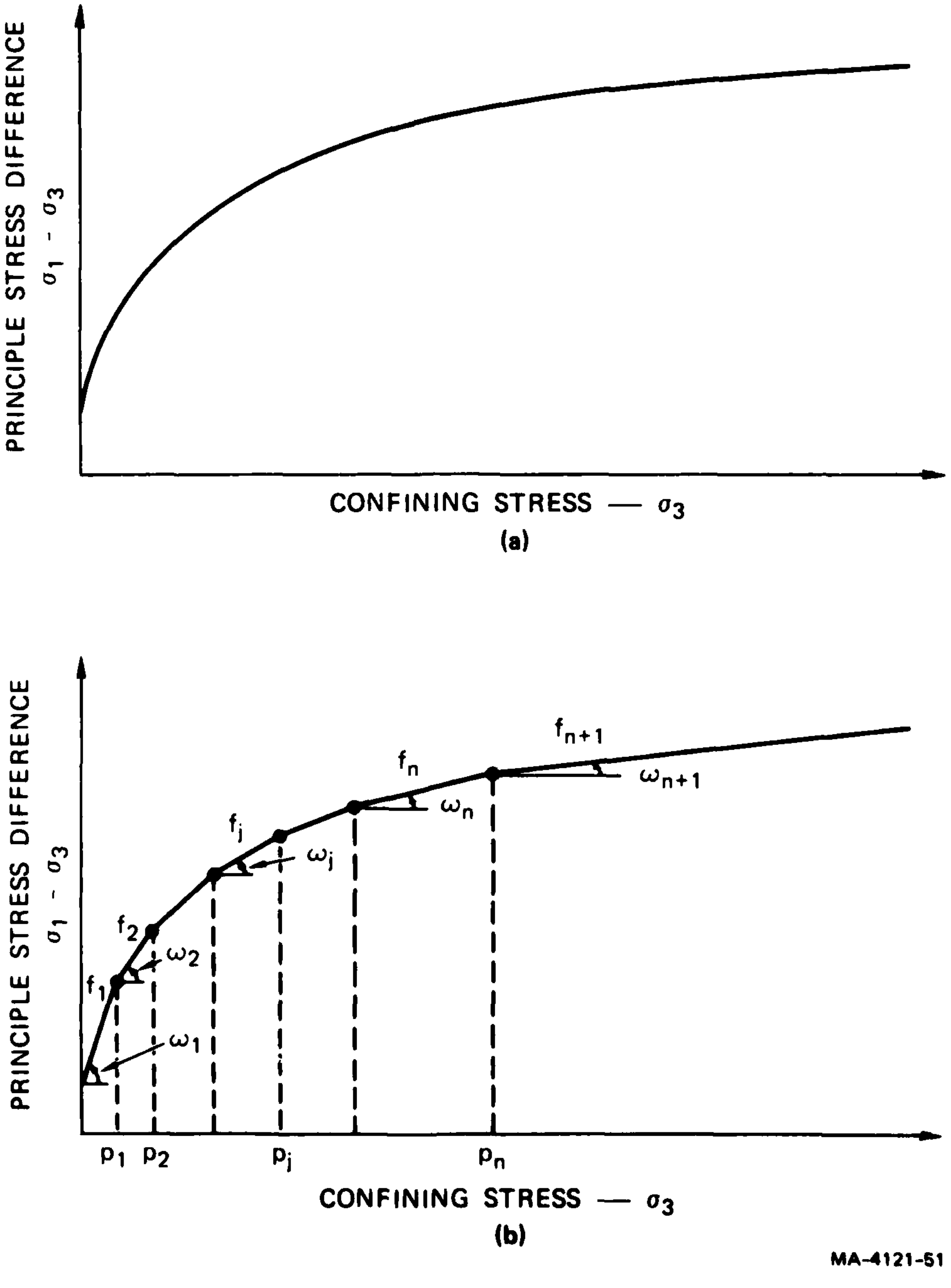

FIGURE A.1 NONLINEAR MOHR-COULOMB TYPE OF YIELD ENVELOPE in $\sigma_1 - \sigma_3$ versus σ_3 space, and the usual Mohr-Coulomb criterion given in τ (shear stress) versus σ_n (normal stress) space, is presented in Appendix B. For a nonlinear yield envelope, it is more convenient to work in $\sigma_1 - \sigma_3$ versus σ_3 space, where states of stress at yield correspond to points on the yield envelope. In τ versus σ_n space, states of stress at yield are determined by Mohr circles tangent to the yield envelope so that the yield envelope cannot have corners.

We will use a yield envelope like the one shown in Figure 1(b) to analyze the elastic-plastic, axisymmetric closure of a tunnel and compare the results to an analysis where the yield envelope is represented by a single straight line. The tunnel is represented by a cylindrical cavity with radius a in an infinite body of rock subjected to a free field pressure P_o and an internal pressure P_i, as shown in Figure A.2. A cylindrical r, θ, z coordinate system is used, with r being the radial distance from the center of the cavity, θ being the angular coordinate about axis of the cavity, and z being the coordinate along the axis of the cavity. The cavity is assumed to be of infinite extent along the z axis, and a plane strain ($\epsilon_z = 0$) condition is assumed to hold.

We assume that the internal and free field pressures are applied in such a way that the internal pressure reaches its maximum value before yielding of the rock occurs. As P_o is increased, yielding will take place first on the inner boundary of the cylinder. As P_o is increased further, the yielded region will move out to some radius R until the load has reached its peak. Consequently, there will be a plastic region between $r = a$ and $r = R$ and a completely elastic region between $r = R$ and $r = \infty$.

A.1 General Relations

We will study the elastic and plastic zones separately, but first let us consider the governing equations that are valid for both zones:

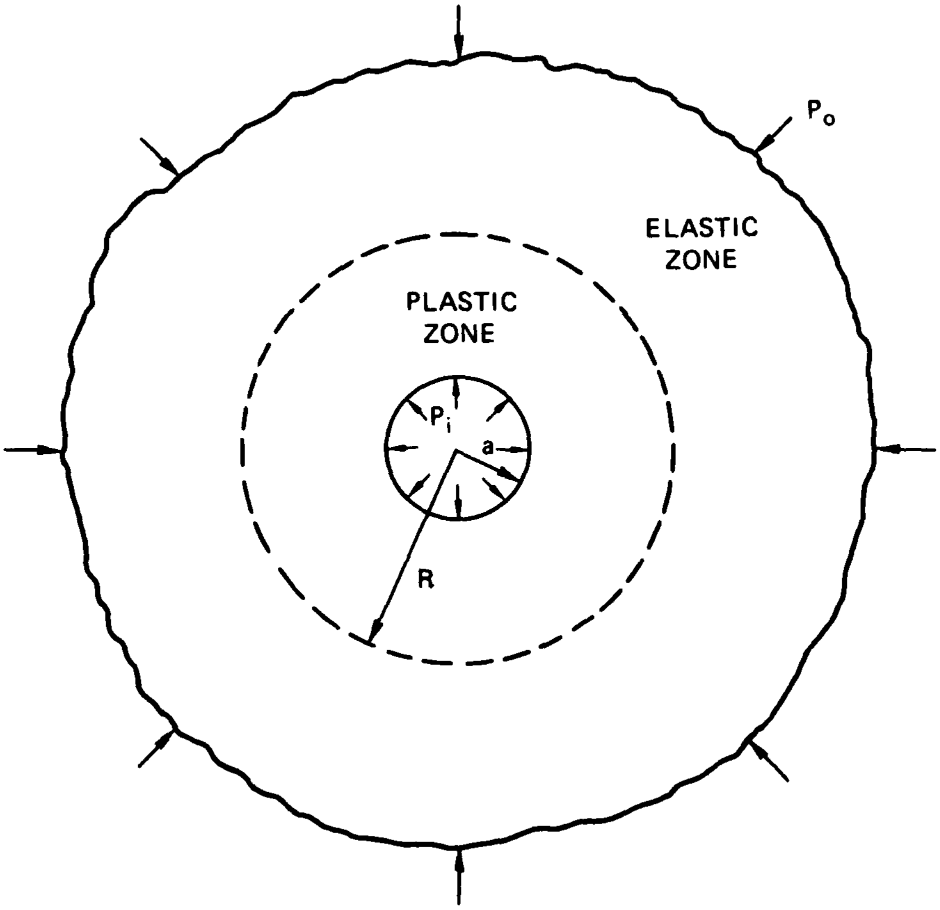

MA-4121-52

FIGURE A.2 ELASTIC-PLASTIC RESPONSE OF A CYLINDRICAL CAVITY IN ROCK

Equilibrium equation:

$$\frac{d\sigma_r}{dr} + \frac{\sigma_r - \sigma_\theta}{r} = 0 \qquad \text{(A-3)}$$

Boundary conditions:

$$\sigma_r = P_i \quad \text{at } r = a$$

$$\sigma_r = P_o \quad \text{at } r = \infty \qquad \text{(A-4)}$$

where compressive stress is positive.

Strain-displacement relations:

$$\epsilon_r = \frac{du}{dr} \qquad \epsilon_\theta = \frac{u}{r} \qquad \text{(A-5)}$$

Compatibility equation:

$$\frac{d\epsilon_\theta}{dr} + \frac{\epsilon_\theta - \epsilon_r}{r} = 0 \qquad \text{(A-6)}$$

Stress-strain relations:

$$\epsilon_r = \frac{1}{E}\left[\sigma_r - \nu(\sigma_\theta + \sigma_z)\right] + \epsilon_{rp}$$

$$\epsilon_\theta = \frac{1}{E}\left[\sigma_\theta - \nu(\sigma_r + \sigma_z)\right] + \epsilon_{\theta p}$$

$$\epsilon_z = \frac{1}{E}\left[\sigma_z - \nu(\sigma_r + \sigma_\theta)\right] + \epsilon_{zp} \qquad \text{(A-7)}$$

where E and ν are Young's modulus and Poisson's ratio, respectively; ϵ_r, ϵ_θ, ϵ_z are the total strains; and ϵ_{rp}, $\epsilon_{\theta p}$, ϵ_{zp} are the plastic strains. For plane strain we have*

$$\epsilon_z = 0 \quad \text{and} \quad \epsilon_{zp} = 0 \tag{A-8}$$

so that

$$\sigma_z = \nu(\sigma_r + \sigma_\theta) \quad . \tag{A-9}$$

The expressions for ϵ_r and ϵ_θ become

$$\epsilon_r = \frac{(1 - \nu^2)}{E} \left(\sigma_r - \frac{\nu}{1 - \nu} \sigma_\theta\right) + \epsilon_{rp}$$

$$\epsilon_\theta = \frac{(1 - \nu^2)}{E} \left(\sigma_\theta - \frac{\nu}{1 - \nu} \sigma_r\right) + \epsilon_{\theta p} \tag{A-10}$$

which may be simplified to

$$\epsilon_r = \frac{1}{E'} \left(\sigma_r - \nu'\sigma_\theta\right) + \epsilon_{rp}$$

$$\epsilon_\theta = \frac{1}{E'} \left(\sigma_\theta - \nu'\sigma_r\right) + \epsilon_{\theta p} \tag{A-11}$$

where

$$E' = \frac{E}{(1 - \nu^2)} \qquad \nu' = \frac{\nu}{1 - \nu} \quad . \tag{A-12}$$

---

*The fact that $\epsilon_{zp} = 0$ follows from the flow rule, as will be discussed later.

A.2 Development of Plastic Zone

From a previous analysis using a linear Mohr-Coulomb failure envelope [1,3] we know that the stress distribution as a function of distance away from the cavity has the form shown in Figure A.3(a). The maximum principal stress is the tangential stress σ_θ, and the minimum principal stress is the radial stress σ_r. We see that σ_r is a monotonically increasing function of r. This means that close to the cavity, where σ_r is between P_i and p_1, $f = f_1$ will be the yield condition. This yield condition will hold until $\sigma_r = p_1$ at $r = R_1$. For σ_r between p_1 (at $r = R_1$) and p_2 (at $r = R_2$), $f = f_2$ will be the yield condition, and so on. This process continues until we reach the elastic-plastic boundary at $r = R_m$, where $m \leq n + 1$ ($n + 1$ is the number of straight line segments in the yield envelope). Consequently, within the plastic region, there exists a number (m) of zones [Figure A.3(b)] where different straight line segments of the yield envelope [Figure A.1(b)] apply as the yield condition. In this discussion, we have assumed that P_i is less than p_1. If this is not the case, we just ignore that part of the yield envelope, where σ_3 is less than P_i, and set the first p_j which is greater than P_i equal to p_1, and p_{j+1} equal to p_2, and so on.

A.3 Calculation of Stresses

A.3.1 Plastic Region

The plastic region is divided into m zones in which different straight line segments of the yield envelope apply as the yield condition. We will analyze each of these zones individually.

In the zone closest to the cavity, the yield condition is given by

$$f = f_1 = \sigma_\theta - N_1\sigma_r - \sigma_{u1} = 0 \quad . \qquad \text{(A-13)}$$

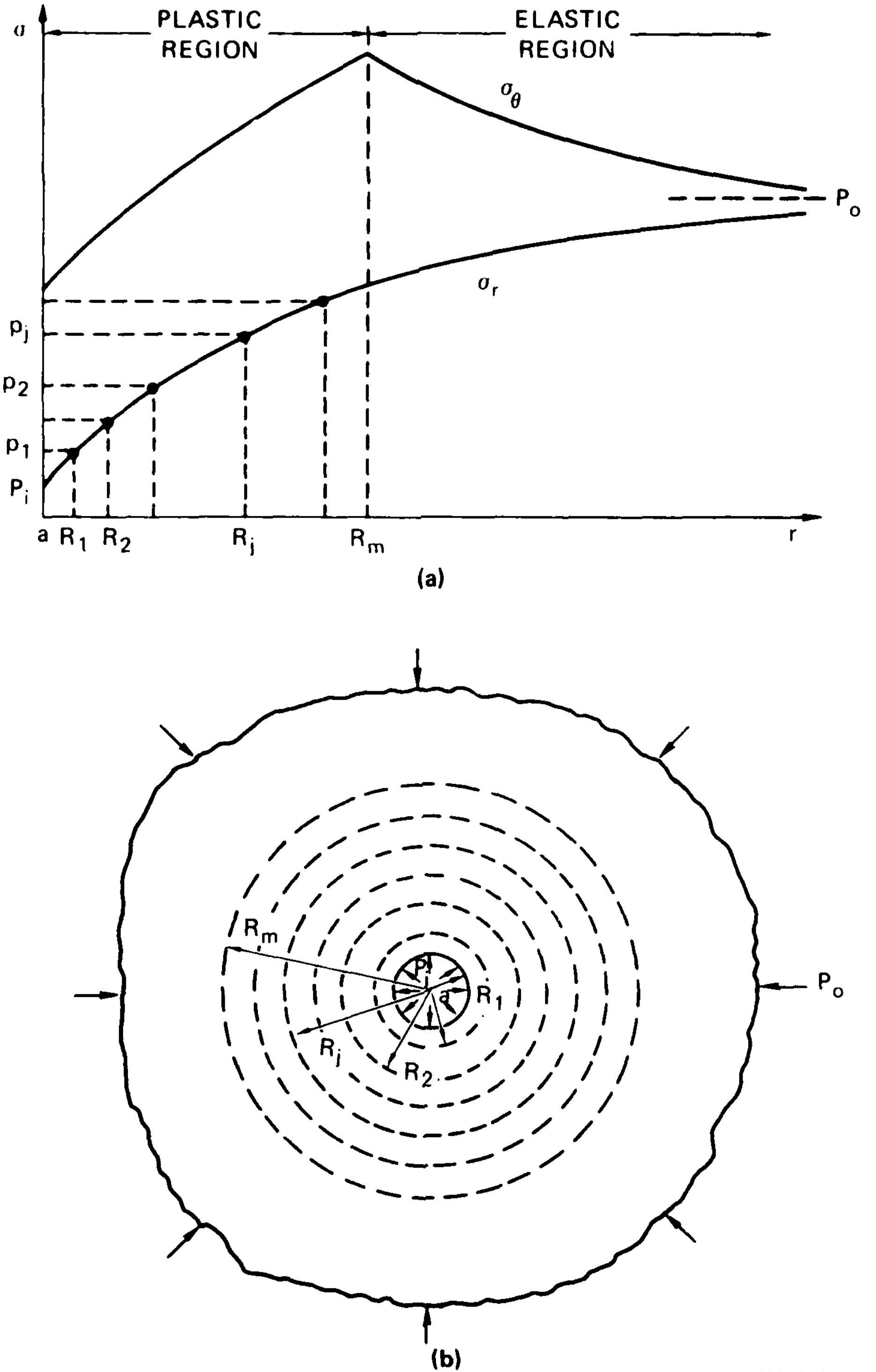

(a)

(b)

MA-4121-53

FIGURE A.3 DEVELOPMENT OF THE PLASTIC REGION AROUND THE CAVITY

Since the material is assumed to be elastic-perfectly plastic, the stresses must satisfy the yield criterion

$$\sigma_\theta = N_1\sigma_r + \sigma_{u1} \tag{A-14}$$

throughout this zone. Substitution of this equation into the equilibrium equation (A-3) gives

$$r\frac{d\sigma_r}{dr} + (1 - N_1)\ \sigma_r = \sigma_{u1} \tag{A-15}$$

which may be solved for σ_r as

$$\sigma_r = \frac{\sigma_{u1}}{1 - N_1} + Ar^{N_1 - 1} \tag{A-16}$$

where A is an unknown constant, determined by employing the boundary condition

$$\sigma_r = P_i \quad \text{at } r = a \quad . \tag{A-17}$$

This gives for A

$$A = \left(\frac{\sigma_{u1}}{N_1 - 1} + P_i\right) a^{1-N_1} \quad . \tag{A-18}$$

Consequently, the stresses in zone 1 may be expressed as

$$\sigma_r = \frac{\sigma_{u1}}{1 - N_1} + \left(\frac{\sigma_{u1}}{N_1 - 1} + P_i\right)\left(\frac{r}{a}\right)^{N_1-1}$$

$$\sigma_\theta = \frac{\sigma_{u1}}{1 - N_1} + N_1\left(\frac{\sigma_{u1}}{N_1 - 1} + P_i\right)\left(\frac{r}{a}\right)^{N_1-1} \quad . \tag{A-19}$$

We may proceed in a similar manner to obtain expressions for the stresses in each of the different zones up to zone m; for example, in zone j we would have

$$\sigma_r = \frac{\sigma_{uj}}{1 - N_j} + \left(\frac{\sigma_{uj}}{N_j - 1} + p_{j-1}\right)\left(\frac{r}{R_{j-1}}\right)^{N_j - 1}$$

$$\sigma_\theta = \frac{\sigma_{uj}}{1 - N_j} + N_j\left(\frac{\sigma_{uj}}{N_j - 1} + p_{j-1}\right)\left(\frac{r}{R_{j-1}}\right)^{N_j - 1} \quad . \qquad \text{(A-20)}$$

Expressions for R_1, R_2 ..., R_m are obtained by employing the requirement of continuity of radial stress σ_r from zone to zone. Thus, we have

$$R_1 = \left[\frac{\sigma_{u1} + p_1(N_1 - 1)}{\sigma_{u1} + P_i(N_1 - 1)}\right]^{\frac{1}{N_1 - 1}} a$$

$$R_2 = \left[\frac{\sigma_{u2} + p_2(N_2 - 1)}{\sigma_{u2} + p_1(N_2 - 1)}\right]^{\frac{1}{N_2 - 1}} R_1$$

$$R_m = \left[\frac{\sigma_{um} + P_R(N_m - 1)}{\sigma_{um} + p_{m-1}(N_m - 1)}\right]^{\frac{1}{N_m - 1}} R_{m-1} \qquad \text{(A-21)}$$

where P_R is the interface pressure at the elastic-plastic interface.

A.3.2 Elastic Region

The stresses in the elastic region are the same as those around a cylindrical cavity with radius R_m in an elastic body with free field pressure P_o and internal pressure P_R. The stresses given in [6] for this case are

$$\sigma_r = -(P_o - P_R)\frac{R_m^2}{r^2} + P_o$$

$$\sigma_\theta = (P_o - P_R)\frac{R_m^2}{r^2} + P_o \quad . \tag{A-22}$$

We may find P_R by making use of the fact that the stresses must satisfy the yield condition

$$f = f_m = \sigma_\theta - N_m \sigma_r - \sigma_{um} = 0 \tag{A-23}$$

at $r = R_m$. This leads to the following expression for P_R:

$$P_R = \frac{(2P_o - \sigma_{um})}{1 + N_m} \quad . \tag{A-24}$$

A.4 Calculation of Strains and Displacement

We will now derive expressions for the strains and displacement in the elastic and plastic regions. For the elastic region, this is done very easily by combining Eqs. (A-5), (A-11), and (A-22). Obtaining strains and displacement in the plastic region requires further analysis. We will first consider zone m ($R_{m-1} < r < R_m$) which borders the elastic region. The associated flow rule gives the plastic strain rates as

$$\dot{\epsilon}_{rp} = \dot{\lambda}\,\frac{\partial f_m}{\partial \sigma_r} = -\dot{\lambda}\,N_m$$

$$\dot{\epsilon}_{\theta p} = \dot{\lambda}\,\frac{\partial f_m}{\partial \sigma_\theta} = \dot{\lambda}$$

$$\dot{\epsilon}_{zp} = \dot{\lambda}\,\frac{\partial f_m}{\partial \sigma_z} = 0 \quad . \tag{A-25}$$

We assume that the internal and free field pressures are applied in such a way that we have proportional loading, so that the preceding expressions may be integrated to give

$$\epsilon_{rp} = -N_m\,\epsilon_{\theta p} \quad . \tag{A-26}$$

We note that this relation implies dilatant behavior under plastic flow, a phenomenon common to granular materials [7]. We will present the results of our analysis without dilatancy later in this section.

From Eqs. (A-11), (A-20), and (A-26), we may write the strains in zone m as

$$\epsilon_r = \frac{1}{E'}\left[\frac{(1-\nu')}{1-N_m}\,\sigma_{um} + (1-\nu' N_m)\left(\frac{\sigma_{um}}{N_m-1} + p_{m-1}\right)\left(\frac{r}{R_{m-1}}\right)^{N_m-1}\right] - N_m\epsilon_{\theta p}$$

$$\epsilon_\theta = \frac{1}{E'}\left[\frac{(1-\nu')}{1-N_m}\,\sigma_{um} + (N_m-\nu')\left(\frac{\sigma_{um}}{N_m-1} + p_{m-1}\right)\left(\frac{r}{R_{m-1}}\right)^{N_m-1}\right] + \epsilon_{\theta p} \tag{A-27}$$

where $\epsilon_{\theta p}$ remains to be determined. To accomplish this, we substitute these expressions into the compatibility equation (A-6) and obtain the following differential equation for $\epsilon_{\theta p}$:

$$r\frac{d\epsilon_{\theta p}}{dr} + (1 + N_m)\ \epsilon_{\theta p} = -\frac{\left(N_m^2 - 1\right)}{E'}\left(\frac{\sigma_{um}}{N_m - 1} + p_{m-1}\right)\left(\frac{r}{R_{m-1}}\right)^{N_m-1} \qquad \text{(A-28)}$$

which has the solution

$$\epsilon_{\theta p} = -\frac{\left(N_m^2 - 1\right)}{2N_m E'}\left(\frac{\sigma_{um}}{N_m - 1} + p_{m-1}\right)\left(\frac{r}{R_{m-1}}\right)^{N_m-1} + Br^{-N_m-1} \qquad \text{(A-29)}$$

where B is an unknown constant. To find B, we use the condition that the plastic strain must vanish at the elastic-plastic boundary, i.e.,

$$\epsilon_{\theta p} = 0 \quad \text{at } r = R_m \quad . \qquad \text{(A-30)}$$

Consequently,

$$B = \frac{\left(N_m^2 - 1\right)}{2N_m E'}\left(\frac{\sigma_{um}}{N_m - 1} + p_{m-1}\right)\left(\frac{R_m}{R_{m-1}}\right)^{N_m-1} R_m^{N_m+1} \quad . \qquad \text{(A-31)}$$

The strains and displacement in zone m may now be expressed as

$$\epsilon_r = \frac{1}{E'}\left\{\frac{(1 - \nu')}{1 - N_m}\sigma_{um} + \left[1 - \nu' N_m + \frac{1}{2}\left(N_m^2 - 1\right)\right]\left(\frac{\sigma_{um}}{N_m - 1} + p_{m-1}\right)\left(\frac{r}{R_{m-1}}\right)^{N_m-1}\right\}$$
$$- \frac{\left(N_m^2 - 1\right)}{2E'}\left(\frac{\sigma_{um}}{N_m - 1} + p_{m-1}\right)\left(\frac{R_m}{R_{m-1}}\right)^{N_m-1}\left(\frac{R_m}{r}\right)^{N_m+1} \qquad \text{(A-32)}$$

$$\epsilon_\theta = \frac{1}{E'}\left\{\frac{(1 - \nu')}{1 - N_m}\sigma_{um} - \left[\frac{\left(N_m^2 - 1\right)}{2N_m} - N_m + \nu'\right]\left(\frac{\sigma_{um}}{N_m - 1} + p_{m-1}\right)\left(\frac{r}{R_{m-1}}\right)^{N_m-1}\right\}$$
$$+ \frac{\left(N_m^2 - 1\right)}{2N_m E'}\left(\frac{\sigma_{um}}{N_m - 1} + p_{m-1}\right)\left(\frac{R_m}{R_{m-1}}\right)^{N_m-1}\left(\frac{R_m}{r}\right)^{N_m+1} \qquad \text{(A-33)}$$

$$u = r\epsilon_\theta \quad . \qquad \text{(A-34)}$$

We may proceed in a similar manner to obtain the strains and displacements in the other zones within the plastic region where the continuity of displacement requirement is used to determine the integration constants. Our primary interest is the closure of the cavity. This is found to be given as

$$
\begin{aligned}
\frac{u}{a} = \frac{1}{E'}\Bigg[& \frac{(1-\nu')}{1-N_1}\,\sigma_{u1} + (N_1-\nu')\left(\frac{\sigma_{u1}}{N_1-1} + P_i\right) \\
& + \frac{\left(N_1^2-1\right)}{2E'N_1}\left(\frac{\sigma_{u1}}{N_1-1} + P_i\right)\left[\left(\frac{R_1}{a}\right)^{2N_1} - 1\right] \\
& + \frac{\left(N_2^2-1\right)}{2E'N_2}\left(\frac{\sigma_{u2}}{N_2-1} + p_1\right)\left[\left(\frac{R_2}{R_1}\right)^{2N_2} - 1\right]\left(\frac{R_1}{a}\right)^{N_1+1} \\
& + \frac{\left(N_3^2-1\right)}{2E'N_3}\left(\frac{\sigma_{u3}}{N_3-1} + p_2\right)\left[\left(\frac{R_3}{R_2}\right)^{2N_3} - 1\right]\left(\frac{R_2}{R_1}\right)^{N_2+1}\left(\frac{R_1}{a}\right)^{N_1+1} \\
& + \dots . \\
& + \frac{\left(N_m^2-1\right)}{2E'N_m}\left(\frac{\sigma_{um}}{N_m-1} + p_{m-1}\right)\left[\left(\frac{R_m}{R_{m-1}}\right)^{2N_m} - 1\right]\left(\frac{R_{m-1}}{R_{m-2}}\right)^{N_{m-1}+1}\left(\frac{R_{m-2}}{R_{m-3}}\right)^{N_{m-2}+1}\cdots\left(\frac{R_1}{a}\right)^{N_1+1} .
\end{aligned}
\tag{A-35}
$$

A.5 Closure Without Dilatancy

We may eliminate dilatancy from the above analysis by using a "non-associated" flow rule whereby the material is considered to be incompressible under plastic flow; i.e.,

$$\varepsilon_{rp} + \varepsilon_{\theta p} = 0 \quad . \tag{A-36}$$

In this case, the closure of the cavity is given as

$$\begin{aligned}
\frac{u}{a} = {} & \frac{1}{E'}\left[\frac{(1 - \nu')}{1 - N_1}\,\sigma_{u1} + (N_1 - \nu')\left(\frac{\sigma_{u1}}{N_1 - 1} + P_i\right)\right] \\
& + \frac{1}{E'}\left[\sigma_{u1} + (N_1 - 1)\,P_i\right]\left[\left(\frac{R_1}{a}\right)^{N_1+1} - 1\right] \\
& + \frac{1}{E'}\left[\sigma_{u2} + (N_2 - 1)\,p_1\right]\left[\left(\frac{R_2}{R_1}\right)^{N_2+1} - 1\right]\left(\frac{R_1}{a}\right)^2 \\
& + \frac{1}{E'}\left[\sigma_{u3} + (N_3 - 1)\,p_2\right]\left[\left(\frac{R_3}{R_2}\right)^{N_3+1} - 1\right]\left(\frac{R_2}{a}\right)^2 \\
& + \ldots. \\
& + \frac{1}{E'}\left[\sigma_{um} + (N_m - 1)\,p_m\right]\left[\left(\frac{R_m}{R_{m-1}}\right)^{N_m+1} - 1\right]\left(\frac{R_{m-1}}{a}\right)^2 \quad .
\end{aligned} \tag{A-37}$$

A.6 Tunnel Closure in Tuff

We will now study the closure of a tunnel in rock with a failure envelope in the range of those found for tuff in the Might Epic area. The yield envelope for this rock, taken from Terra Tek data [8], is shown in Figure A.4. We performed calculations using the solid line nonlinear curve, which follows the yield data closely, and the dashed single straight line approximation. A plot of tunnel closure versus free field pressure for the analysis with dilatancy and $P_i = 0$ is shown

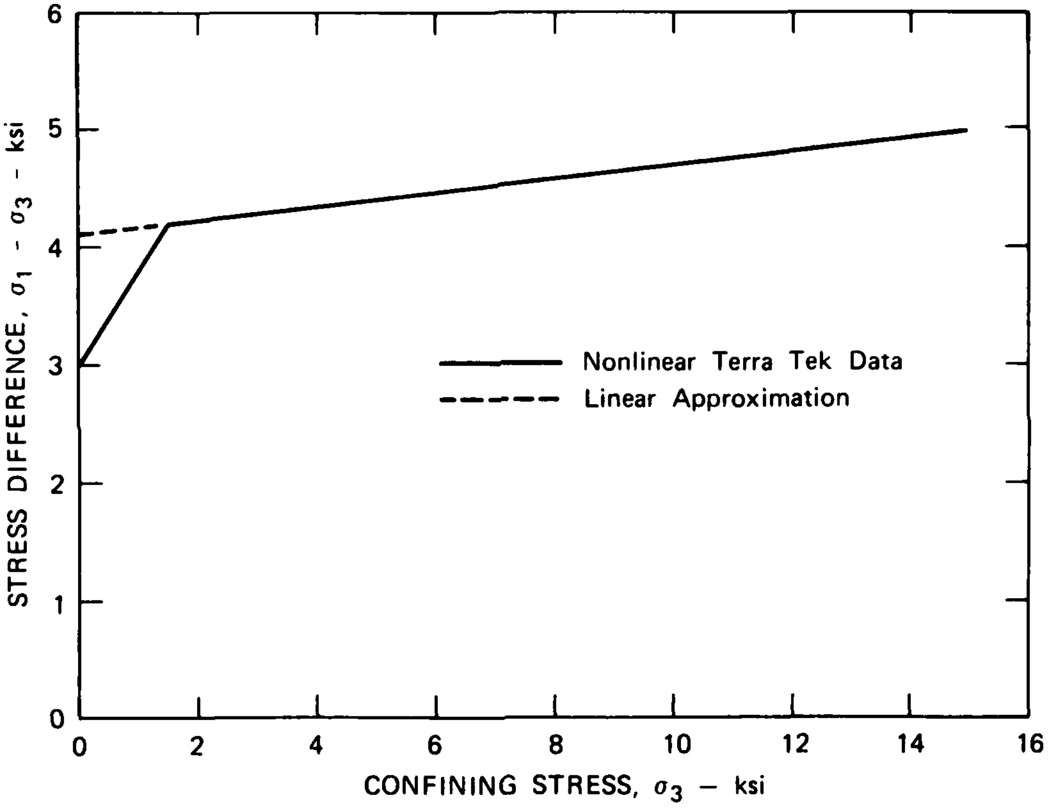

MA-4121-54A

FIGURE A.4 YIELD ENVELOPE FOR TUFF IN MIGHTY EPIC AREA in Figure A.5 for these two cases. The difference in tunnel closure for a given load for the two curves can be quite large. For example, at P_o equal to 7500 psi, there is 50 percent more closure in the nonlinear envelope case than in the linear envelope case even though the two yield envelopes are identical except when σ_3 is less than 1500 psi. This suggests that the amount of closure is very sensitive to the plastic behavior of the material closest to the cavity (i.e., where σ_3 is smallest).

Figure A.6 shows a similar calculation using the analysis without dilatancy. The choice of yield envelope has a much smaller effect here (at P_o equal to 7500 psi, there is only about 10 percent more closure in the nonlinear envelope case than in the linear envelope case). This is expected since the plastic strain rate vectors have the same direction for both envelopes; i.e., "normality" is not required.

Let us now consider a weak tuff whose yield envelope is shown in Figure A.7. The solid line nonlinear curve closely fits data from Terra Tek [8]. Two single straight line approximations to this envelope are also shown. Figures A.8 through A.12 give plots of tunnel closure versus free field pressure with different internal pressures for these three envelopes using the theory with dilatancy.

In Figure A.8, for which P_i equals zero, we see that the closures for the nonlinear yield envelope and linear approximation #1 are fairly close, while the closure for linear approximation #2 is considerably smaller for a given load. Linear approximation #1 is closer to the nonlinear envelope at low stress levels ($0 < \sigma_3 < 1000$ psi) than approximation #2. This again demonstrates the sensitivity of closure to the plastic behavior of the material in close proximity to the tunnel.

Figure A.9 shows similar plots for P_i equal to 1 ksi. Now the closures for the nonlinear envelope and approximation #2 are close together while closure for approximation #1 is higher than either. This

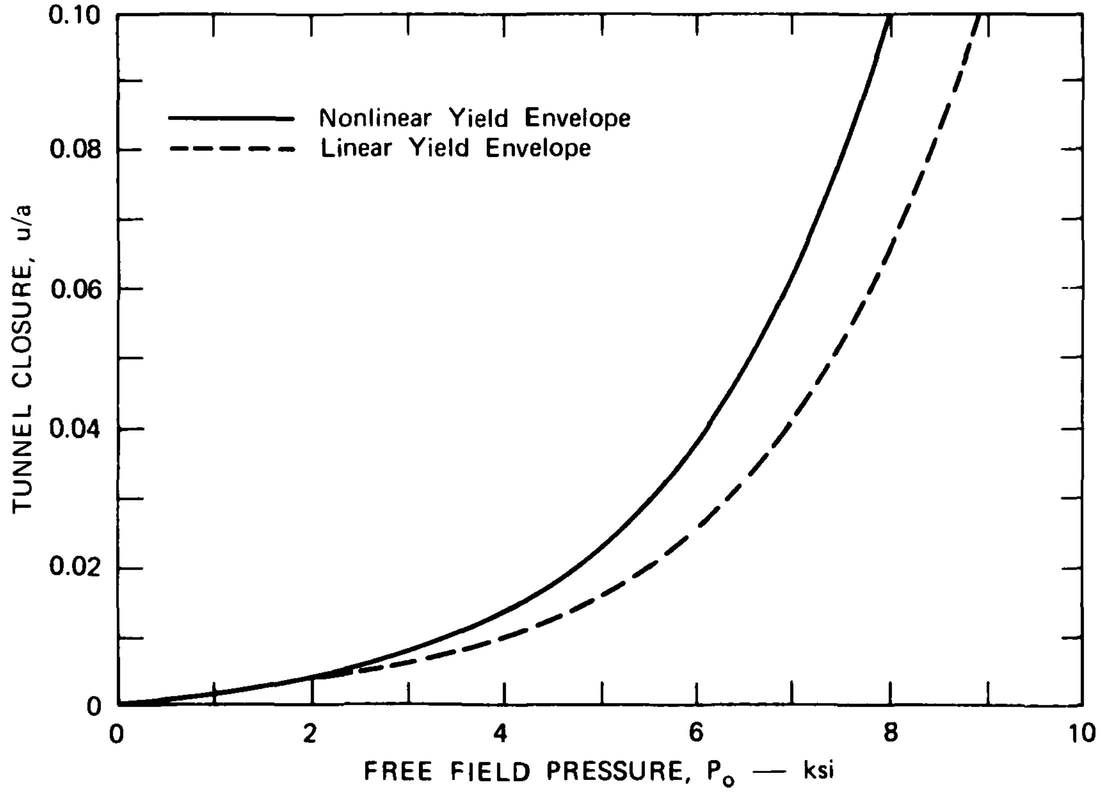

MA-4121-55

FIGURE A.5 TUNNEL CLOSURE VERSUS FREE FIELD PRESSURE (WITH CAVITY PRESSURE P_i = 0) FOR ANALYSIS WITH DILATANCY

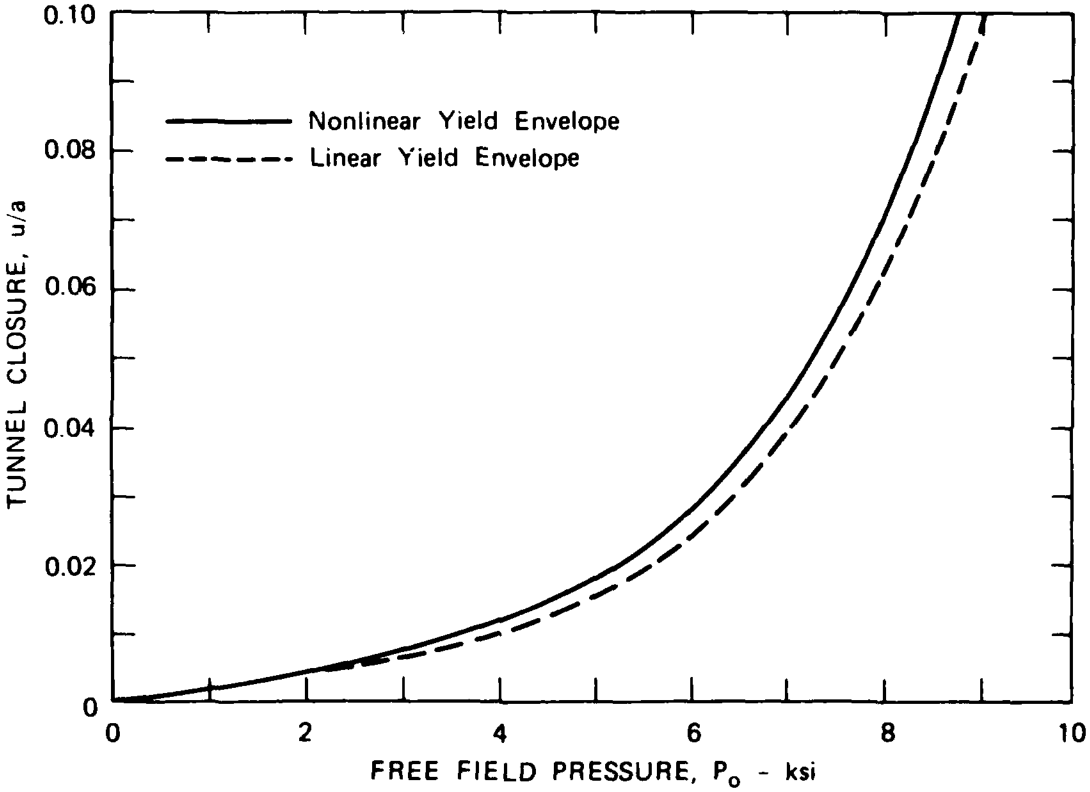

MA-4121-56

FIGURE A.6 TUNNEL CLOSURE VERSUS FREE FIELD PRESSURE (WITH CAVITY PRESSURE P_i = 0) FOR ANALYSIS WITHOUT DILATANCY

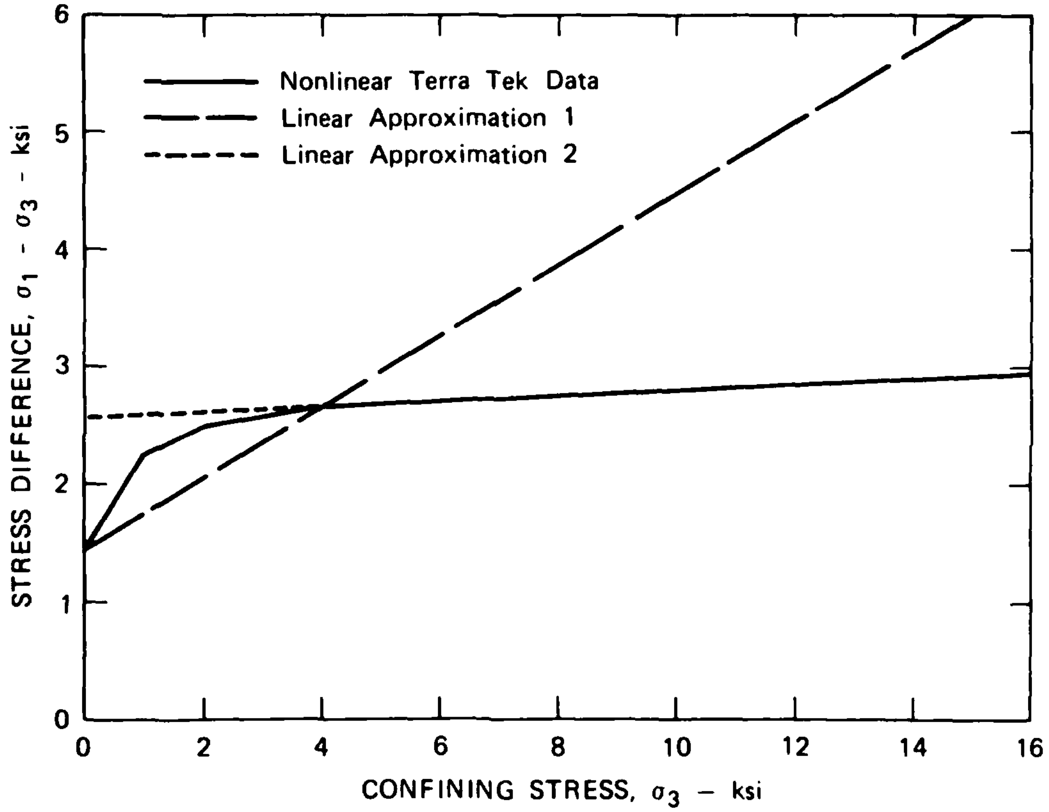

MA-4121-57A

FIGURE A.7 YIELD ENVELOPE FOR WEAK TUFF

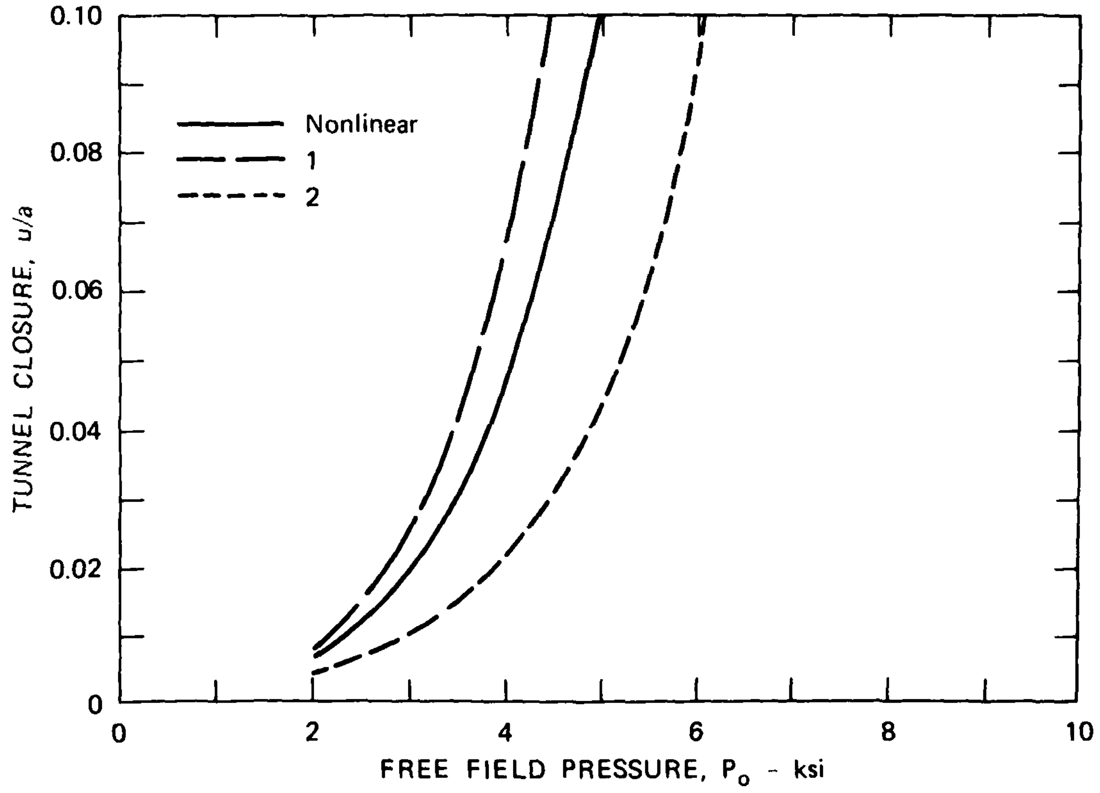

MA-4121-58

FIGURE A.8 TUNNEL CLOSURE VERSUS FREE FIELD PRESSURE (WITH CAVITY PRESSURE P_i = 0) IN WEAK TUFF WITH DILATANCY

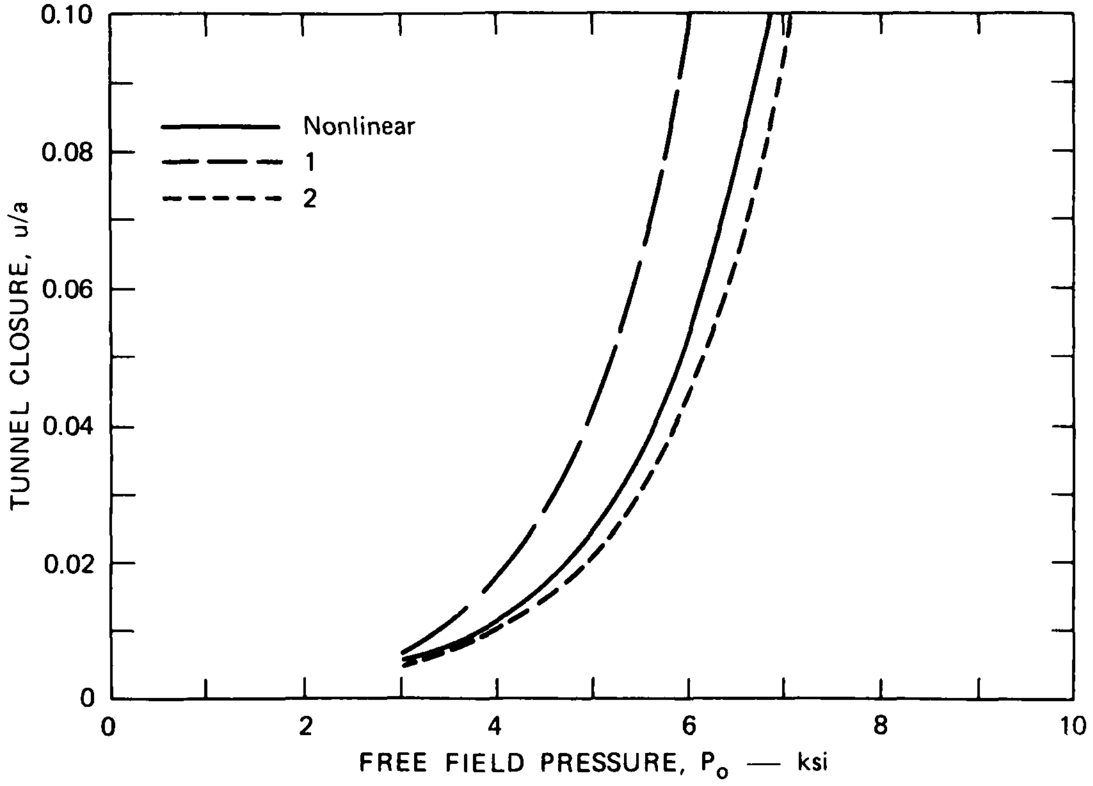

FIGURE A.9 TUNNEL CLOSURE VERSUS FREE FIELD PRESSURE (WITH CAVITY PRESSURE P_i = 1 ksi) IN WEAK TUFF WITH DILATANCY

is expected because approximation #2 is closer to the nonlinear envelope than approximation #1 for σ_3 greater than 1 ksi. As P_i is increased further, all three closure curves shift further to the right (see Figures A.10, A.11, and A.12) with the closure for the nonlinear curve and approximation #2 becoming coincident at $P_i = 4$ ksi (Figure A.12). The closure curve for approximation #1 moves to the right more rapidly than the others with increasing P_i, and eventually passes them at $P_i = 3$ ksi (Figure A.11). Again, these results demonstrate the importance of accurately modeling the yield envelope in the low σ_3 stress level region near the tunnel.

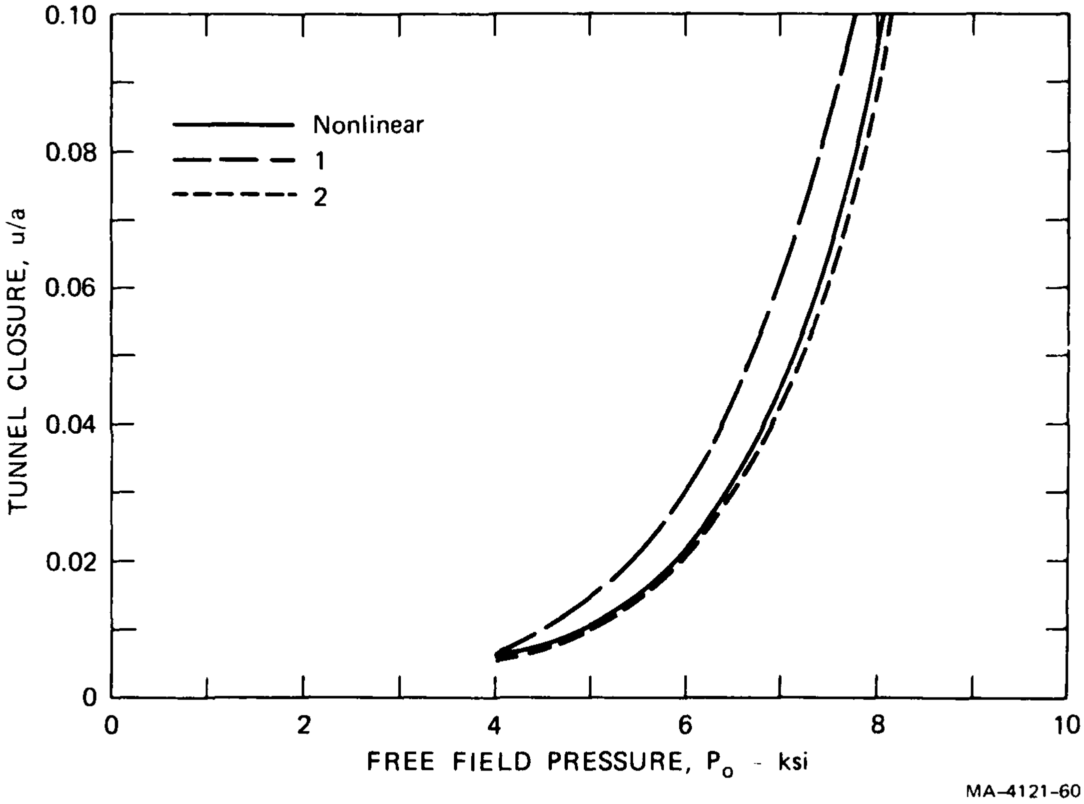

FIGURE A.10 TUNNEL CLOSURE VERSUS FREE FIELD PRESSURE (WITH CAVITY PRESSURE P_i = 2 ksi) IN WEAK TUFF WITH DILATANCY

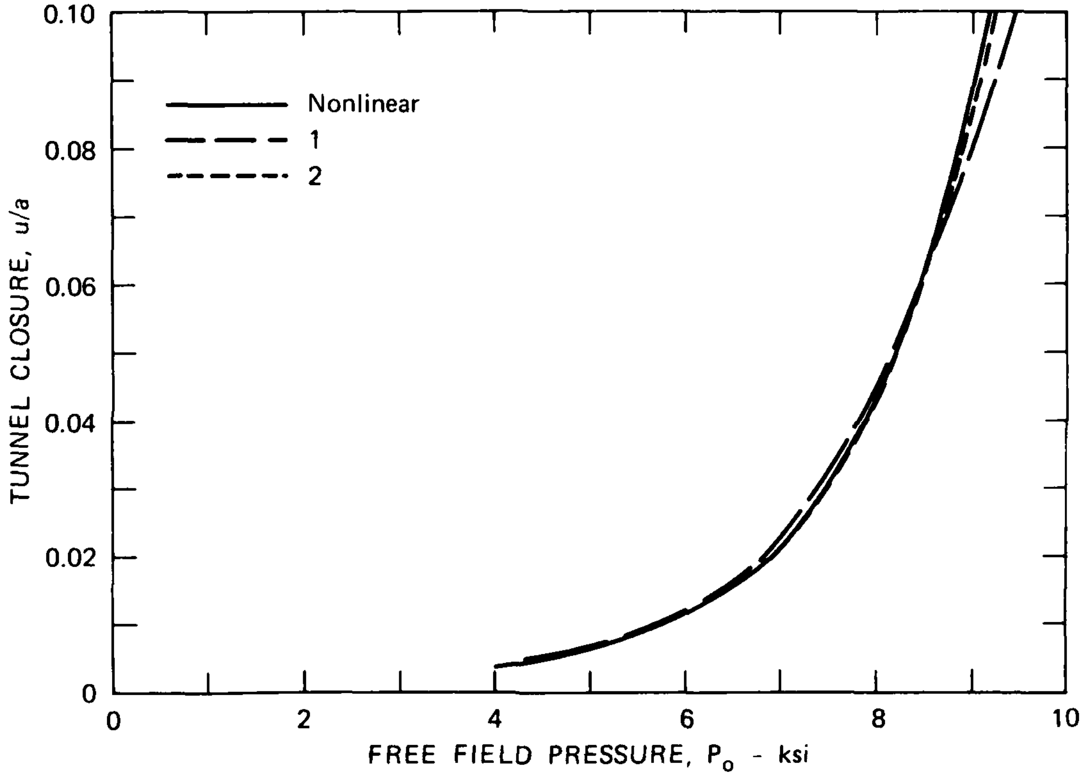

MA-4121-61

FIGURE A.11 TUNNEL CLOSURE VERSUS FREE FIELD PRESSURE (WITH CAVITY PRESSURE P_i = 3 ksi) IN WEAK TUFF WITH DILATANCY

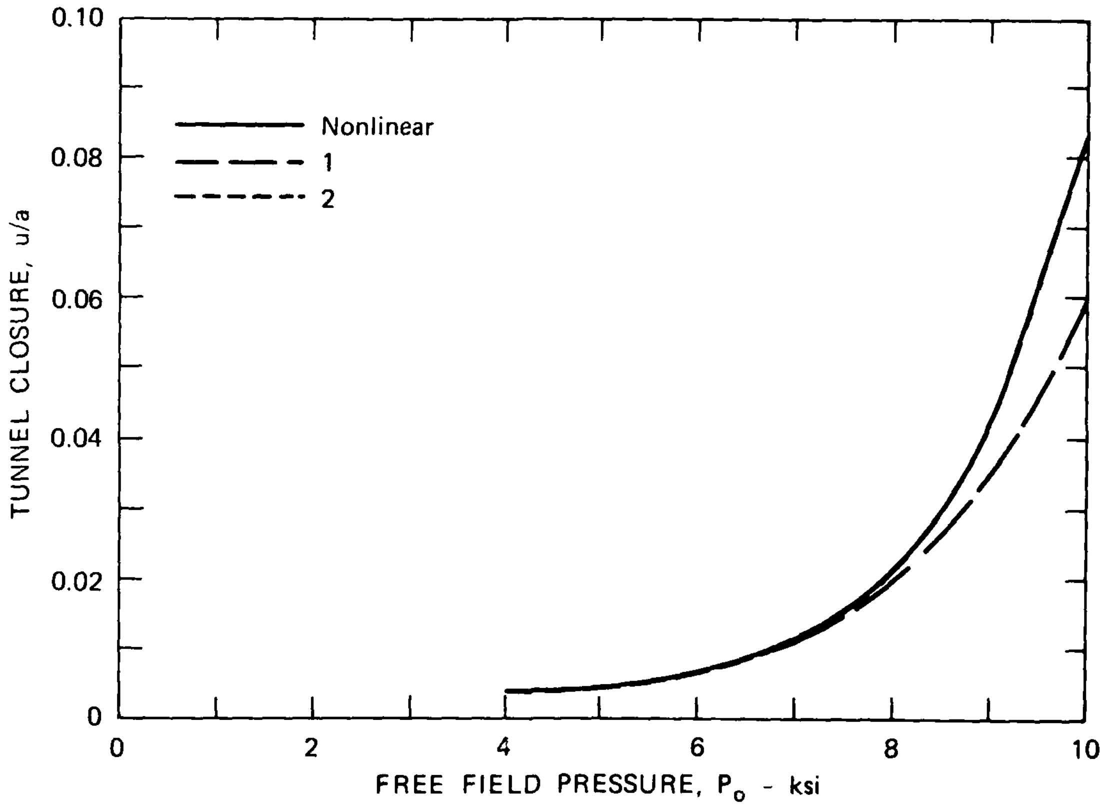

MA-4121-62

FIGURE A.12 TUNNEL CLOSURE VERSUS FREE FIELD PRESSURE (WITH CAVITY PRESSURE P_i = 4 ksi) IN WEAK TUFF WITH DILATANCY

Appendix B

MAPPING OF A SEGMENTED YIELD SURFACE INTO A MOHR DIAGRAM

In this appendix, we investigate the relationship between the yield criterion given in $\sigma_1 - \sigma_3$ versus σ_3 space used in our analysis and the usual Mohr-Coulomb criterion given in τ (shear stress) versus σ_n (normal stress) space. For simplicity, we consider the bilinear yield envelope shown in Figure B.1(a), where

$$\text{for } \sigma_3 \leq p_1 , \; f = f_1 = \sigma_1 - (1 + \tan \omega_1) \sigma_3 - \sigma_{u1} = 0 \qquad \text{(B-1)}$$

$$\text{for } \sigma_3 \geq p_1 , \; f = f_2 = \sigma_1 - (1 + \tan \omega_2) \sigma_3 - \sigma_{u2} = 0 \quad . \qquad \text{(B-2)}$$

In τ versus σ_n space, yielding occurs when the Mohr circle representing the state of stress at some point in the body comes in contact with the yield envelope; for example, consider the first circle tangent to the line

$$F = F_1 = \tau - \tan \phi_1 \sigma_n - C_1 = 0 \qquad \text{(B-3)}$$

in Figure B.1(b), where ϕ_1 is the angle of internal friction for that part of the yield envelope. The maximum and minimum principal stresses at yield are σ_1 and σ_3, respectively. For this line, τ and σ_n are related to σ_1 and σ_3 by

$$\tau = \left(\frac{\sigma_1 - \sigma_3}{2}\right) \cos \phi_1 \qquad \text{(B-4)}$$

$$\sigma_n = \sigma_3 + (1 - \sin \phi_1) \left(\frac{\sigma_1 - \sigma_3}{2}\right) \quad . \qquad \text{(B-5)}$$

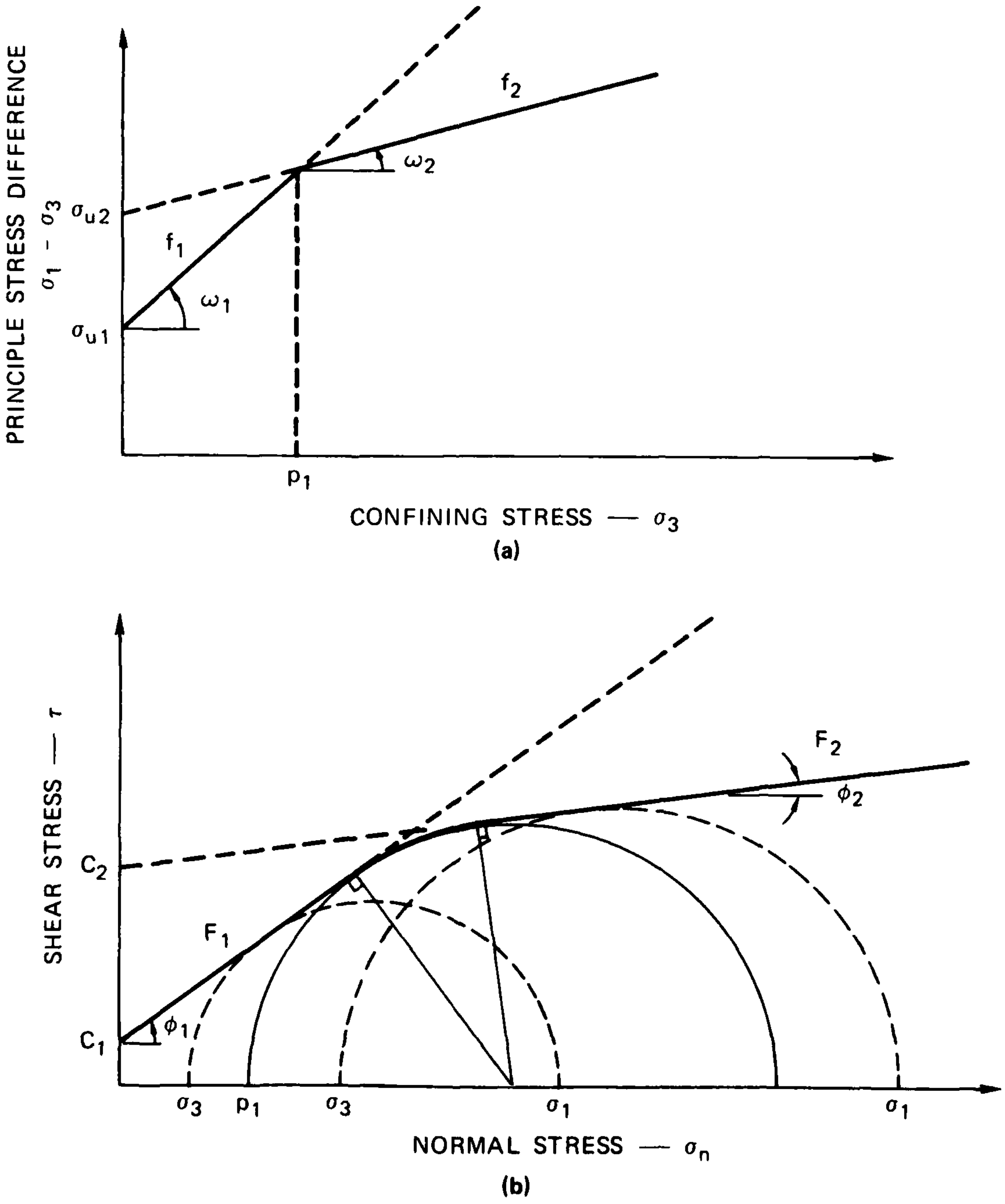

FIGURE B.1 RELATIONSHIP BETWEEN THE YIELD ENVELOPES IN $\sigma_1 - \sigma_3$ VERSUS σ_3 SPACE AND τ VERSUS σ_n SPACE

Substituting these expressions into Eq. (B-3) yields

$$F_1 = \sigma_1 - \left(\frac{1 + \sin \phi_1}{1 - \sin \phi_1}\right) \sigma_3 - C_1 = 0 \quad . \tag{B-6}$$

Comparing this result with Eq. (B-1), we conclude that for these two yield envelopes to be equivalent, the following relations must hold:

$$\phi_1 = \sin^{-1} \left[\frac{\tan \alpha_1}{2 + \tan \alpha_1}\right] \tag{B-7}$$

$$C_1 = \frac{(1 - \sin \phi_1)}{2 \cos \phi_1} \sigma_{u1} \quad . \tag{B-8}$$

Similar relations hold for the other line segments of the yield envelope. Consequently, straight line segments in $\sigma_1 - \sigma_3$ versus σ_3 space map into straight line segments in τ versus σ_n space as shown in Figure B.1(b). When the minimum principal stress σ_3 is less than p_1, the Mohr circle representing the state of stress at yield is tangent to the line F_1. When σ_3 is greater than p_1, the Mohr circle at yield is tangent to the line F_2. When σ_3 is equal to p_1, the Mohr circle is tangent to both line F_1 and line F_2. This means that the point connecting f_1 and f_2 at σ_3 equal to p_1 in $\sigma_1 - \sigma_3$ versus σ_3 space is mapped into an arc of a circle tangent to F_1 and F_2 in τ versus σ_n space. Consequently, there are no "corners" on the yield envelope in τ versus σ_n space.

Blank

Appendix C

IMPROVEMENTS IN THE VERTICAL AND LATERAL PRESSURE PULSES

Pressure records obtained from the initial tests performed with the larger scale testing machine developed under this program and also from earlier tests performed with the small scale testing machine showed that the loading pressure pulses were not smooth, but had large-amplitude spikes and oscillations. The nature of the oscillations in pressure can be seen from the pressure records shown in Figure C.1. These pressure records are from an early dynamic uniaxial strain loading experiment, DCUX-68. Similar records were obtained from the initial tests performed with the larger scale testing machine.

Figure C.1(a) shows the vertical pressure in the gas above the specimen.* The pressure pulse has the desired shape and smooth rise. This loading, applied at the top of the specimen, is reacted by the pool of oil in the receiver plate under the specimen. The pressure in this oil under the specimen is shown in Figure C.1(b). Although the pressure pulse has the same general shape as the pressure pulse in the gas above the specimen, it has some undesirable spikes and high frequency oscillations (5100 Hz) as early times. The amplitudes of several of these spikes are as great or greater than the peak of the pulse. The cause of the spikes and subsequent oscillations in the pressure in the oil under the specimen appeared to be the specimen impacting this pool of oil. We took corrective steps based on this assumption and were successful in eliminating the spikes and reducing the amplitude of the oscillations in pressure. These steps will be described below. It is important to note that pressure measurements by means of the oil pool were crucial in detecting this problem; specimen impact may go undetected in other dynamic loading machines.

---

*See Figure 3.1, page 41 for a cross-sectional view of the testing machine.

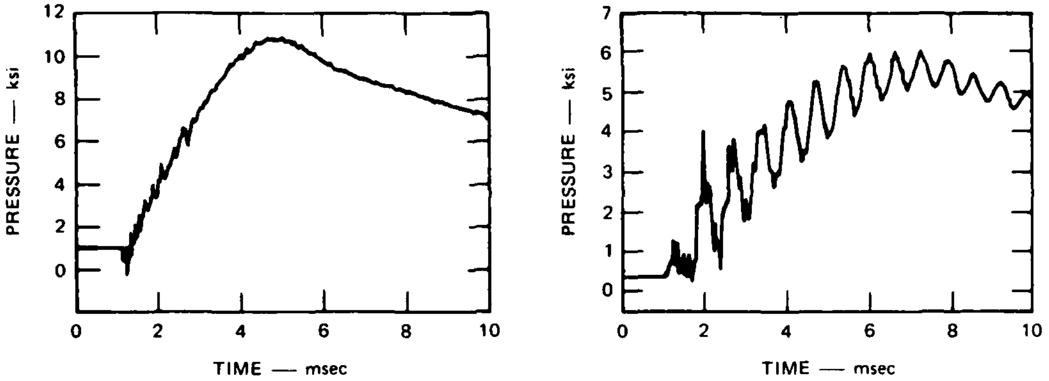

(a) P1-GAS PRESSURE ABOVE SPECIMEN

(c) P2-OIL PRESSURE IN LATERAL CHAMBER (NEAR CENTER)

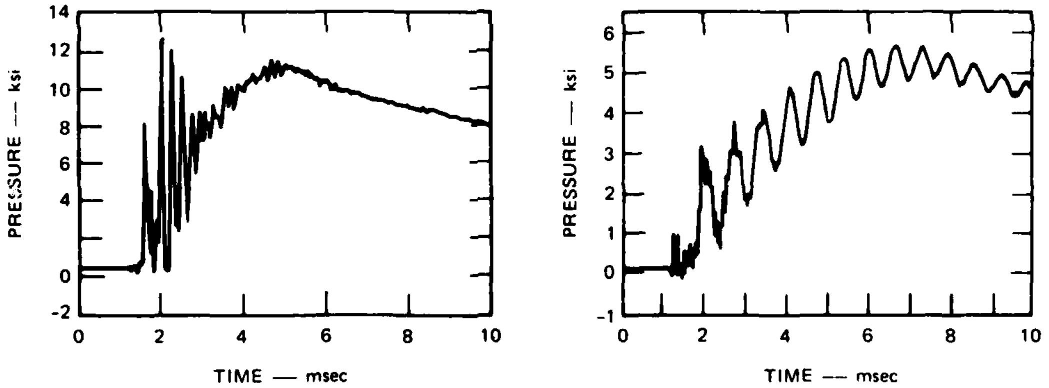

(b) P4-OIL PRESSURE BELOW SPECIMEN

(d) P3-OIL PRESSURE IN LATERAL CHAMBER (SLIGHTLY LOWER)

MA-4121-76

FIGURE C.1 PRESSURE DATA FROM TEST DCUX-68, BEFORE REDUCING THE SOURCE OF PRESSURE OSCILLATIONS

Figures C.1(c) and C.1(d) show the lateral confining pressure, measured at two separate locations in the lateral chamber. The low frequency (1550 Hz) oscillation in pressure has an amplitude that abates to 8 percent of the amplitude of the peak pressure at the time the peak occurs. The frequency is very close to the fundamental frequency calculated for vibration of the oil in the lateral chamber (the Bellofram at the base of the chamber acts as a free boundary, so the oil is modeled as a column that is fixed at the top and free at the bottom). For the larger scale testing machine, the frequency of the oscillations (680 Hz) also corresponded to the calculated fundamental frequency of the oil in the lateral chamber. The source of these oscillations was not clear. Therefore, several paths were explored before the oscillations were reduced to an acceptable level. These corrective measures will be outlined in the last section of this appendix.

The improved pressure pulses are shown in Figure C.2. These pressure records are from a typical dynamic uniaxial strain loading experiment, DUX-74. Figures C.2(a) and C.2(b) show the vertical pressure in the gas above the specimen and in the oil under the specimen, respectively. The large spikes in the pressure record shown in Figure C.1(b) are absent from the record shown in Figure C.2(b). A vestige remains, but it is at a low level and is greatly separated in time from the peak loading, where virtually all the tunnel response takes place. The pressure increases abruptly at the beginning of the pulse, but then rises fairly steadily to the peak of the pulse. The lateral pressure data shown in Figures C.2(c) and C.2(d) indicate that the oscillation in the lateral pressure damps out rapidly and that the frequency is only half that of the oscillation in the lateral pressure in test DCUX-68. In later tests these small lateral chamber oscillations were reduced still further until they were barely detectable, Figure C.3.

C.1 VERTICAL PRESSURE PULSE IMPROVEMENT

The spikes and subsequent oscillations in the vertical pressure measured in the oil under the specimen apparently result from inevitable

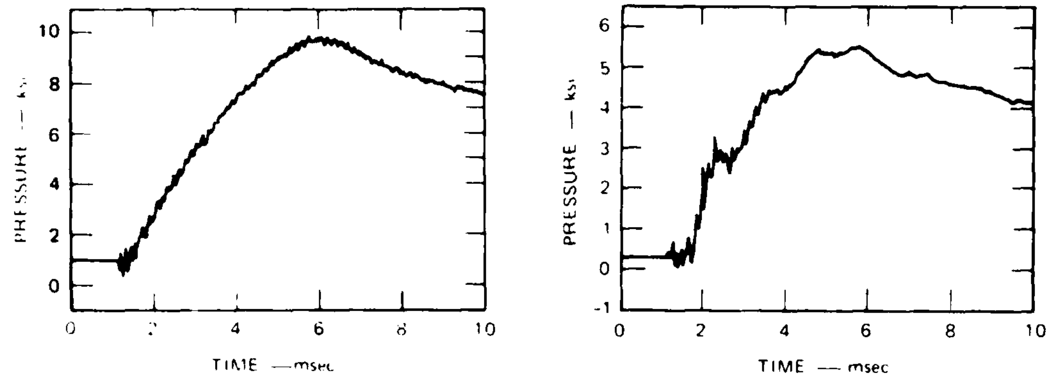

(a) P1-GAS PRESSURE ABOVE SPECIMEN

(c) P2-OIL PRESSURE IN LATERAL CHAMBER (NEAR CENTER)

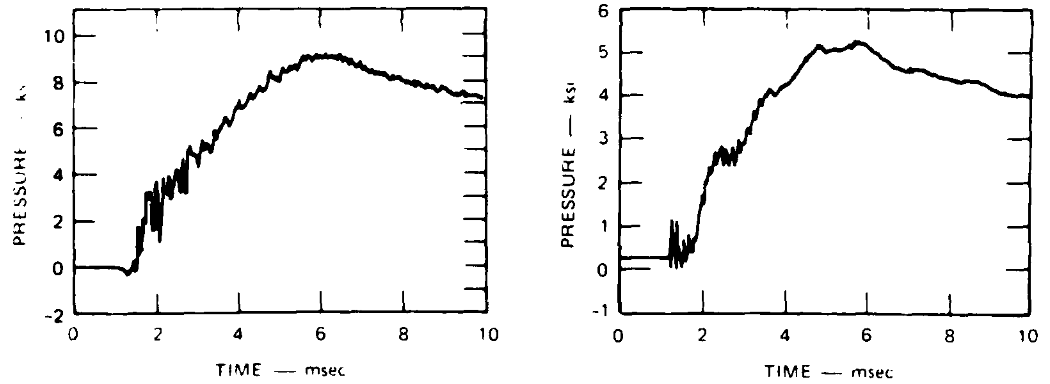

(b) P4-OIL PRESSURE BELOW SPECIMEN

(d) P3-OIL PRESSURE IN LATERAL CHAMBER (SLIGHTLY LOWER)

MA 4121 75

FIGURE C.2 PRESSURE DATA FROM UNIAXIAL STRAIN LOADING TEST DUX-74

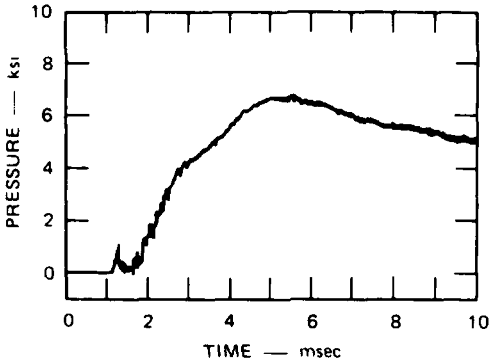

(a) P2-OIL PRESSURE IN LATERAL CHAMBER (NEAR CENTER)

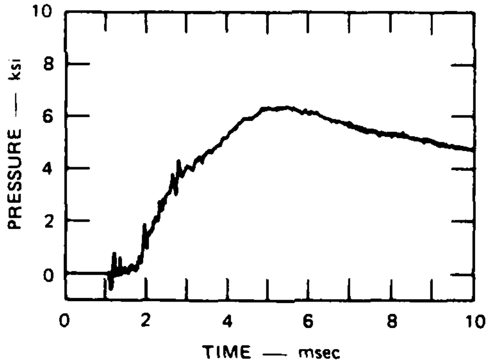

(b) P3-OIL PRESSURE IN LATERAL CHAMBER (SLIGHTLY LOWER)

MA-4121-158

FIGURE C.3 LATERAL PRESSURE DATA FROM TEST DUX-84, SHOWING CURRENT LATERAL PRESSURE PULSES rock misalignment and also entrapment of a small amount of air in the oil well below the rock. Calculations indicate that a gap between rock and support of only a few mils is enough that the rock impacts the support at a velocity high enough to give the observed spike amplitude. Then the rock rebounds, impacts again, and so forth until the process gradually damps out. In an attempt to reduce the amplitude of the spikes, a dissipative mechanism was introduced between the rock specimen and the oil under the specimen.

A layer of 0.100-inch- (2.5-mm) diameter lead shot was placed in the bottom copper can, under the specimen. The lead shot was packed in the bottom of the copper cup to a density that was approximately 95% of the tightest possible packing. After the test, the lead shot was remeasured and was found to have been permanently crushed by roughly 30%. The records resulting from this test showed that the lead shot was fairly effective in reducing the severity of the impact and that the plastic deformation of the lead shot did introduce some damping.

On the basis of static experiments performed on various packing densities of the lead shot, we felt that a much lower packing density, approximately 50%, would significantly reduce the severity of the impact. This would also provide enough dissipation to reduce the height to which the rock rebounded, thereby reducing the magnitude of the subsequent spikes. Because this lower density of lead shot supports the specimen at fewer, more widely spaced points, we placed a 0.010-inch- (0.25-mm) thick steel plate between the specimen and the layer of lead shot to maintain a nearly uniform load on the rock.

Results from tests with 50% packing density showed that the amplitude of the initial spike was reduced but that the subsequent oscillations persisted. The greater compliance of the 50% packing provided more cushioning, but not enough to also damp out the oscillations. To obtain small oscillations that damp out quickly, we reviewed the source of the oscillation and made another change in our testing procedure as described below.

As stated previously, we attributed the spikes in the vertical pressure to the specimen impacting against the oil pool in the reaction chamber below the rock. We suspected that a small amount of air was trapped in the chamber and that this trapped air compressed while the rock was being accelerated downward by the loading gas pressure above the rock. When the air was completely compressed, the rock impacted the oil and rebounded up from it. The gas pressure above the rock then accelerated the specimen back downward toward the oil where it again impacted and rebounded. This process damped out quickly, but without special precautions, the amplitude of the first few spikes in the pressure pulse could be unacceptably high.

We found that the amount of air trapped in the chamber could be reduced by heating the oil before and during the fill procedure. The receiver plate (the plate that contains the oil chamber) was placed on its side and oriented so that the gage port was at the top. The copper cup and O-ring that seal the oil chamber were put in place, and the oil was slowly poured into the chamber through the gage port. During this period the plate was heated by four infrared lamps. When the chamber was full, the copper cup was flexed so that the oil level rose and fell in the gage port. The induced motion of the oil allowed tiny air bubbles to float to the top of the chamber and out through the gage port. When no more air could be forced to float out, the pressure gage was installed, sealing the gage port, and the ring was stacked into the machine where it was allowed to cool.

We feel that heating the oil reduces its viscosity and allows smaller air bubbles to escape. Results from tests in which this fill procedure was used in conjunction with the layer of 50% packing density lead shot showed that the initial spike was nearly eliminated and the remaining small oscillation damped out quickly. The oil pressure then increased smoothly as it faithfully reproduced the applied air pressure at the top of the rock. The small initial oscillations probably indicate some inevitable rock misalignment or that a small amount of air remained trapped inside the chamber.

In summary, to achieve suitable pressure pulses at the base of the specimen, we placed a layer of lead shot in the bottom copper cup under the specimen and used extra care in removing trapped air from the oil chamber in the receiver plate. These two steps lessen the severity of the impact of the specimen on the pool of oil below it and help produce a suitable loading pulse. This same procedure, developed here for the small testing machine, has been used successfully to achieve a completely analogous loading pulse in the larger scale testing machine.

C.2 LATERAL PRESSURE PULSE IMPROVEMENT

As mentioned previously, the source of the oscillations in the lateral pressure was unknown, so several paths were investigated. Since the frequency of the oscillations in both the small and larger scale testing machines corresponded to the fundamental frequency of the oil column with one end free and the other fixed, whose length is that of the lateral chamber, we made some simple calculations with both a single-degree-of-freedom model and a uniform column model excited by the ramp increase in explosive gas pressure at the base of the column. These calculations suggested that the amplitude of the oscillations would decrease in proportion to a decrease in the rate of pressure rise in the ramp.

To test this hypothesis, we performed a series of tests in which the rise time of the pressure pulse was increased from 1.2 to 2.4 to 5.5 ms. The respective amplitudes of the oscillation were reduced from ±15% to ±13% to ±8% (±8% is the amplitude shown in Figure C.1).

In this test series, the shape of the pressure oscillation at the gage location nearest the upper end of the rock tended to be more nearly triangular than sinusoidal, and the shape at the middle gage tended to be trapezoidal. These were the shapes predicted by the oil column model with a ramp input of pressure at its base. Also, further calculations with the oil column model showed that if the sudden linear ramp rise in pressure were replaced by a ramp with a rounded toe, the triangular shape would be replaced by a more nearly sinusoidal shape and the amplitude of the oscillation would be greatly reduced.

To investigate this prediction, we performed tests in which the baffle plate holes were constricted to produce the desired rounded toe on the pressure pulse. The results of these tests were somewhat surprising: the oscillations at early times during the pressure pulse were increased in amplitude and had a shape similar to that which would result if the single-degree-of-freedom system were subjected to a step load (in contrast to a ramp load). These results suggested that the loading applied by the Bellofram to the loading chamber was not solely responsible for the oscillations in pressure that were observed. It was expected therefore that the structural response of the testing machine following the detonation of the loading charges was, in part, responsible for these pressure oscillations.

To determine the influence of the dynamic structural response of the testing machine on the lateral pressure pulse, we performed a test in which the explosive gases were prevented from directly loading the specimen or the oil,hence any disturbance in the oil would have to be excited by pulses traveling through the rings of the testing machine. Records from this test show that the oil remained quiescent throughout the test: no pressure was transmitted to the oil when the vent holes were blocked. Therefore, we concluded that the dynamic structural response of the test apparatus was not the mechanism responsible for the excitation of the oscillations in the lateral pressure.

Finally, although we were unable to identify the source of the oscillations, we did find a way to reduce their amplitude to a very low level. We performed a test in which 6 of the 12 holes through the receiver plate were plugged. We expected that this greater change in cross-sectional area would tend to accentuate the oscillations but that the increased damping would dominate this effect at the peak of the pulse.

The records from this test showed that the net result was a decrease in the amplitude of the oscillations. Surprisingly, the initial amplitude of the oscillation was not increased.

Encouraged by this result, we performed another test in which 10 of the 12 holes through the receiver plate were plugged. The records from this test showed that the amplitude of the pressure oscillations at the peak of the pulse was very small. Also, the frequency of the oscillations was reduced to half of that observed in previous tests. This was attributed to having the oil holes now constricted to such an extent that we have changed the boundary conditions of the oil column. The important result, however, was that reducing the number of holes through the plate seemed indeed to increase the damping in the system and hence reduce the amplitude of the oscillation to a very small level, acceptable for routine testing.

Later, we opened six holes in this plate, but with reduced diameters so that the total open area was the same as for two unconstricted holes. This was done to give further assurance that the loading was circumferentially uniform near these entry holes at the base of the specimen.

Since the design and operation of both the small and large testing machines are similar, we made this modification to the specimen receiver plate in the large machine simply by plugging six holes and making the diameter of the six constricted holes three times larger than in the small testing machine. The factor three was chosen because it is the ratio of the diameter of the large specimen to the diameter of the small specimen and because it is representative of the scale factors between corresponding parts in the two testing machines. The damping introduced by the modification to the large testing machine reduced the amplitude and the frequency of the oscillations so that the resulting lateral pressure pulses are similar to those shown for the small machine in Figure C.2. Later tests with the small testing machine (performed under our current laboratory program) showed that the lateral pressure pulse shown in Figure C.2 can be improved even further, as shown in Figure C.3, by decreasing the area of the constricted holes through the specimen receiver plate. Similar modifications have been completed in the large machine, but no tests have yet been performed with this configuration at the time of of this reporting.

In summary then, although we did not locate the source of the oscillations in the lateral pressure pulse, we were able to introduce enough damping to reduce the amplitude of the oscillations to a negligible level.

Blank

DISTRIBUTION LIST

DEPARTMENT OF DEFENSE

Assistant to the Secretary of Defense
Atomic Energy
ATTN: Executive Assistant

Defense Advanced Rsch Proj Agency
ATTN: TIO

Defense Intelligence Agency
ATTN: DB-4C2
ATTN: RDS-3A

Defense Nuclear Agency
ATTN: STVL
ATTN: RAEV
3 cy ATTN: SPSS, T. Deevy
4 cy ATTN: TITL

Defense Technical Information Center
12 cy ATTN: DD

Field Command
Defense Nuclear Agency
ATTN: FCTMOF
ATTN: FCPR

Field Command
Defense Nuclear Agency
Livermore Division
ATTN: FCPRL

Field Command Test Directorate
2 cy ATTN: FCTC, J. LaComb

Joint Strat TGT Planning Staff
ATTN: JLA
ATTN: NRI-STINFO Library

Undersecretary of Def for Rsch & Engrg
ATTN: Strategic & Space Systems (OS)

DEPARTMENT OF THE ARMY

Chief of Engineers
Department of the Army
ATTN: DAEN-MCE-D
ATTN: DAEN-RDM

Construction Engineering Rsch Lab
Department of the Army
ATTN: CERL-SOI-L

Harry Diamond Laboratories
Department of the Army
ATTN: DELHD-N-P

U.S. Army Ballistic Research Labs
ATTN: DRDAR-TSB-S
ATTN: DRDAR-BLT, W. Taylor
ATTN: DRDAR-BLE, J. Keefer
ATTN: DRDAR-BLV

U.S. Army Communications Command
ATTN: Technical Reference Division

DEPARTMENT OF THE ARMY (Continued)

U.S. Army Concepts Analysis Agency
ATTN: CSSA-ADL

U.S. Army Engineer Center
ATTN: DT-LRC

U.S. Army Engineer Dist Omaha
ATTN: MROED-D, C. Distefano

U.S. Army Engineer Div Huntsville
ATTN: HNDED-SR
3 cy ATTN: C. Huang

U.S. Army Engineer Div Ohio River
ATTN: ORDAS-L

U.S. Army Engr Waterways Exper Station
ATTN: P. Mlakar
ATTN: Library
ATTN: WESSD, G. Jackson
ATTN: WESSE, L. Ingram
ATTN: J. Drake
ATTN: WESSA, W. Flathau
ATTN: WESSS, J. Ballard
ATTN: J. Day

U.S. Army Nuclear & Chemical Agency
ATTN: Library

DEPARTMENT OF THE NAVY

Dir Cmd Control Planning & Prgmng Div, OP-940
Department of the Navy
ATTN: OP-943

Naval Construction Battalion Center
ATTN: Code L51, W. Shaw
ATTN: Code L44, H. Haynes
ATTN: Code L08A
ATTN: Code L51, R. Odello
ATTN: Code L51, S. Takahashi

Naval Electronic Systems Command
ATTN: PME 117-211, B. Kruger

Naval Postgraduate School
ATTN: Code 0142 Library

Naval Research Laboratory
ATTN: Code 2627

Naval Surface Weapons Center
ATTN: Tech Library & Info Services Branch

Naval War College
ATTN: Code E-11

Strategic Systems Project Office
Department of the Navy
ATTN: NSP-43

DEPARTMENT OF THE AIR FORCE

Air Force Institute of Technology
ATTN: Library

Air Force Weapons Laboratory
Air Force Systems Command
ATTN: NT, D. Payton
ATTN: NTE, M. Plamondon
ATTN: SUL

Assistant Chief of Staff
Studies & Analyses
Department of the Air Force
ATTN: AF/SASM

Ballistic Missile Office
Air Force Systems Command
ATTN: MNN
ATTN: MNNH

Operations Plans and Readiness
Department of the Air Force
ATTN: AFXODC

Research, Development & Acq
Department of the Air Force
ATTN: AFRDQSM

Foreign Technology Division
Air Force Systems Command
ATTN: NIIS Library

Strategic Air Command
Department of the Air Force
ATTN: XPFS
ATTN: NRI-STINFO Library

OTHER GOVERNMENT AGENCIES

Department of the Interior
Bureau of Mines
ATTN: Technical Library

Department of the Interior
U.S. Geological Survey
ATTN: D. Snyder
ATTN: W. Twenhofel
ATTN: R. Carroll

Department of the Interior
U.S. Geological Survey
ATTN: D. Roddy

DEPARTMENT OF ENERGY CONTRACTORS

Lawrence Livermore National Laboratory
ATTN: H. Heard
ATTN: L-96, L. Woodruff
ATTN: Technical Information Dept Library
ATTN: L-21, D. Oakley

Los Alamos National Scientific Laboratory
ATTN: L. Germaine
ATTN: MS 364, Class. Reports Library
ATTN: B. Killian
ATTN: J. Johnson

DEPARTMENT OF ENERGY CONTRACTORS (Continued)

Sandia National Laboratories
Livermore Laboratory
ATTN: Library & Security Classification Div.

Sandia National Laboratories
ATTN: Mail Services Section for L. Hill
ATTN: Mail Services Section for 3141

Oak Ridge National Laboratory
ATTN: Central Research Library

DEPARTMENT OF DEFENSE CONTRACTORS

Aerospace Corp.
ATTN: Technical Information Services
ATTN: P. Mathur

Agbabian Associates
ATTN: C. Bagge
ATTN: M. Balachanda
2 cy ATTN: M. Agbabian

Applied Theory, Inc.
2 cy ATTN: J. Trulio

AVCO Research & Systems Group
ATTN: Library A830

BDM Corp.
ATTN: Corporate Library
ATTN: T. Neighbors

Boeing Co.
ATTN: T. Berg
ATTN: M/S 42/37, K. Friddell
ATTN: J. Wooster
ATTN: R. Dyrdahl
ATTN: H. Leistner
ATTN: Aerospace Library

California Institute of Technology
ATTN: D. Anderson

California Research & Technology, Inc.
ATTN: Library
ATTN: S. Schuster
ATTN: K. Kreyenhagen

California Research & Technology, Inc.
ATTN: D. Orphal

University of California
ATTN: N. Cook
ATTN: R. Goodman

Calspan Corp.
ATTN: Library

Civil Systems Inc,
ATTN: J. Bratton

University of Denver
ATTN: Sec. Officer for J. Wisotski

EG&G Washington Analytical Services Center, Inc.
ATTN: Library

DEPARTMENT OF DEFENSE CONTRACTORS (Continued)

Electromechanical Sys of New Mexico, Inc.
ATTN: R. Shunk

Eric H. Wang
Civil Engineering Rsch Fac
University of New Mexico
ATTN: N. Baum

Foster-Miller Associates, Inc.
ATTN: J. Hampson for E. Foster

Franklin Institute
ATTN: Z. Zudans

General Electric Company-TEMPO
ATTN: DASIAC

IIT Research Institute
ATTN: R. Welch
ATTN: M. Johnson
ATTN: Documents Library

Institute for Defense Analyses
ATTN: Classified Library

J. H. Wiggins Co., Inc.
ATTN: J. Collins

Kaman AviDyne
ATTN: Library

Kaman Sciences Corp.
ATTN: Library

Lockheed Missiles & Space Co., Inc.
ATTN: Technical Information Center
ATTN: T. Geers

Massachusetts Institute of Technology
ATTN: W. Brace

Merritt CASES, Inc.
ATTN: J. Merritt

Nathan M. Newmark Consult Eng Svcs
ATTN: A. Hendron
ATTN: W. Hall
ATTN: N. Newmark

City College of New York
ATTN: C. Miller

Northwestern University
ATTN: T. Belytschko

Pacifica Technology
ATTN: G. Kent

Physics International Co.
ATTN: Technical Library
ATTN: F. Sauer
ATTN: E. Moore

R & D Associates
ATTN: J. Lewis
ATTN: C. MacDonald
ATTN: R. Port
ATTN: Technical Information Center
ATTN: D. Shrinivasa
ATTN: D. Rawson
ATTN: P. Haas

DEPARTMENT OF DEFENSE CONTRACTORS (Continued)

Rand Corp.
ATTN: A. Laupa

Science Applications, Inc.
ATTN: Technical Library

Science Applications, Inc.
ATTN: Technical Library

Southwest Research Institute
ATTN: A. Wenzel
ATTN: W. Baker

SRI International
ATTN: B. Holmes
ATTN: G. Abrahamson
ATTN: H. Lindberg

Systems, Science & Software, Inc.
ATTN: C. Archembeam
ATTN: W. Wray
ATTN: T. Bache
ATTN: R. Duff
ATTN: D. Grine
ATTN: Library

Terra Tek, Inc.
ATTN: Library
ATTN: H. Pratt

Tetra Tech, Inc.
ATTN: Library

Texas A & M University System
ATTN: Sec Officer for A. Rychlik
ATTN: J. Handin

TRW Defense & Space Sys Group
ATTN: Technical Information Center
ATTN: N. Lipner
ATTN: P. Huff

TRW Defense & Space Sys Group
ATTN: E. Wong
ATTN: P. Dai

Universal Analytics, Inc
ATTN: E. Field

Weidlinger Assoc., Consulting Engineers
ATTN: M. Baron
ATTN: I. Sandler

Weidlinger Assoc., Consulting Engineers
ATTN: J. Isenberg

Westinghouse Electric Corp.
ATTN: W. Volz

William Perret
ATTN: W. Perret